

STRUCTURE OF THE NORTHEAST PACIFIC WAVE CYCLONE OF 19  
NOVEMBER 1980

By

Christopher H. Gratham

B. Sc., The University of British Columbia, 1989

A THESIS SUBMITTED IN PARTIAL FULFILLMENT OF  
THE REQUIREMENTS FOR THE DEGREE OF  
MASTER OF SCIENCE

in

THE FACULTY OF GRADUATE STUDIES  
ATMOSPHERIC SCIENCE

We accept this thesis as conforming  
to the required standard

THE UNIVERSITY OF BRITISH COLUMBIA

August 1991

© Christopher H. Gratham, 1991

In presenting this thesis in partial fulfilment of the requirements for an advanced degree at the University of British Columbia, I agree that the Library shall make it freely available for reference and study. I further agree that permission for extensive copying of this thesis for scholarly purposes may be granted by the head of my department or by his or her representatives. It is understood that copying or publication of this thesis for financial gain shall not be allowed without my written permission.

Department of Atmospheric Science

The University of British Columbia  
Vancouver, Canada

Date Sept 27 1991

## Abstract

The frontal system that passed over the Storm Transfer and Response Experiment Study area on 19 November 1980 was the third vigorous system in succession to affect this region of the northeast Pacific Ocean. This study marks the first detailed investigation of a frontal wave over the Gulf of Alaska and as such provides structural details not shown in other studies.

Precipitation and changes in temperature, wind velocity, and pressure were associated with the passage of both the warm and cold fronts. The thermal structure exhibits a well defined warm sector with regions of large baroclinicity in both the warm and cold frontal zones. Data from radiosonde releases from the northern-most of two observing platforms indicate a mid-level upper moisture front above the kata cold front. Throughout these northern cross-sections, gradients in the warm and cold frontal zones are of similar magnitudes while sections from the southern ship show a warm frontal zone that is more intense than the cold transition region. Along-frontal gradients of equivalent potential temperature are of the same order of magnitude as the cross-frontal gradients.

Horizontal wind components relative to the storm indicate strong inflow to the system at lower layers from both south and east. The wind exits the system to the west and south. Upper level winds are westerly throughout. Gradients of wind components are strongest in frontal zones, which results in the cold front coincident with the peak axis in the vertical component of relative vorticity. The field of horizontal divergence also exhibits its largest magnitudes in the frontal zones, with convergence in the warm frontal zone and divergence in the cold transition region. This seldom observed feature of divergence at the cold front leads to a downwelling motion in this region and categorizes the front

as a kata-cold front. Most of the upward vertical velocity occurs in and around the warm frontal zone as a result of horizontal convergence in this region. Relative isentropic analysis indicates that there are three main air streams within the system. The warm conveyor belt flows to the north in the warm sector and rises gradually as it makes its way to the north. Ahead of the warm front and behind the cold front are two cold air streams that flow to the north and south respectively.

Analysis of the kinematic frontogenesis indicates that confluence and infrequently studied shear effects are the most important processes influencing the frontal gradients. Analysis of uncertainty in the terms of the prognostic kinematic frontogenesis equations reveals that the diabatic heat and twisting terms that others have found important are smaller than their estimated errors in this study.

## Table of Contents

<b>Abstract</b>	<b>ii</b>
<b>List of Tables</b>	<b>vi</b>
<b>List of Figures</b>	<b>vii</b>
<b>Acknowledgement</b>	<b>xiv</b>
<b>1 Introduction</b>	<b>1</b>
1.1 Introduction . . . . .	1
1.2 Synoptic and Thermodynamic Structure . . . . .	2
1.3 Kinematic Structure . . . . .	10
1.4 Frontogenesis and Frontolysis . . . . .	11
1.5 Storm Transfer and Response Experiment (STREX) . . . . .	15
1.6 Goals of the Research . . . . .	16
1.7 Overview of Thesis . . . . .	16
<b>2 Synoptic Analysis</b>	<b>18</b>
2.1 Introduction . . . . .	18
2.2 Surface and Upper Air Analyses . . . . .	18
2.3 Satellite and Radar Imagery . . . . .	23
2.4 Surface Observations . . . . .	27
2.5 System Motion . . . . .	31
2.6 Composite Plan View . . . . .	33

<b>3</b>	<b>Thermal and Moisture Structure</b>	<b>35</b>
3.1	Introduction . . . . .	35
3.2	Temperature and Relative Humidity . . . . .	37
3.3	Potential Temperatures . . . . .	42
<b>4</b>	<b>Kinematic Structure</b>	<b>57</b>
4.1	Horizontal Winds . . . . .	57
4.2	Vertical Velocity . . . . .	73
4.3	Air Streams . . . . .	75
4.3.1	Warm Conveyor Belt . . . . .	75
4.3.2	Cold Airstreams . . . . .	76
<b>5</b>	<b>Diagnosis of Frontogenesis</b>	<b>80</b>
5.1	Introduction . . . . .	80
5.2	Horizontal Potential Temperature Gradient . . . . .	81
5.3	Static Stability . . . . .	89
5.4	Summary . . . . .	96
<b>6</b>	<b>Summary and Conclusions</b>	<b>98</b>
	<b>Bibliography</b>	<b>103</b>

## List of Tables

5.1	Typical maximum values of frontogenetic terms for a number of studies; $H_t$ refers to height of maximum magnitude, $W$ refers to the warm frontal zone; $C$ refers to the cold frontal zone; * these two terms were summed in their figures; MS stands for McBean and Stewart (personal communication); OP for Ogura and Portis (1982); BF for Bond and Fleagle (1985); Sanders for Sanders (1955); Baldwin for Baldwin et al. (1984); Rao for Rao (1966); and PBL for Planetary Boundary layer. . . . .	85
-----	---	----

## List of Figures

- 1.1 Idealized mid-latitude cyclone based on the Norwegian model (from Bjerknes and Solberg, 1922). Top and bottom diagrams show clouds and air motions through cross-sections north of cyclones centre and through the warm sector south of its centre. Middle diagram shows plan view; dash-dotted arrow shows direction of cyclone motion ; other arrows are streamlines of flow at the earth's surface. Hatched areas show regions of precipitation. . . . . 3
- 1.2 Cross-section based on soundings from Uccle, Belgium, from Feb. 1-4, 1933 (from Van Mieghem, 1939). Thin lines are isotherms ( $^{\circ} K$ ), heavy lines show the tropopause and the boundaries of the frontal transition zones. Bottom shows traces of pressure, temperature, surface winds, and rainfall. . . . . 4
- 1.3 Conveyor belt model that shows the three main air streams, cloud, and precipitating regions in a mid-latitude cyclone (from Carlson, 1980). Arrows show flow relative to the system, with two shaded ones indicating flow at the top of the WCB and CCB, the height of which is labeled in mb. The scalloped line shows the edge of the comma shaped cloud pattern, and the shading represents areas where precipitation occurs. . . . . 6
- 1.4 Schematic showing generation of potential instability in the middle troposphere where dry cold air overruns the WCB (from Harrold, 1973). . . . . 7
- 1.5 Schematic diagram showing structure of mesoscale precipitation areas (from Browning and Mason, 1981). . . . . 8

1.6	Schematic diagram showing mesoscale rainbands in relation to a mid-latitude cyclone (from Browning and Mason, 1981). . . . .	9
1.7	Split front model; SCF=surface cold front, UCF=upper cold front (from Browning and Monk, 1982). . . . .	9
1.8	Temporal development of Norwegian school Mid-latitude cyclone; time increasing to the right (from Godske et al.,1957). Upper panel shows vertical cross-section through upper transect, middle panel shows plan view, and bottom panel (b - e) shows vertical cross-section through lower transect. Isobars are solid lines in middle panel, hatched lines indicate areas of precipitation. . . . .	11
1.9	Dashed lines show the streamlines inferred from the geostrophic wind for a cyclone over western Europe on Feb. 17, 1935 (from Bjerknes and Palmen, 1937). . . . .	12
1.10	Vertical cross-section showing idealized composite field for local pressure changes (long-dashed lines are isallobars for $\pm 6 mb/12 hr$ ), potential temperature (short-dashed lines), and streamlines (arrows). Dotted curve represents the trough line; dash-dotted curve is the ridge line; solid lines represent air flow ;and the circles represent the tropopause. (from Fleagle, 1948). . . . .	13
2.1	Surface analyses from the STREX Meteorological Atlas (Reed and Mullen, 1981): a) 1200 UTC 18 November 1980 b) 0000 UTC 19 November 1980. . . . .	20
2.1	Surface analyses from the STREX Meteorological Atlas (Reed and Mullen, 1981): c) 1200 UTC 19 November 1980 d) 0000 UTC 20 November 1980. . . . .	21

2.2	500 mb analyses from the National Meteorological Centre data set : a) 1200 UTC November 19 1980 b) 0000 UTC 20 November 1980. Solid lines indicate geopotential height (metres). . . . .	22
2.3	Analyses from the National Meteorological Centre data set for 1200 UTC November 19 1980 : a) 850 mb b) 700 mb. Solid lines indicate geopotential height (metres) and dashed lines indicate temperature ( $^{\circ}C$ ). Location of surface fronts is also shown. . . . .	24
2.4	a) GOES infrared imagery 0945 UTC 19 November 1980. . . . .	25
2.4	b) GOES infrared imagery 0915 UTC 19 November 1980. . . . .	26
2.5	PPI radar imagery from the ship Vancouver: 0602 UTC 19 November 1980.	28
2.6	Motions of recognizable cloud and precipitation features from GOES imagery. Upper ( $\sim 300$ mb) and Lower trailing edge ( $\sim 550$ mb) features. .	29
2.7	Time series of meteorological variables measured at the ship Vancouver. Shaded area of circle represents fraction of sky obscured with cloud. Ac, As, Sc, and St refer to altocumulus, altostratus, stratocumulus, and stratus clouds respectively. R- refers to light rain and the lines underneath show the duration of the rain. Long vertical lines indicate the time of passage of the surface cold front (CF) and warm front (WF) respectively. . . . .	32
2.8	Composite plan view of system as described in text. . . . .	34
3.1	Time-Pressure cross section of Temperature (solid; contour interval $2^{\circ}C$ ) and Relative Humidity (dashed; contour interval 20%) for the ship Vancouver. Heavy lines to the west and east represent the cold and warm frontal transition zones respectively. . . . .	38

3.2	Time-Pressure cross section of Temperature (solid; contour interval $2^{\circ}C$ ) and Relative Humidity (dashed; contour interval 20%) for the ship Oceanographer. Heavy lines to the west and east represent the cold and warm frontal transition zones respectively. . . . .	39
3.3	Temperature soundings for a) pre-warm frontal (Vancouver 0000 UTC), b) warm sector (Oceanographer 1200 UTC), and c) post-cold frontal (Vancouver 1500 UTC). . . . .	43
3.4	Potential temperature soundings for pre-warm frontal (0045 UTC), warm sector (0845 UTC), and post-cold frontal (1745 UTC) for the ship Vancouver. . . . .	44
3.5	Time-Pressure cross section of Potential Temperature at the ship Vancouver (contour interval $2^{\circ}K$ ). . . . .	46
3.6	Time-Pressure cross section of Potential Temperature at the ship Oceanographer (contour interval $2^{\circ}K$ ). . . . .	47
3.7	Time-Pressure cross section of $\frac{\partial\theta}{\partial p}$ at the ship Vancouver. Dashed lines indicate negative values (Units $\frac{^{\circ}K}{10mb}$ ). . . . .	48
3.8	Time-Pressure cross section of Equivalent Potential Temperature at the ship Vancouver (contour interval $2^{\circ}C$ ). . . . .	50
3.9	Time-Pressure cross section of Equivalent Potential Temperature at the ship Oceanographer (contour interval $2^{\circ}C$ ). . . . .	51
3.10	Time-Pressure cross section of $\frac{\partial\theta_e}{\partial p}$ at the ship Vancouver. Dashed lines indicate negative values (Units $\frac{^{\circ}K}{10mb}$ ). . . . .	52
3.11	Time-Pressure cross section of $\frac{\partial\theta_e}{\partial p}$ at the ship Oceanographer. Dashed lines indicate negative values (Units $\frac{^{\circ}K}{10mb}$ ). . . . .	53
3.12	Time-Pressure cross section of $\frac{\partial\theta_e}{\partial x}$ at the ship Vancouver. Dashed lines indicate negative values (Units $10^{-5}^{\circ}K m^{-1}$ ). . . . .	54

3.13	Time-Pressure cross section of $\frac{\partial \theta_z}{\partial x}$ at the ship Oceanographer. Dashed lines indicate negative values (Units $10^{-5} \text{ }^\circ K m^{-1}$ ).	55
3.14	Time-Pressure cross section of $\frac{\partial \theta_z}{\partial y}$ . Dashed lines indicate negative values (Units $10^{-5} \text{ }^\circ K m^{-1}$ ).	56
4.1	Time-Pressure cross section of u wind component at the ship Vancouver as defined in text (contour interval $2 m s^{-1}$ ).	59
4.2	Time-Pressure cross section of v wind component at the ship Vancouver as defined in text (contour interval $2 m s^{-1}$ ).	60
4.3	Time-Pressure cross section of u wind component at the ship Oceanographer as defined in text (contour interval $2 m s^{-1}$ ).	61
4.4	Time-Pressure cross section of v wind component at the ship Oceanographer as defined in text (contour interval $2 m s^{-1}$ ).	62
4.5	Time-Pressure cross section of $\frac{\partial u}{\partial x}$ for the ship Vancouver. Dashed lines indicate negative values (Units $10^{-4} s^{-1}$ ).	64
4.6	Time-Pressure cross section of $\frac{\partial u}{\partial x}$ for the ship Oceanographer. Dashed lines indicate negative values (Units $10^{-4} s^{-1}$ ).	65
4.7	Time-Pressure cross section of $\frac{\partial v}{\partial y}$ . Dashed lines indicate negative values (Units $10^{-4} s^{-1}$ ). Contours greater than $\pm 0.5 \times 10^{-4} s^{-1}$ not included.	66
4.8	Time-Pressure cross section of horizontal divergence, $\frac{\partial u}{\partial x} + \frac{\partial v}{\partial y}$ . Dashed lines indicate negative values (Units $10^{-4} s^{-1}$ ). Contours greater than $\pm 0.6 \times 10^{-4} s^{-1}$ not included.	67
4.9	Time-Pressure cross section of $\frac{\partial v}{\partial x}$ for the ship Vancouver. Dashed lines indicate negative values (Units $10^{-4} s^{-1}$ ).	69
4.10	Time-Pressure cross section of $\frac{\partial v}{\partial x}$ for the ship Oceanographer. Dashed lines indicate negative values (Units $10^{-4} s^{-1}$ ).	70

4.11	Time-Pressure cross section of $\frac{\partial u}{\partial y}$ . Dashed lines indicate negative values (Units $10^{-4} s^{-1}$ ). Contours greater than $\pm 0.5 \times 10^{-4} s^{-1}$ not included. . . . .	71
4.12	Time-Pressure cross section of vertical component of relative vorticity $\frac{\partial v}{\partial x} - \frac{\partial u}{\partial y}$ . Dashed lines indicate negative values (Units $10^{-4} s^{-1}$ ). Contours greater than $\pm 0.5 \times 10^{-4} s^{-1}$ not included. . . . .	72
4.13	Time-Pressure cross section of significant vertical velocity at the ship Vancouver as calculated kinematically. Dashed lines indicate negative values (upward motion) (Units $Pa s^{-1}$ ). Contours end in the figure since the uncertainties increase with height. Contours greater than $\pm 0.06 Pa s^{-1}$ not included. . . . .	74
4.14	Pressure of constant $30^{\circ}C \theta_e$ and $22^{\circ}C \theta_e$ surfaces. Vectors indicate wind components on the surface at each ship. . . . .	77
4.15	Three air-streams along isentropic surfaces as described in text. . . . .	79
5.1	Frontogenetical effect of terms from equation. Frontogenesis due to: a) confluence, b) shear, and c) tilting. Vectors represent winds, dashed lines are contours of $\xi$ . . . . .	82
5.2	Time-Pressure cross section of frontogenetical effect of $(-\frac{\partial u}{\partial x} \frac{\partial \theta_e}{\partial x})$ . Positive values indicate frontogenesis in the $\theta_e$ field (Units $10^{-9} K m^{-1} s^{-1}$ ). Contours greater than $\pm 0.9 \times 10^{-9} K m^{-1} s^{-1}$ not included. . . . .	84
5.3	Time-Pressure cross section of frontogenetical effect of $(-\frac{\partial v}{\partial x} \frac{\partial \theta_e}{\partial y})$ . Positive values indicate frontogenesis in the $\theta_e$ field (Units $10^{-9} K m^{-1} s^{-1}$ ). Contours greater than $\pm 0.9 \times 10^{-9} K m^{-1} s^{-1}$ not included. . . . .	87

5.4	Time-Pressure cross section of total frontogenetic effect of confluence and twisting terms $\simeq \left( \frac{d}{dt} \frac{\partial \theta_e}{\partial x} \right)$ . Positive values indicate frontogenesis in the $\theta_e$ field (Units $10^{-9} \text{ }^\circ K \text{ m}^{-1} \text{ s}^{-1}$ ). Contours greater than $\pm 0.8 \times 10^{-9} \text{ }^\circ K \text{ m}^{-1} \text{ s}^{-1}$ not included. . . . .	90
5.5	Time-Pressure cross section of frontogenetical effect of $\left( - \frac{\partial u}{\partial p} \frac{\partial \theta_e}{\partial x} \right)$ . Positive values indicate frontogenesis in the $\theta_e$ field (Units $10^{-8} \text{ }^\circ K \text{ s}^{-1} \text{ Pa}^{-1}$ ). Contours greater than $\pm 4.0 \times 10^{-8} \text{ }^\circ K \text{ s}^{-1} \text{ Pa}^{-1}$ not included. . . . .	92
5.6	Time-Pressure cross section of frontogenetical effect of $\left( - \frac{\partial v}{\partial p} \frac{\partial \theta_e}{\partial y} \right)$ . Positive values indicate frontogenesis in the $\theta_e$ field (Units $10^{-8} \text{ }^\circ K \text{ s}^{-1} \text{ Pa}^{-1}$ ). Contours greater than $\pm 2.0 \times 10^{-8} \text{ }^\circ K \text{ s}^{-1} \text{ Pa}^{-1}$ not included. . . . .	93
5.7	Time-Pressure cross section of total frontogenetic effect of the two twisting terms $\simeq \left( \frac{d}{dt} \frac{\partial \theta_e}{\partial p} \right)$ . Positive values indicate frontogenesis in the $\theta_e$ field (Units $10^{-8} \text{ }^\circ K \text{ s}^{-1} \text{ Pa}^{-1}$ ). Contours greater than $\pm 4.0 \times 10^{-8} \text{ }^\circ K \text{ s}^{-1} \text{ Pa}^{-1}$ not included. . . . .	95

## Acknowledgement

Many people have provided me with valuable support throughout this challenging and rewarding part of my life. Mr. Ernie Recker of UW, Dr. Nick Bond of NOAA-PMEL, and Dr. Ron Stewart of the AES all made useful data available to me. I would like to acknowledge the tremendous contribution of my thesis advisor, Dr. Gordon McBean. He was always available to provide advice and direction to my research and his editing has greatly improved this thesis. Drs. Douw Steyn and Phil Austin provided much valuable input and their open door policies regarding my questions is greatly appreciated. I would also like to thank my friends and colleagues in Atmospheric Science and Geography for many fruitful discussions. Finally, I am deeply indebted for the understanding and encouragement shown by my loving wife, Suzanne, who acted as art director, spiritual advisor, and best friend.

## Chapter 1

### Introduction

#### 1.1 Introduction

Atmospheric frontal systems have long been associated with periods of vigorous weather and the forecasting of their motion and evolution remains a central aspect of present day meteorology. For over seventy years these disturbances have been studied with concentration on the synoptic, dynamic, and thermodynamic structure. More recently, considerable emphasis has been focussed towards understanding the complex processes involved in frontogenesis (frontolysis), the intensification (weakening) of frontal characteristics. Due to the great expense and logistical difficulties of planning and executing observational programs designed to study marine cyclones the vast majority of case studies have involved cyclones over the continents and coastal regions. Until recently, studies of cyclones over mid-latitude marine areas have been rare, even though their features are very important to forecasting in coastal regions. Studies of storms in the northeast Pacific Ocean are also essential since this region is characterized by a large number of cyclones (Gyakum et al. 1988) and by frequent cyclogenesis (Murty et al. 1983).

The following three sections provide a brief historical review of the synoptic, thermodynamic, kinematic, and frontogenetic structure of mid-latitude cyclones, based primarily on studies of storms over continents. Following these are sections introducing the field program from which the data for this study were collected, reviewing the goals of this

research, and finally an overview of the body of this thesis.

## 1.2 Synoptic and Thermodynamic Structure

The first synoptic scale model of a mid-latitude cyclone was developed by the Norwegian Bergen school (Bjerknes, 1919; Bjerknes and Solberg, 1922 figure 1.1). Their model indicated the wave shape that is commonly exhibited by the Scandinavian cyclones they were studying. The wave consists of a warm front stretching south east from the low pressure centre and a cold front extending to the south west. Ahead of the warm front and behind the cold front lies cold air and between the fronts is the region of warm air. Their observations suggested that precipitation associated with the warm front is essentially uniform due to widespread gentle uplift of the warm sector over the colder air ahead of it. They envisioned the surface cold front as a well-defined squall line with a band of cumulonimbus convection along and above the surface feature.

Nearly twenty years later, Bergeron (1937) introduced the terms “ana” and “kata” to distinguish between fronts at which there is ascent in the warm air (ana-front) and those in which descent occurs in all but the lowest layers (kata-front). Of these two, the ana-front, accompanied by abrupt temperature changes, sharp wind veering, and a marked precipitation belt, is by far the easiest for the forecaster to analyse (Browning and Monk, 1982). By comparison, they state that kata-fronts are usually accompanied by a change only in relative humidity and little or no change in temperature.

The first attempts to study the upper-air structure of extra-tropical cyclones used balloon sondes and aircraft observations. Figure 1.2 shows an example of a vertical cross-section resulting from one of the earliest ascents. This diagram illustrates the structure of the warm sector followed by a shallow cold air tongue, which corresponds well with the Bergen scheme.

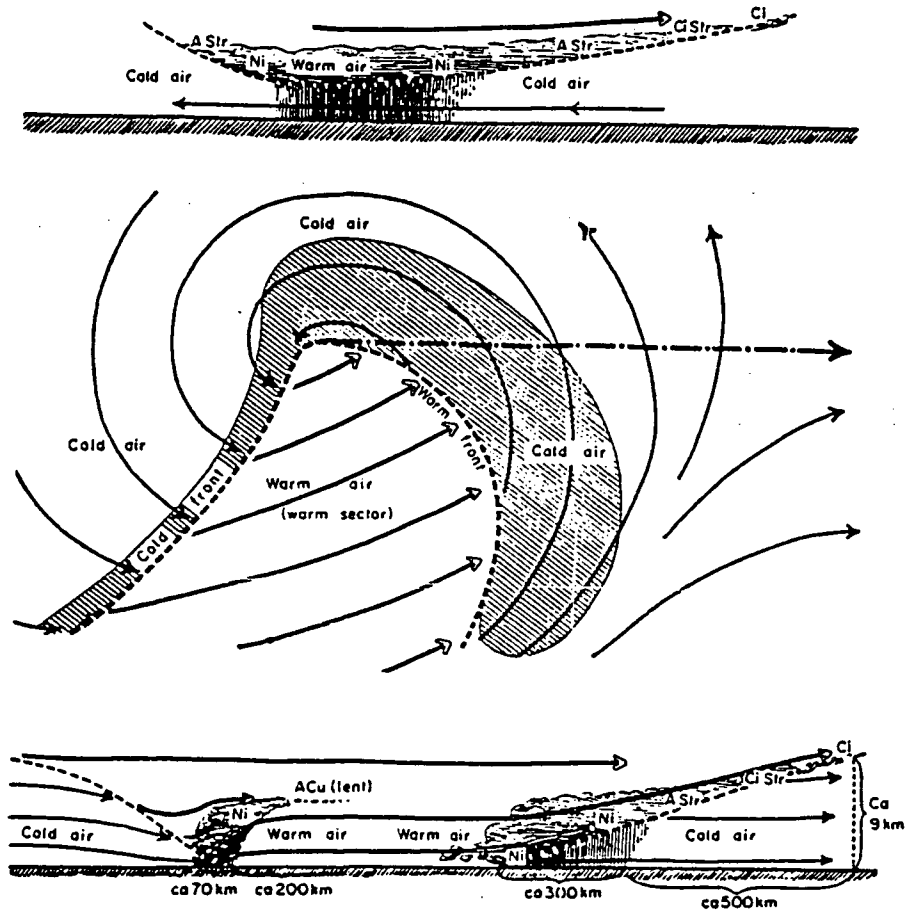


Figure 1.1: Idealized mid-latitude cyclone based on the Norwegian model (from Bjerknes and Solberg, 1922). Top and bottom diagrams show clouds and air motions through cross-sections north of cyclones centre and through the warm sector south of its centre. Middle diagram shows plan view; dash-dotted arrow shows direction of cyclone motion ; other arrows are streamlines of flow at the earth's surface. Hatched areas show regions of precipitation.

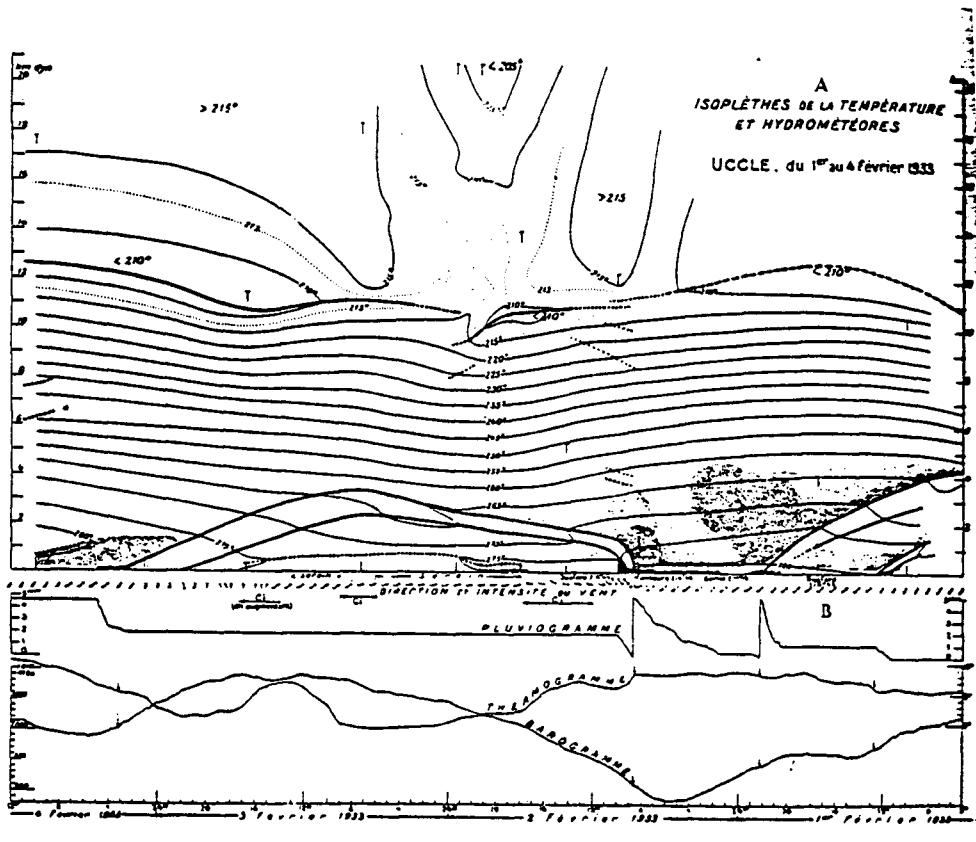


Figure 1.2: Cross-section based on soundings from Uccle, Belgium, from Feb. 1-4, 1933 (from Van Mieghem, 1939). Thin lines are isotherms ( $^{\circ}K$ ), heavy lines show the tropopause and the boundaries of the frontal transition zones. Bottom shows traces of pressure, temperature, surface winds, and rainfall.

The availability of weather radar, satellites, and radiosondes since the early 1960's has led to more detailed examination of the structure of fronts and their associated precipitation features. While these investigations have generally supported the large scale features of the classical frontal model, they have also revealed that the more detailed structure is indeed far more complex than originally presented.

Harrold (1973), Browning (1972), and Carlson (1980) developed a conceptual model that accounts for the principal synoptic scale features of cloud and precipitation, and provides a useful framework for understanding the phenomena on a somewhat smaller scale. This model (figure 1.3) displays how the overall cloud and precipitation distribution can be explained in terms of three main flows. The northern-hemisphere warm conveyor belt (WCB) originates in the boundary layer in a region of high pressure south of the low pressure centre. This warm, moist air flow travels northwards ahead of the cold front and turns anticyclonically as it ascends above the cold air ahead of the surface warm front. The second stream, the cold conveyor belt (CCB), originates in anticyclonic flow just north-east of the cyclone. It makes its way westward ahead of the surface warm front beneath the WCB, then ascends and turns anticyclonically as it emerges from beneath the western edge of the WCB. The third air stream in this model is the dry flow that starts in the upper troposphere to the west of the system and descends while turning cyclonically and flows toward the north just, on the cold side of the cold front.

The authors reasoned that it is these three flows that combine to produce the comma shaped cloud pattern that is characteristic of extra-tropical cyclones. The sharp western edge of the comma cloud results from confluence of the WCB and the descending dry airflow. Precipitation is commonly found parallel to the cold front, in association with the early ascent of the WCB, and extends into the region where the WCB ascends ahead of the surface warm front.

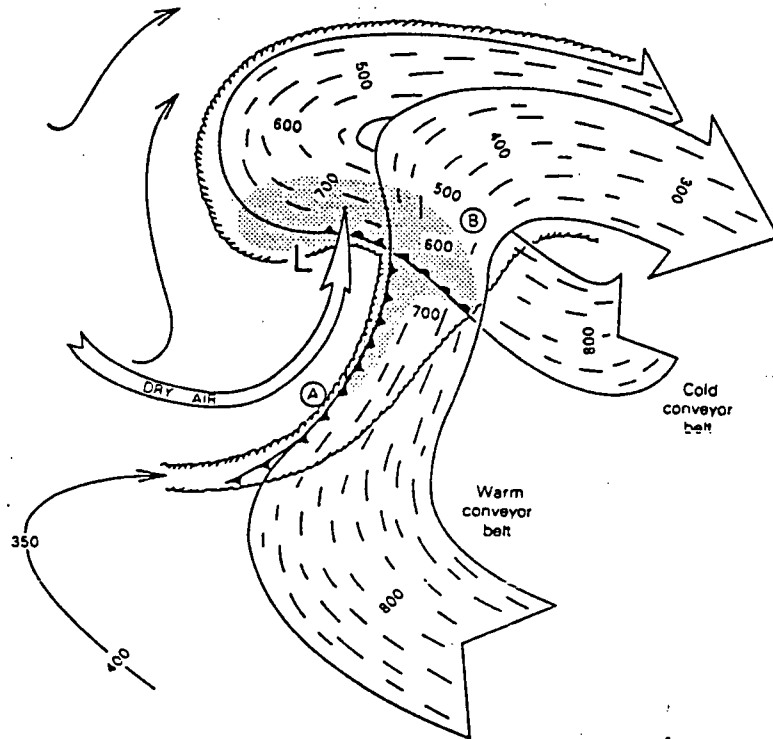


Figure 1.3: Conveyor belt model that shows the three main air streams, cloud, and precipitating regions in a mid-latitude cyclone (from Carlson, 1980). Arrows show flow relative to the system, with two shaded ones indicating flow at the top of the WCB and CCB, the height of which is labeled in mb. The scalloped line shows the edge of the comma shaped cloud pattern, and the shading represents areas where precipitation occurs.

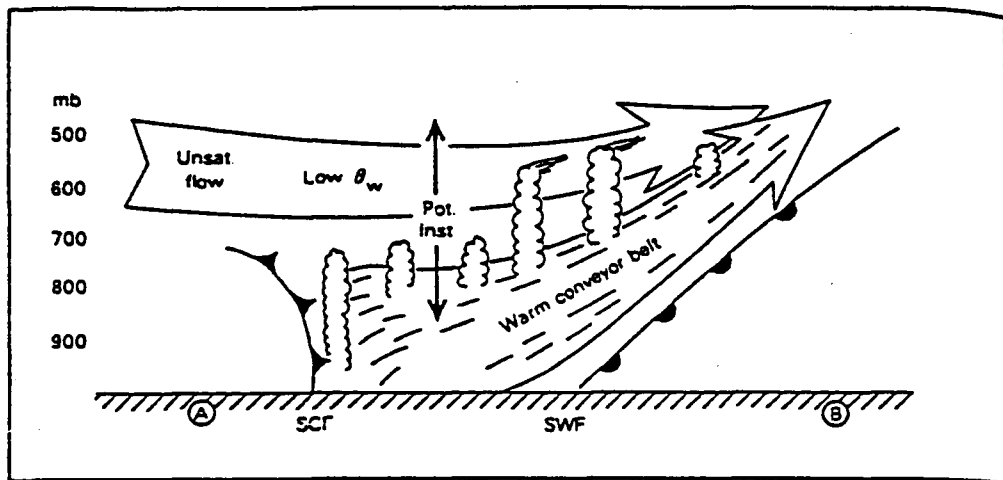


Figure 1.4: Schematic showing generation of potential instability in the middle troposphere where dry cold air overruns the WCB (from Harrold, 1973).

Browning and Mason (1981) assert that the most common form of convection in mid-latitude depressions does not have its roots at the surface but, rather, is restricted to a shallow layer of the middle troposphere, somewhere between 700 and 500 *mb*. Figure 1.4 shows that as flow ascends, potential instability is realized at the top of the warm conveyor belt. The resulting convection takes the form of small cells (horizontal dimensions of about one kilometre) that are called generating cells because of their role in initiating precipitation (Wexler and Atlas, 1959). These cells tend to form in clusters, with dimensions of several tens of kilometres and give rise to the mesoscale precipitation areas (MPAs) illustrated in figure 1.5.

There is a tendency for the precipitation in the MPAs to be in linear patterns that are called mesoscale rainbands. These patterns have been studied quite extensively in both the USA and the UK (Austin, 1960; Elliot and Hovind, 1964; Krietzberg and Brown, 1970; Houze et al., 1976; Browning and Harrold, 1969; Browning et al., 1970) Figure 1.6 shows that the main types of bands that are associated with mid-latitude depressions,

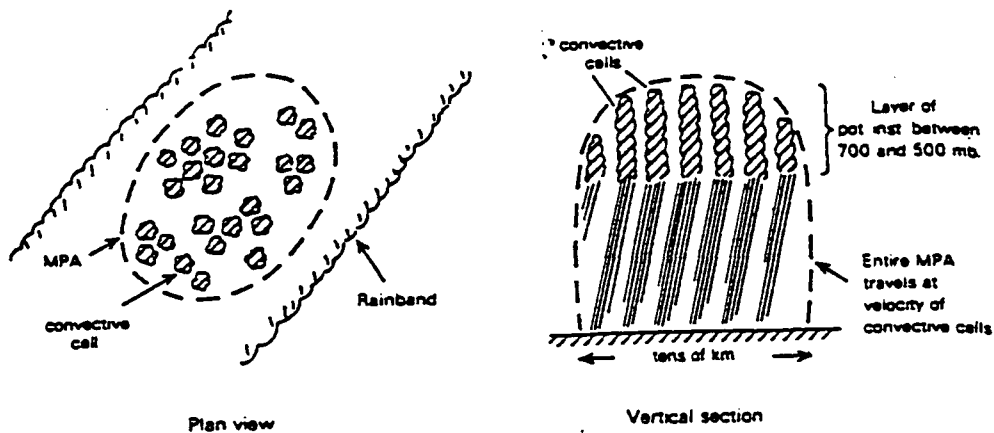


Figure 1.5: Schematic diagram showing structure of mesoscale precipitation areas (from Browning and Mason, 1981).

which with the exception of type 5, are all 50 – 100 km wide. Bands of types 2 and 5 arise from convection initiated at the surface, with type 5 bands often corresponding to line convection commonly found off the Pacific coast of North America (Browning and Mason, 1981).

Not all of these rainband types need occur in every mid-latitude cyclone. Type 4 bands, for example, are most commonly associated with occluding systems while types 3 and 5 are formed at ana-cold fronts (Browning and Mason, 1981; Sansom, 1951). The CYCLES project of the University of Washington (Houze et al., 1976) has studied rainbands off the Washington coast, at scales from the synoptic to the micro, using radar and aircraft data.

Browning and Monk (1982) proposed a conceptual split cold front model (figure 1.7), with an overrunning upper cold front (humidity front) as an alternative to the Norwegian model of a kata-cold front. They note that this model is especially useful for interpreting cloud and precipitation patterns as observed by radar and satellite.

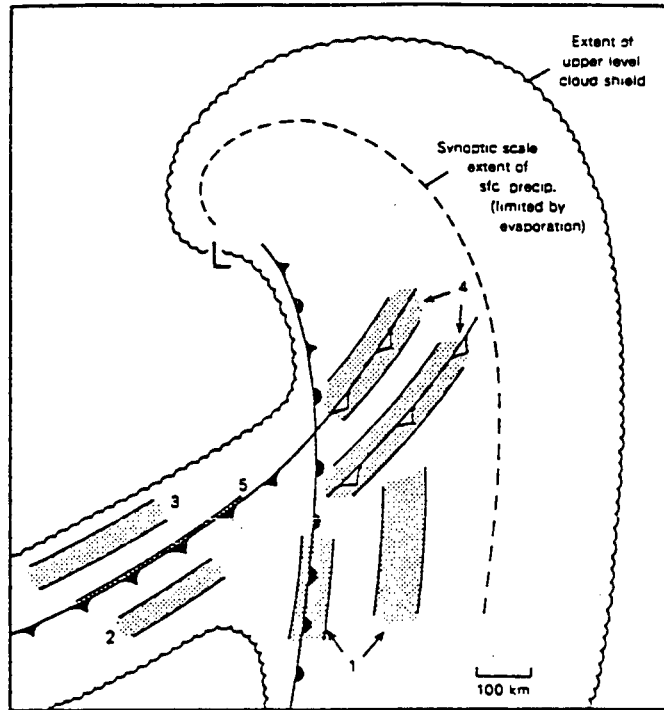


Figure 1.6: Schematic diagram showing mesoscale rainbands in relation to a mid-latitude cyclone (from Browning and Mason, 1981).

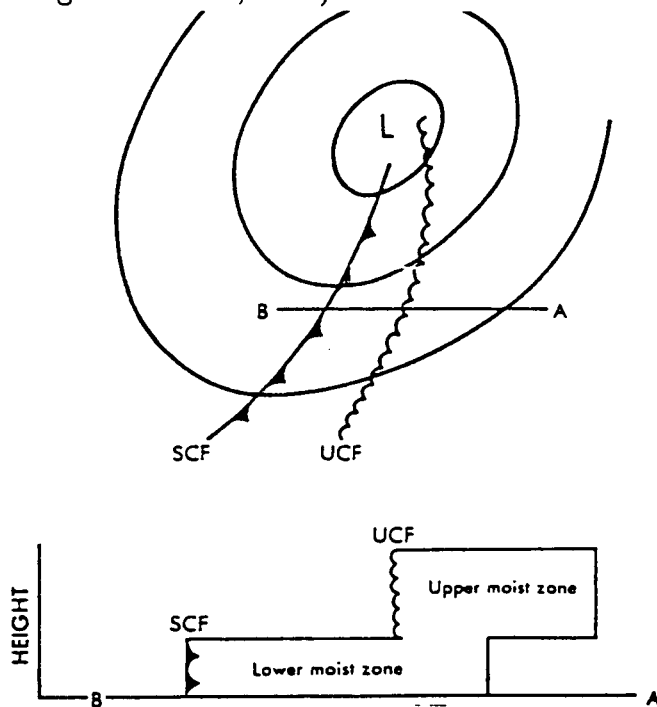


Figure 1.7: Split front model; SCF=surface cold front, UCF=upper cold front (from Browning and Monk, 1982).

### 1.3 Kinematic Structure

The temporal development of the classic Bergen school cyclone is shown in figure 1.8 (Godske et al., 1957). The cyclone is initiated as a small perturbation on a quasi-stationary front, characterized by cyclonic shear. After the small initial wave has started, warm air infiltrates into the cold air, the pressure falls near the wave crest and this perturbation causes a pressure distribution favorable to further development of cyclonic circulation about the crest. It was observed that cold fronts typically advance faster than do warm ones, leading to the warm front eventually being overtaken and the warm air being lifted entirely away from the earth's surface. The resulting "occluded" front (Bjerknes, 1919) is bounded on either side by cold air masses with only slightly different properties. As the development proceeds, the occlusion grows in extent leaving a large cold vortex in the lower troposphere with warm air still existing further up. The process eventually comes to an end when the cyclone loses all frontal structure and gradually dissipates due to frictional effects.

Bjerknes and Solberg (1922) recognised that an essential feature for cyclogenesis, "The tendency towards the formation of a discontinuity or the intensification of an existing one" (Pettersen, 1956), is conversion of potential energy of the warm air into kinetic energy of the cyclone. They reasoned that the kinetic energy of a system could only increase as long as an appreciable air-mass (frontal) contrast was available. At the final stages of occlusion the system fails to develop further due to absence of potential energy in the weakened air-mass contrast near the cyclone centre.

Figure 1.9 illustrates the flow streamlines inferred from the geostrophic wind field by Bjerknes and Palmén (1937). This clearly portrays the cyclonic curvature aloft behind the cold front and indicates the tendency towards anticyclonic curvature over the warm front.

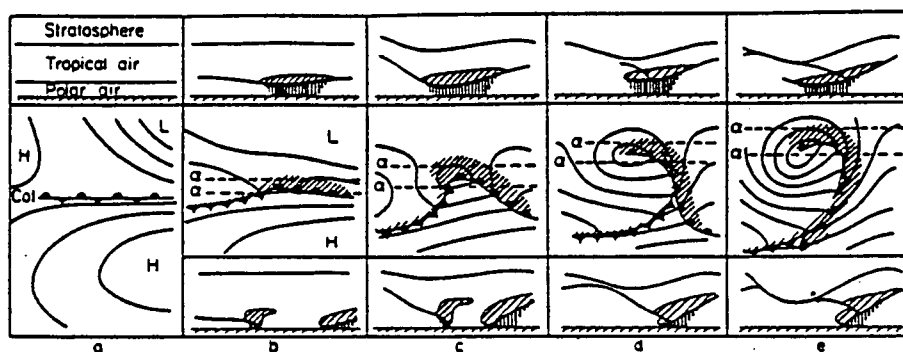


Figure 1.8: Temporal development of Norwegian school Mid-latitude cyclone, time increasing to the right (from Godske et al., 1957). Upper panel shows vertical cross-section through upper transect, middle panel shows plan view, and bottom panel (b – e) shows vertical cross-section through lower transect. Isobars are solid lines in middle panel, hatched lines indicate areas of precipitation.

As aerological soundings improved, further efforts were made to compute three dimensional fields of motion and relate them to the occurrence of clouds and precipitation (Haurwitz et al., 1945; Houghton and Austin, 1946; Panofsky, 1946; Miller, 1948a; Fleagle, 1948). Figure 1.10 shows a generalized picture of motion, potential temperature, and pressure changes in a cross-section through a traveling cyclone based on a number of studies by Fleagle (1948). This diagram indicates that vertical motions are largest in the region just ahead of the trough and that they decrease away from it. Areas of ascent are associated with pressure decrease ahead of the trough, while descent corresponds with pressure increase to the rear.

#### 1.4 Frontogenesis and Frontolysis

A primary motivation for the study of the structure of mid-latitude frontal systems is to gain a better understanding of the complex processes governing frontogenesis and

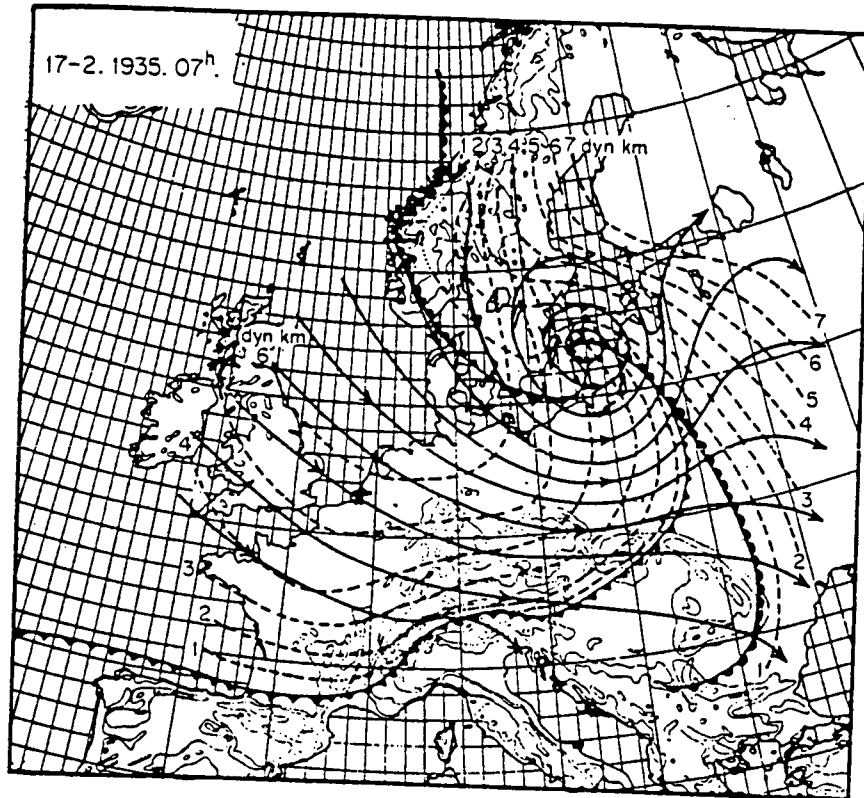


Figure 1.9: Dashed lines show the streamlines inferred from the geostrophic wind for a cyclone over western Europe on Feb. 17, 1935 (from Bjerknes and Palmen, 1937).

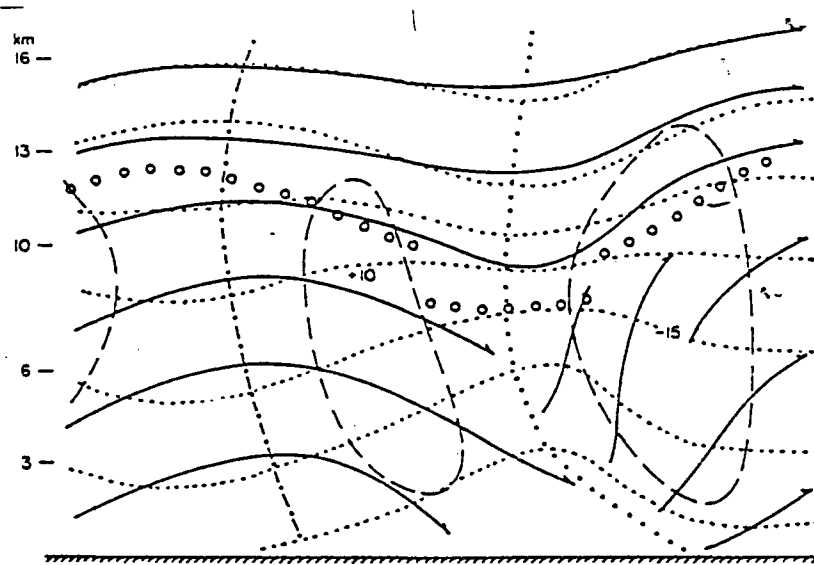


Figure 1.10: Vertical cross-section showing idealized composite field for local pressure changes (long-dashed lines are isallobars for  $\pm 6 \text{ mb}/12 \text{ hr}$ ), potential temperature (short-dashed lines), and streamlines (arrows). Dotted curve represents the trough line; dash-dotted curve is the ridge line; solid lines represent air flow; and the circles represent the tropopause. (from Fleagle, 1948).

frontolysis. Frontogenesis refers to the intensification of frontal characteristics while frontolysis is the opposite effect.

Generally, fronts are subjected to the tendency for weakening of thermal contrasts in the lower layers due to the transfer of properties from the earth's surface that act to reduce the air-mass contrast (Palmen and Newton, 1969). This propensity for heat transfer to reduce the contrast is even more pronounced over marine areas than over land due to the larger heat storage and latent heat flux from water. As a result of the reduction of air-mass contrasts, the persistence of a frontal system is dependent on it being continuously acted upon by kinematic frontogenesis. These frontogenetic processes involve a number of mechanisms, the importance of each of which varies with height, distance from the front, and from one storm to another. Sawyer (1956), Eliassen (1959, 1962), and Hoskins and Bretherton (1972) have all conducted theoretical studies of frontogenesis and the so-called Sawyer-Eliassen secondary circulation has been used to relate the kinematics to the dynamics of frontal systems. This theory relates secondary circulation in a plane normal to the front to frontogenesis due to geostrophic deformation. As frontogenetic processes increase the temperature gradient across the front, vertical shear in the along-front direction increases to maintain the thermal wind balance. Ageostrophic (secondary) circulations in the cross-frontal plane then accompany accelerations in the along-front wind.

Prognostic equations for parameters that characterize frontal development have been developed, using actual instead of geostrophic winds, and used by a number of researchers (Miller, 1948b; Reed and Sanders, 1953; Newton, 1954; Sanders, 1955; Rao, 1966; Keyser and Anthes, 1982; Ogura and Portis, 1982; Baldwin et al., 1984; Bond and Fleagle, 1985; McBean and Stewart, personal communications). These equations will be discussed in further detail in chapter 5.

## 1.5 Storm Transfer and Response Experiment (STREX)

The field stage of STREX was conducted in the Gulf of Alaska during November and December of 1980 (Fleagle et al., 1982). The objectives of this research programme were to study: the spatial distribution of the surface fluxes; the scales of coupling between the boundary layer and the troposphere; the scales of latent heat release; and the effects of storms on the upper oceans. During the six weeks of the programme, a total of 18 low pressure centres moved through the research area and ten of these were chosen for intensive observation.

The primary observing platforms during STREX were two ships (the weatherships CSS Vancouver located at 50°N, 145°W called station P and USS Oceanographer at 50°N, 140°W) which made both surface observations and released upper-air balloons. Throughout the programme these radiosondes were launched at six-hour intervals, and through the intensive periods they were released every three hours. In order to give more detailed information on boundary layer stability and structure, pressure-temperature-humidity sondes were also launched at one hour intervals during some of the intensive observation periods. Conventional radar images were produced from the digital radar data acquired from the ship Vancouver. Research aircraft were dispatched during certain storms; however, they were unable to collect data for the system currently under consideration since it passed through the area at night. Visible and infrared images from both geostationary and polar orbiting satellite are also available throughout the study programme.

Two of the storms that passed through the STREX study area have previously been studied in detail. The storm of 15 November (four days prior to the system currently being studied) has been investigated in Bond and Fleagle (1985) and Bond (1986). This study investigated an intense cold front that passed rapidly through the area. They

found that this system was quite similar to other observed fronts and modelled frontal simulations. Their mesoscale aircraft analyses indicated that a narrow zone  $\sim 2\text{ km}$  wide at the leading edge of the front was the primary region of vertical transport of air and moisture. Gradients of temperature, humidity, and wind and the strongest frontogenetic processes were also predominant near the leading edge of the front. McBean and Stewart (1991) investigated the occluded frontal system that passed through the same area on 17 November. They found a detached upper frontal zone, similar to the upper cold front of Browning and Monk (1981). They also found strong areas of uplift just ahead of the surface cold front but subsiding motions in higher regions of the cold front. The storm of 19 November presents an excellent opportunity to compare the detailed structure of three consecutive systems and to attempt to identify areas of similarities and differences between the cases.

## 1.6 Goals of the Research

The objective of this research is to investigate the synoptic, thermodynamic, and kinematic structure of the frontal system that passed through the STREX study area on 19 November, 1980. These analyses will be used to diagnose the dominant processes determining the frontogenesis or frontolysis of the system. Results will be compared with those of other observational and numerical studies in addition to conceptual models of such mid-latitude cyclones.

## 1.7 Overview of Thesis

Chapter 2 will show a synoptic analysis of the frontal system, using satellite and radar images as well as surface ship observations. Chapters 3 and 4 provide detailed analyses of the thermodynamic and kinematic structure respectively. Chapter 5 consists

of a diagnosis of the frontogenetic processes involved in the prognostic equations for the baroclinicity and the static stability. The final chapter presents a summary and conclusions.

## Chapter 2

### Synoptic Analysis

#### 2.1 Introduction

The system of 19 November involved linked low centres in the surface pressure and 500 mb geopotential height fields that were quasi-stationary ( $55^{\circ}$  N,  $160^{\circ}$  W) and nearly constant in magnitude (975 mb, 510 dm) throughout the 24 hours of interest (figures 2.1 and 2.2 from the STREX Meteorological Atlas, Reed and Mullen, 1981 and from the National Meteorological Centre data set). The associated frontal wave was moving rapidly to the northeast with the strong upper level flow and had a large cloud mass and precipitating regions embedded within it.

#### 2.2 Surface and Upper Air Analyses

The 500 mb analyses (figure 2.2) shows a low centre in the height field, a broad upper level trough that extended to the south-southeast between  $160^{\circ}$  and  $150^{\circ}$  W, and ridging along the West coast of North America. Consequently, the study area was under the influence of a strong southwesterly upper level flow, which persisted from 11 November through 27 November. Throughout the 24 hours of interest the pattern was very similar but the trough tilted slightly from a nearly north-south orientation at 0000 UTC 19 November to more north-northwest/south-southeast by 0000 UTC 20 November.

The surface analysis in figure 2.1 indicates the main low pressure centre at  $49^{\circ}$  N and  $165^{\circ}$  W and two frontal systems very close together at 1200 UTC on 18 November. An

occluded front lay in a north south line from the low to  $45^{\circ}$  N with a cold front extending to the southeast and a warm front to the southwest. A secondary low was situated at  $43^{\circ}$  N and  $158^{\circ}$  W with an associated frontal wave to the south of it.

By 0000 UTC on 19 November the northern-most of the two lows had shifted to its quasi-stationary position and the secondary low was no longer analysed. The occluded front extended to the southeast from the low to  $47^{\circ}$  N and  $151^{\circ}$  W from where the cold front continued to the southwest. The frontal wave that had been associated with the secondary low was by this time only  $\sim 100$  km to the southeast of the junction of the occluded and cold frontal sections of the first front. Given the paucity of data and the lack of strong evidence from the satellite images it is quite possible that there were not two distinct cold fronts at all but rather a wide cold frontal transition zone. Regardless of whether there were two fronts or only one at the time of this analysis, the trailing cold front from the previous analysis was moving in the same direction as, and more rapidly than, the leading one. As a result they amalgamated at roughly 0000 UTC on 19 November. By the 1200 UTC surface analysis a typical pattern of an occluded front with a frontal wave at its southern end was clearly evident. The system continued towards the northeast for the next 24 hours until it was over the continent.

An estimate of the motion of the system can be made by tracking successive positions of the frontal wave on the surface analyses. Over the 36 hours shown here the velocity of the frontal wave was  $17 \text{ m.s}^{-1}$  from  $240^{\circ}$ . Based on this direction of motion, the front passed over the Oceanographer at a point  $180$  km further south along its axis than where it crossed the Vancouver. Using the frontal position on the surface charts and this speed to interpolate between charts we conclude that the surface warm front passed the Vancouver close to 0630 UTC and the cold front at approximately 0930 UTC.

The surface air temperature differences across both the warm and cold fronts were from  $2$  to  $4^{\circ}\text{C}$ , as was the dew-point temperature difference across the warm front (Pacific

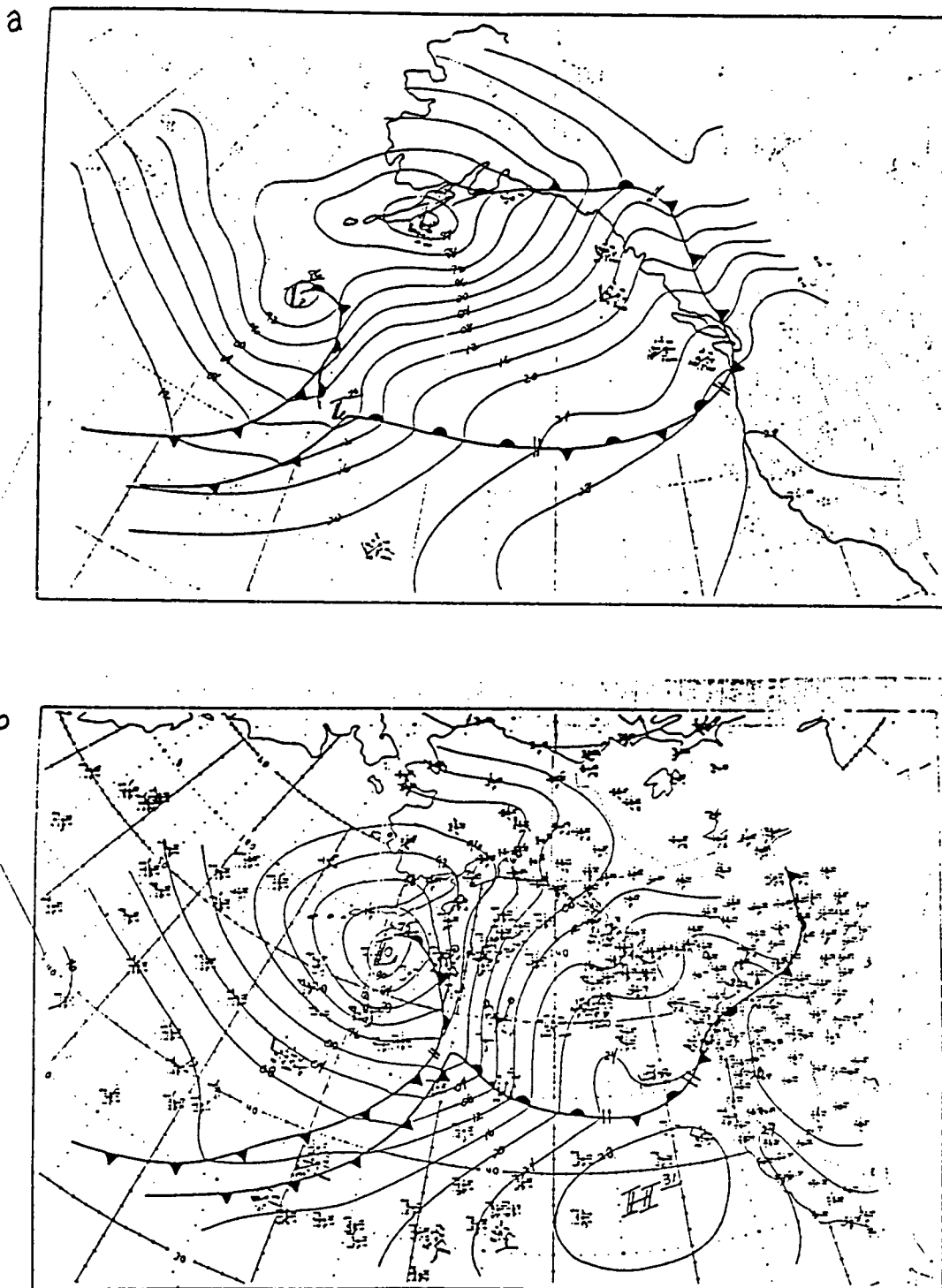


Figure 2.1: Surface analyses from the STREX Meteorological Atlas (Reed and Mullen, 1981): a) 1200 UTC 18 November 1980 b) 0000 UTC 19 November 1980.

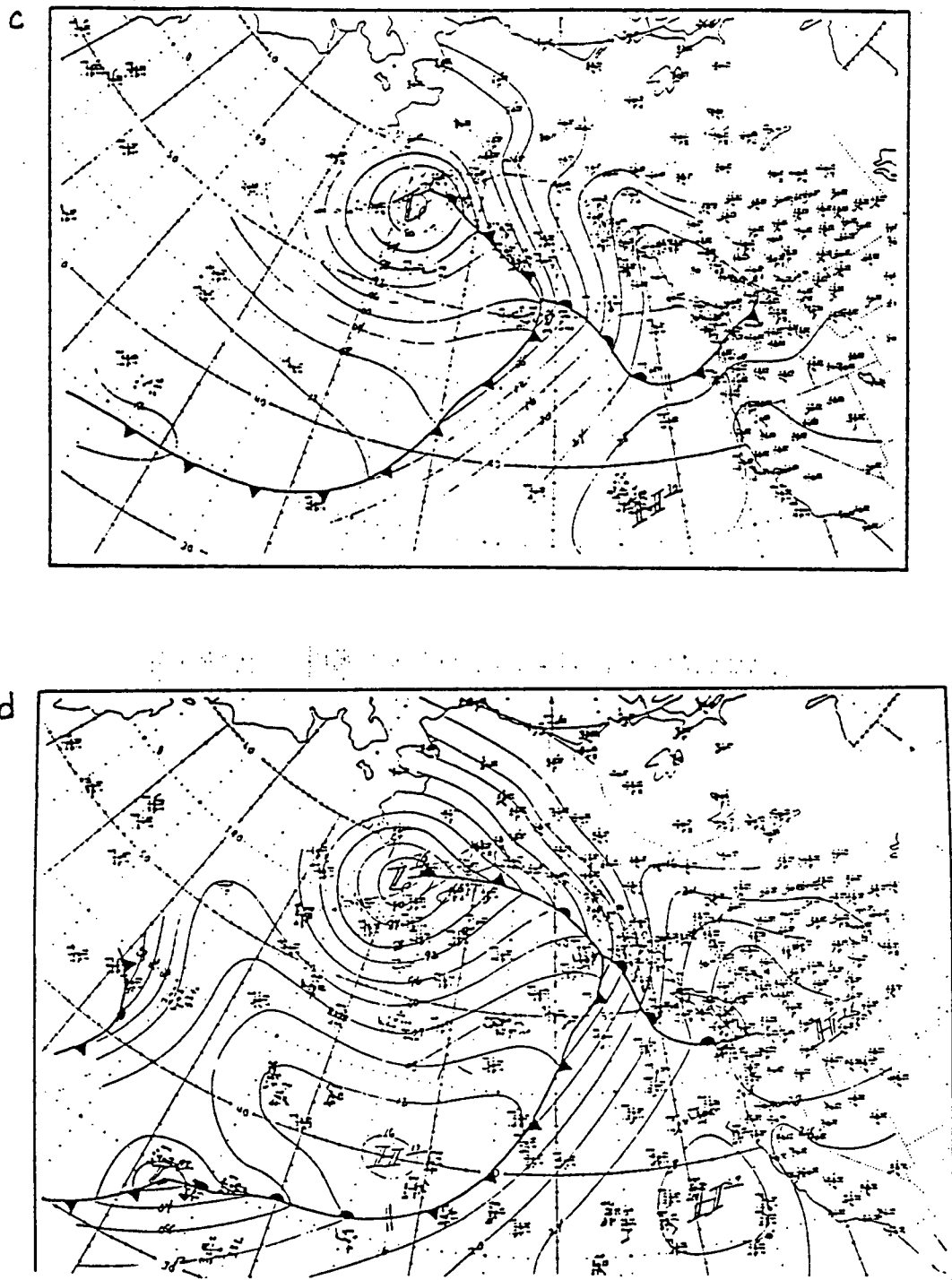


Figure 2.1: Surface analyses from the STREX Meteorological Atlas (Reed and Mullen, 1981): c) 1200 UTC 19 November 1980 d) 0000 UTC 20 November 1980.

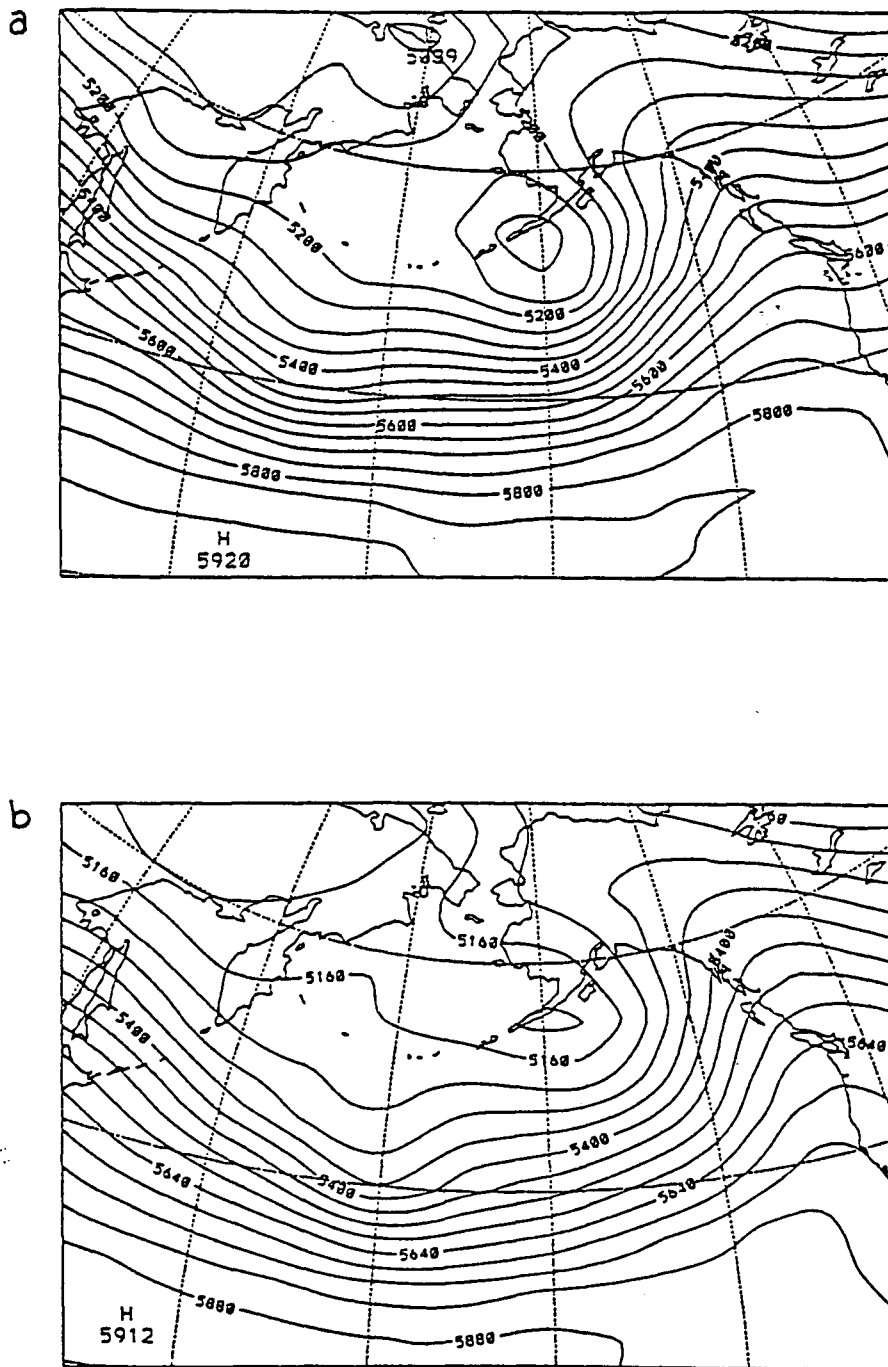


Figure 2.2: 500 mb analyses from the National Meteorological Centre data set : a) 1200 UTC November 19 1980 b) 0000 UTC 20 November 1980. Solid lines indicate geopotential height (metres).

Weather Centre surface analyses). However, the dew-point temperatures within the warm sector were 6 to 10 °C warmer than those behind the cold front. Winds behind the cold front were westerly with southwesterlies in the warm sector and south-southeasterlies ahead of the warm front. The wind speeds in the warm sector were generally lower than those in regions of colder air.

The 850 *mb* and 700 *mb* height analyses (figure 2.3) show a similar pattern to that at 500 *mb* with a low in the field near 160° W, 55° N and the study region experiencing a generally southwesterly flow. In the temperature field at both levels the warm sector is illustrated by ridging of the isotherms. The strongest cross-frontal horizontal temperature gradients occur in the region just behind the surface cold front with maximum 700 *mb* gradients ( $\sim 2 \times 10^{-5} \text{ }^\circ\text{C m}^{-1}$ ) larger than those at 850 *mb* ( $\sim 1.5 \times 10^{-5} \text{ }^\circ\text{C m}^{-1}$ ). Further to the west of this region the temperature gradients are smaller. The area just to the east of the surface warm frontal zone also shows enhanced cross-frontal temperature gradients, although much smaller than on the cold frontal side.

### 2.3 Satellite and Radar Imagery

Figure 2.4a shows the large cloud mass associated with the system. The comma cloud pattern regularly accompanying mid-latitude cyclones is clearly evident with a well defined trailing edge that corresponds with the surface cold front. The enhancement in figure 2.4b emphasizes the tops of the high ( $\sim 300$  *mb*) clouds which are closely associated with the precipitating regions.

Figure 2.5 shows a PPI radar image of the precipitation band associated with the warm front that passed through the ship Vancouver. The main areas of reflectivities  $\leq 24$  *DBZ* correspond to the light rain observed at the ship and the smaller regions of

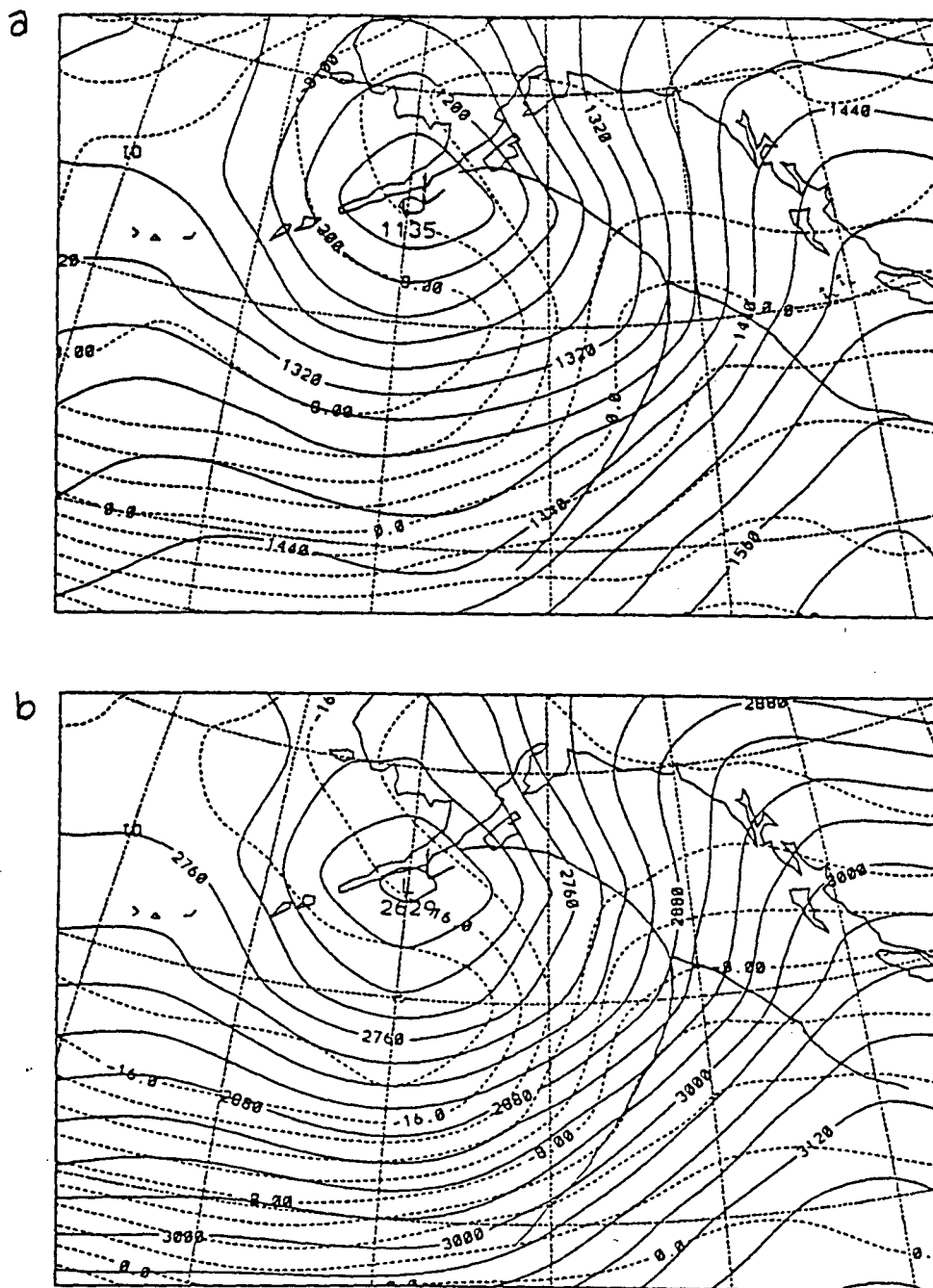


Figure 2.3: Analyses from the National Meteorological Centre data set for 1200 UTC November 19 1980 : a) 850 mb b) 700 mb. Solid lines indicate geopotential height (metres) and dashed lines indicate temperature ( $^{\circ}\text{C}$ ). Location of surface fronts is also shown.

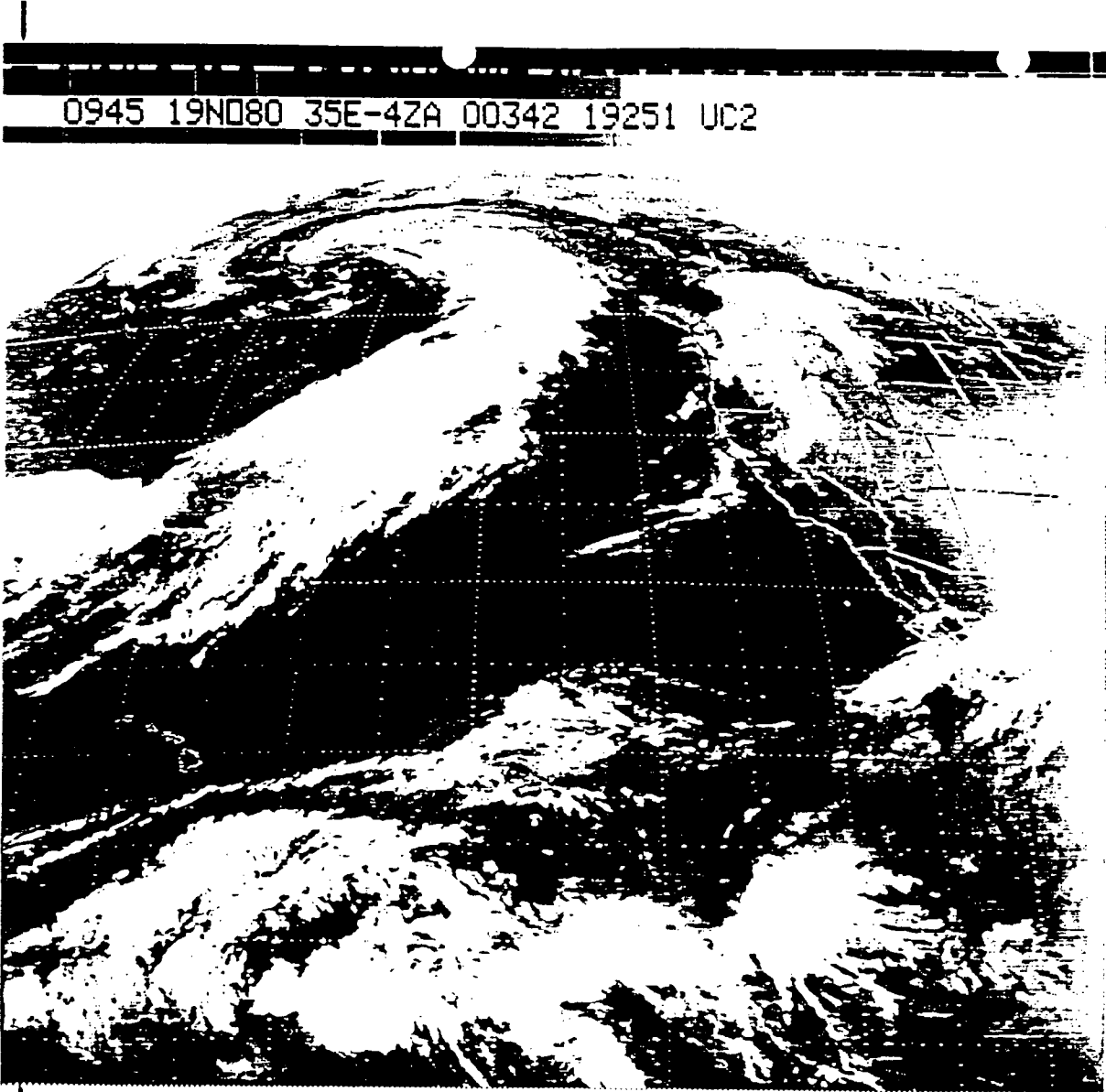


Figure 2.4: a) GOES infrared imagery 0945 UTC 19 November 1980.

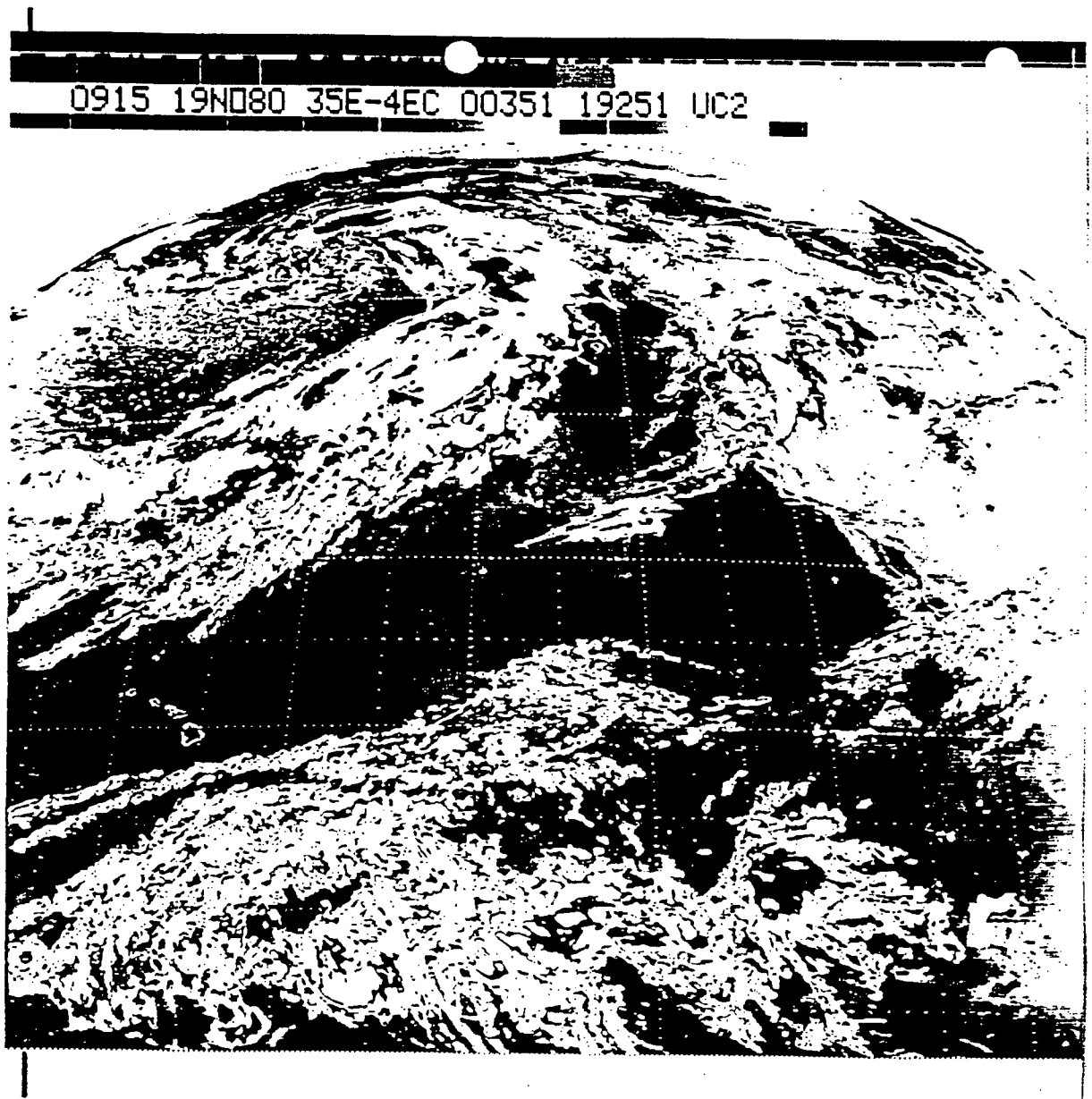


Figure 2.4: b) GOES infrared imagery 0915 UTC 19 November 1980.

more intense echos  $\geq 27$  DBZ (to the west of the ship in this figure) either did not occur or were not recorded at the Vancouver.

By tracking the movement of recognizable features from the GOES imagery and radar plots we can determine the speed and direction of movement of these features. Figure 2.6 shows the tracking of a number of cloud features. Upper features are areas of cloud top brightness temperatures from  $-51.2^{\circ}\text{C}$  to  $-60.2^{\circ}\text{C}$ , which from the sounding data correspond to the 300 mb level. It is apparent that clouds at this height were moving from  $220 - 230^{\circ}$  with speeds of  $18 - 19\text{ m s}^{-1}$ . The trailing edge of the lower cloud pattern, which corresponds to cloud top temperatures of  $-15$  to  $-17^{\circ}\text{C}$  ( $\sim 500 - 600$  mb), were moving with a velocities of  $15 - 17\text{ m s}^{-1}$  from  $240 - 255^{\circ}$ . Tracking of features from the radar images (not shown) indicates that the recognizable rain bands within the system were moving from  $225 - 235^{\circ}$  with speeds ranging from  $16 - 22\text{ m s}^{-1}$ .

## 2.4 Surface Observations

Surface observations provide a useful record of the weather associated with the specific features of the storm. They can also be used to verify the time of passage of the fronts and cloud/precipitation bands as determined from the other means of data acquisition (charts, satellite images, radar images, radiosonde data). Surface observations were performed by ship personnel on an hourly basis at the Oceanographer and every three hours at the Vancouver. Shipboard instruments recorded a number of variables every 30 seconds at the Vancouver. A quality check was performed on this nearly continuous data by comparing a single reading with a running ten-minute mean. If the measurement was within a predetermined deviation from the mean ( $2^{\circ}\text{C}$ ,  $20^{\circ}$  in wind direction,  $2\text{ m s}^{-1}$ ) it was considered representative. If between 1 and 6 consecutive measurements were not near the mean then they were discarded and replaced with linearly interpolated values as

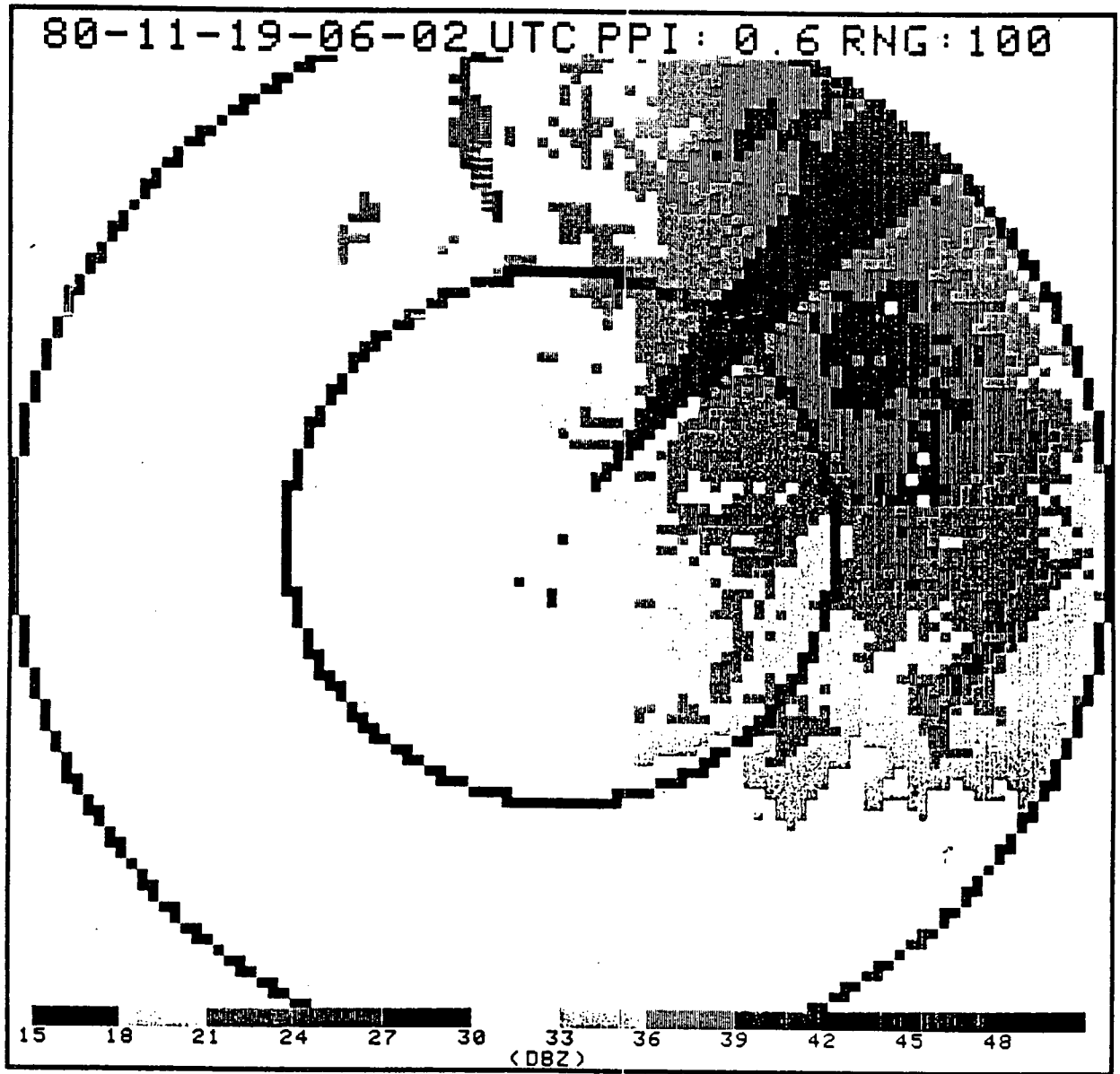


Figure 2.5: PPI radar imagery from the ship Vancouver: 0602 UTC 19 November 1980.

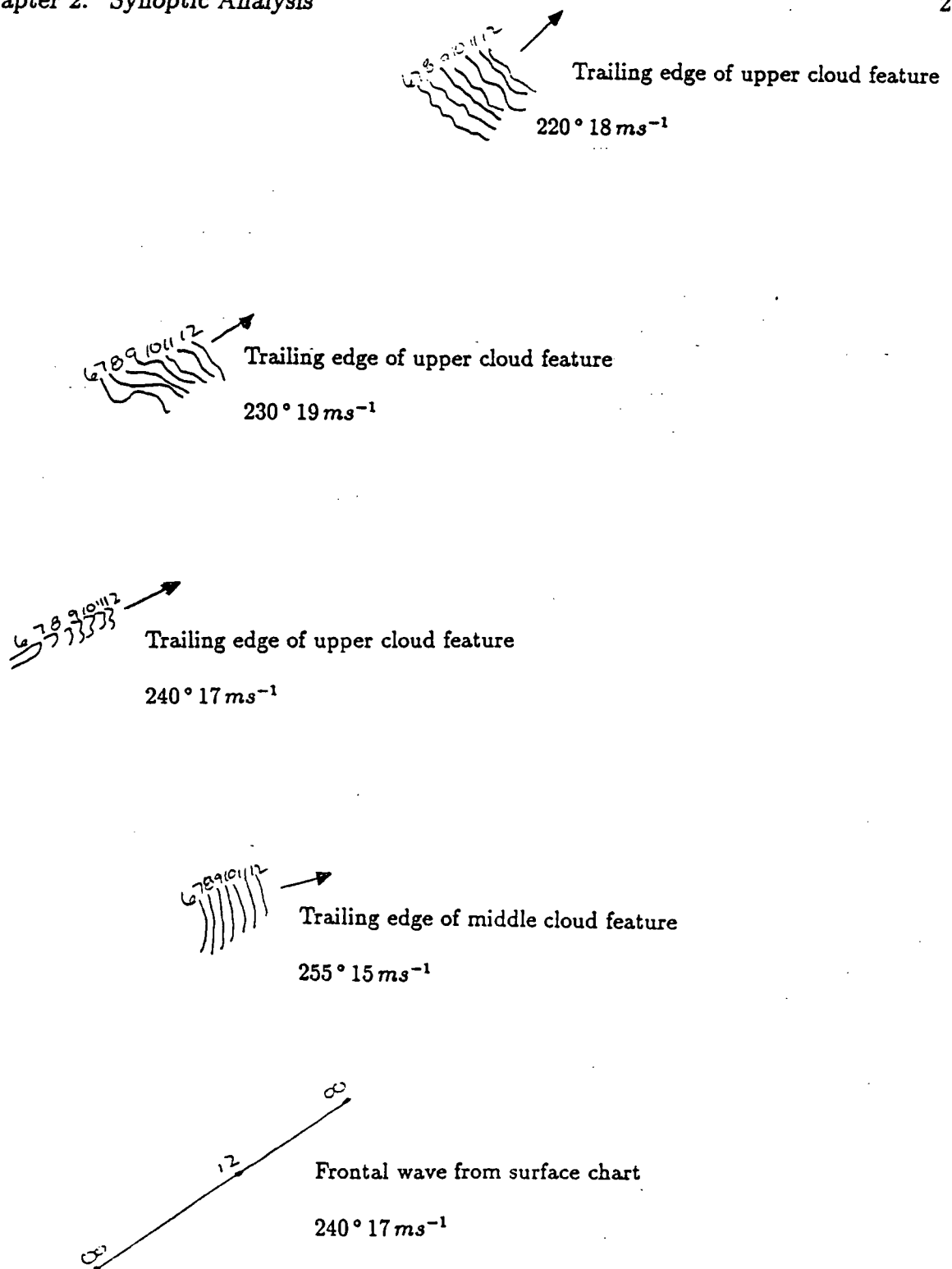


Figure 2.6: Motions of recognizable cloud and precipitation features from GOES imagery. Upper ( $\sim 300$  mb) and Lower trailing edge ( $\sim 550$  mb) features.

they were assumed to be noise in the data. If 6 or more consecutive measurements were away from the mean however, this was determined to be persistent enough to represent a change in the quantity and not just noise, and therefore the measurements were kept in the series.

The corrected time series for the Vancouver was then smoothed via a 10 minute mean and plotted in Figure 2.7. The hourly weather reports from the ship Oceanographer were similar to this series except that the U.S. ship observed either intermittent or continuous light rain from 0600 UTC through the rest of 19 November. At 0003 UTC on 19 November the pressure at the Vancouver was high (1005 mb) but falling rapidly ( $2 - 4 \text{ mbh}^{-1}$ ) and the sky was  $3/4$  obscured with stratocumulus clouds. The temperature was just below  $8^\circ\text{C}$  and the wet bulb depression was about  $1^\circ\text{C}$ . By 0600 UTC the sky was  $7/8$  covered by stratus and altostratus cloud and the pressure stopped its rapid fall and remained nearly constant for the next three hours. A short time later (near 0620 UTC) the wind began to swing around to the southwest. At the same time  $T_a$  rose by nearly  $2^\circ\text{C}$  and  $T_w$  rose by more than  $2^\circ\text{C}$ . In light of the moderating influence caused by the large heat capacity of the ocean these temperature changes are substantial. Since the change in each of these variables occurred at virtually the same time the conclusion is drawn that the surface warm front passed by the Vancouver at 0625 UTC. This time also corresponds to the time of ceasing of light rain that had been falling for the previous two hours.

The warm sector of this system was characterized by winds from the southwest, steady pressure, and relatively high  $T_a$  and  $T_w$  with the wet-bulb depression less than  $0.5^\circ\text{C}$ . The 0900 UTC surface observation reported skies that were fully obscured by stratus clouds. Light rain began to fall again by 0920 UTC and at 0945 UTC the wind began to shift to a westerly and  $T_a$  and  $T_w$  began to fall simultaneously. By 0955 UTC rain had stopped and pressure began to rise steadily. Shortly after 1000 UTC the wind direction became steady as did the temperatures with the wet-bulb depression depression

increasing to  $2^{\circ}\text{C}$ .

Based on the wind shift, the temperature changes, the change in pressure tendency, and the satellite pictures we conclude that the surface cold front passed the ship at 0950 UTC. The times of frontal passage for both fronts as determined previously by the synoptic charts correspond closely with those indicated by the surface data.

Over the next five hours, the pressure continued its steady rise and the temperatures and the wind direction remained relatively constant. The amount of cloud cover reduced throughout this period such that at 1200 UTC there was 4/8 stratocumulus and only 1/8 stratocumulus observed by 1500 UTC.

## 2.5 System Motion

On the basis of the tracking from the satellite images and from the surface analysis we conclude that the surface trough, surface fronts, and clouds were moving with a velocity of  $17\text{ m s}^{-1}$  from  $240^{\circ}$  ( $\pm 2\text{ m s}^{-1}$  and  $15^{\circ}$ ). While it is clear that some features, especially precipitation bands, embedded within the cyclone were moving with different velocities, this is the best estimate of motion of the large scale features of the storm. Hereafter a new coordinate system will be used with axes along and perpendicular to the direction of motion. The x-axis will be positive at  $60^{\circ}$  and negative at  $240^{\circ}$  (perpendicular to the front, along the direction of motion), called East and West respectively. Similarly, y will be positive (North) at  $330^{\circ}$  and negative (South) at  $150^{\circ}$  (along the front, perpendicular to the direction of motion). The origin ( $x = 0, y = 0$ ) will be at the ship Vancouver as the cold front is passing the ship (0950 UTC November 19) and will move with the system. Based on a qualitative analysis of the data we conclude that any evolution of the system over the 24 hours of interest was small and that we can treat the system as simply advecting. There are two main reasons for this assumption. First is that

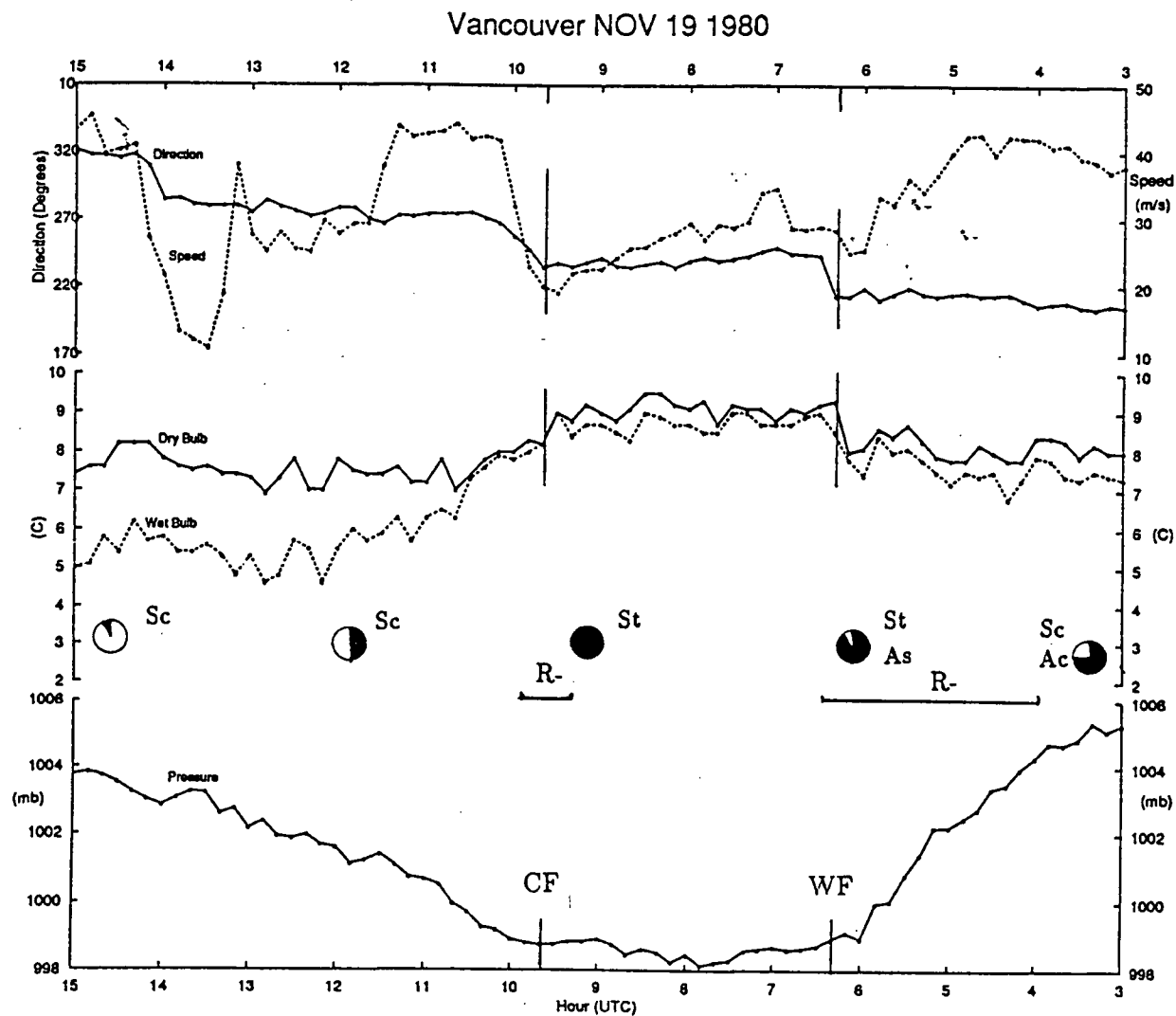


Figure 2.7: Time series of meteorological variables measured at the ship Vancouver. Shaded area of circle represents fraction of sky obscured with cloud. Ac, As, Sc, and St refer to altocumulus, altostratus, stratocumulus, and stratus clouds respectively. R- refers to light rain and the lines underneath show the duration of the rain. Long vertical lines indicate the time of passage of the surface cold front (CF) and warm front (WF) respectively.

features on satellite images are very similar from one image to the next. Secondly, the temperatures, dew-point depressions, and wind velocities in each sector of the storm remain nearly constant as the system moves through the study area.

Therefore, measurements at the Oceanographer will be regarded as being 180 *km* farther to the south along the cold front than those at the Vancouver.

## 2.6 Composite Plan View

Figure 2.8 shows a plan view of the system by compositing the information presented in this chapter. The scalloped area indicates the extent of the cloud with mid-level tops and the bold areas are the areas with higher tops. The stippling shows the main areas of precipitation and a composite surface observation has been plotted for each of the three main sectors of the storm.

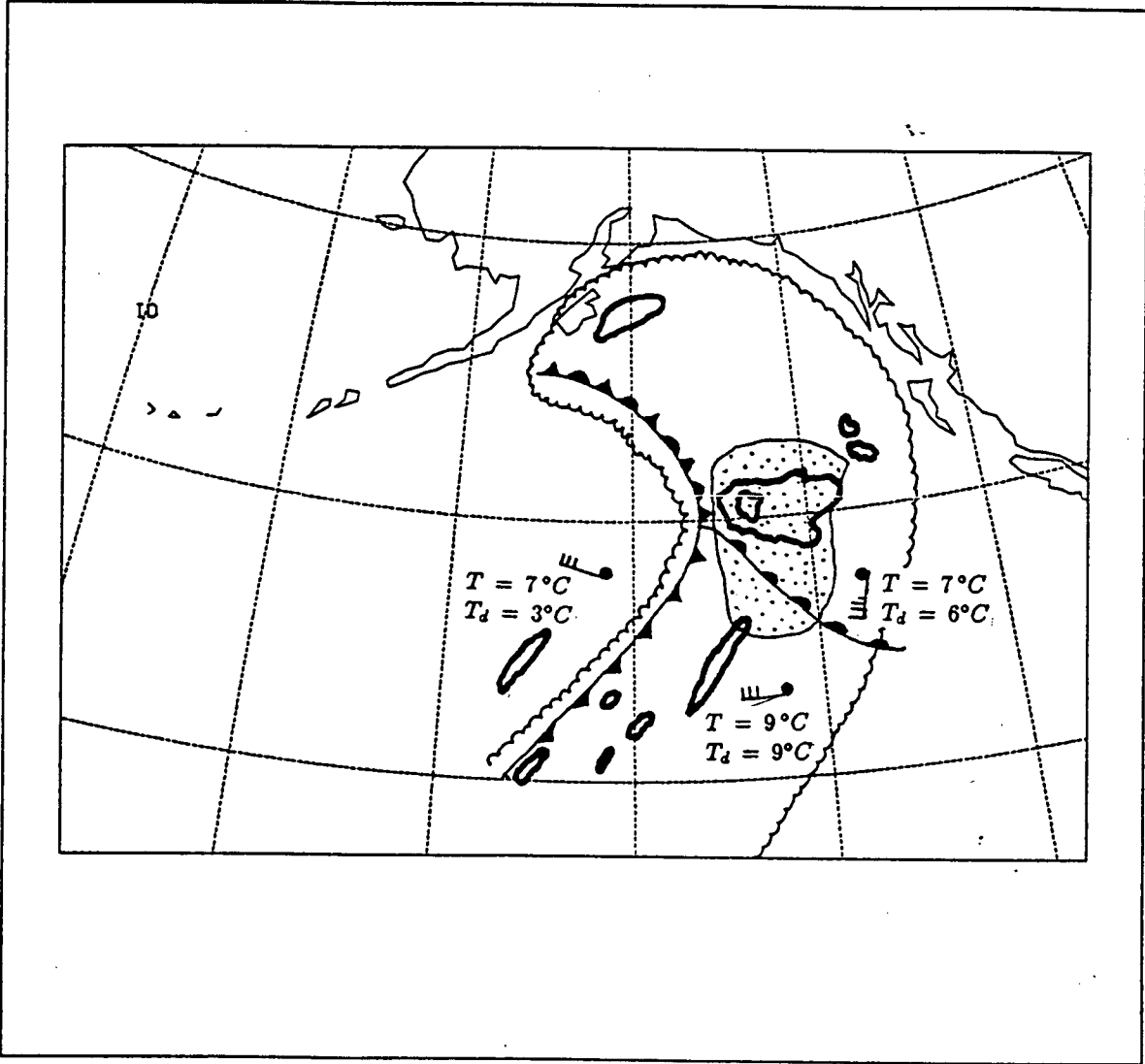


Figure 2.8: Composite plan view of system as described in text.

## Chapter 3

### Thermal and Moisture Structure

#### 3.1 Introduction

Radiosonde balloons were released every three hours from each ship and the data gathered from these ascents has been used to construct pressure-time cross sections through the front. The cross-sections consist of seven releases (at times shown by the upward tick marks on the bottom of cross-sections) along the horizontal axis while the vertical axis indicates the standard  $50\text{ mb}$  increments that the data were interpolated onto. In order to produce these plots the assumption was made that the balloons rose vertically through the atmosphere to at least  $400\text{ mb}$ . This is a valid assumption since a  $10\text{ m s}^{-1}$  wind would lead to horizontal advection of around  $10\text{ km}$  (which will be shown later to be  $\sim 5\%$  of the distance between soundings) in the  $20\text{ mins}$  taken by the balloon to reach  $400\text{ mb}$ . Using the speed of the system as determined in the previous section ( $17\text{ m s}^{-1}$ ) the three hours between balloon releases corresponds to  $184\text{ km}$  in the horizontal. Cross-sections based on data from the Oceanographer were through the front  $180\text{ km}$  to the south of those for the Vancouver. Gradients in the cross-frontal and vertical directions were computed by performing two-dimensional cubic spline interpolations on the data and then calculating the derivatives. Gradients in the along-frontal direction were determined by the differences between the cross-sections through the two ships after the fronts had been aligned at each ship. Since each  $y$ -derivative relies on the difference between only two points, extra care was taken to corroborate these findings with estimates

of the derivatives from the surface and upper air charts from the National Meteorological Centre data set and the STREX Meteorological Atlas (Reed and Mullen, 1981).

The pressure-time cross-sections can be interpreted as pressure-distance if we assume that the system was not evolving substantially over the period of interest. While there were certainly some changes in the system as it passed, the satellite images indicate that they were not large and that for the resolution of this study we can treat the system as simply advecting and not evolving, as discussed previously.

All computations of gradient fields were performed such that only contours with magnitudes larger than the uncertainty (probable error) for the term were plotted. The probable error was calculated following Barford (1986) such that the uncertainty  $\delta$  of a function  $\mathcal{F}(a, b, c)$  was determined in the following manner.

$$\delta\mathcal{F} = \left( \left( \frac{\partial\mathcal{F}}{\partial a} \delta a \right)^2 + \left( \frac{\partial\mathcal{F}}{\partial b} \delta b \right)^2 + \left( \frac{\partial\mathcal{F}}{\partial c} \delta c \right)^2 \right)^{\frac{1}{2}},$$

where  $\delta a$ ,  $\delta b$ , and  $\delta c$  are the uncertainties in the arguments of  $\mathcal{F}$ .

The uncertainty in the temperature measurements is  $\sim 1^\circ\text{C}$ , based on the work of McBean et al. (1986). The uncertainty in the speed of system motion ( $2\text{ m s}^{-1}$ ) leads to a probable error of  $\sim 21\text{ km}$  (or 11%) in the distance between soundings. This creates a probable error in the cross-frontal horizontal temperature gradients of  $0.7 \times 10^{-5}^\circ\text{C m}^{-1}$  ( $0.7^\circ\text{C } 100\text{ km}^{-1}$ ). The uncertainty in the north-south distance between soundings, based on the  $15^\circ$  uncertainty in the direction of motion, is  $70\text{ km}$ . This corresponds to an error in  $\partial\theta/\partial y$  of  $0.8 \times 10^{-5}^\circ\text{C m}^{-1}$  ( $0.8^\circ\text{C } 100\text{ km}^{-1}$ ). For the vertical derivatives, the error between vertical grid points was assumed to be 10%. This leads to an uncertainty in  $\partial\theta/\partial p$  of  $\sim 1.7 \times 10^{-3}^\circ\text{C mb}^{-1}$ .

### 3.2 Temperature and Relative Humidity

Figures 3.1 and 3.2 show cross-sections of temperature and relative humidity at the Vancouver and Oceanographer respectively. The two sections exhibit similar thermal patterns. The temperature contours in both cases indicate a region of strong baroclinicity, a large horizontal temperature gradient in the western portion that is evidence of the cold frontal zone as indicated by the heavy lines in both figures. These lines will be included in subsequent figures in order to show the frontal transition zones in relation to the other features. The upward and westward sloping isotherms of the transition zone indicate a width of approximately 120 km at the surface. Of course, the frontal zone may not have been this wide, but this is as narrow as could be resolved with the present data density. Figure 3.1, the Vancouver's cross-section, shows that the surface cold front, defined in the normal manner as the leading edge of the transition zone, corresponds to the time of passage of this feature as determined independently from the continuously recorded variables. Since only hourly surface measurements exist from the Oceanographer, we can only say that the surface cold front passage at this ship determined from the cross-section (figure 3.2) agrees with the time of passage as determined by the shipboard measurements ( $\sim 1600 UTC$ ) to within the resolution of the data.

The warm sector of elevated isopleths is clearly seen in both sections, however it is wider in figure 3.2 than in figure 3.1 since the system passed over the Oceanographer to the south of where it crossed the Vancouver.

Just to the east of the warm sector both sections show another region of significant baroclinicity. Although in the Vancouver's cross-section this second region of baroclinicity is weaker than that in the cold frontal zone the two areas of baroclinicity are of similar magnitude at the Oceanographer. These contours that slope downward and to

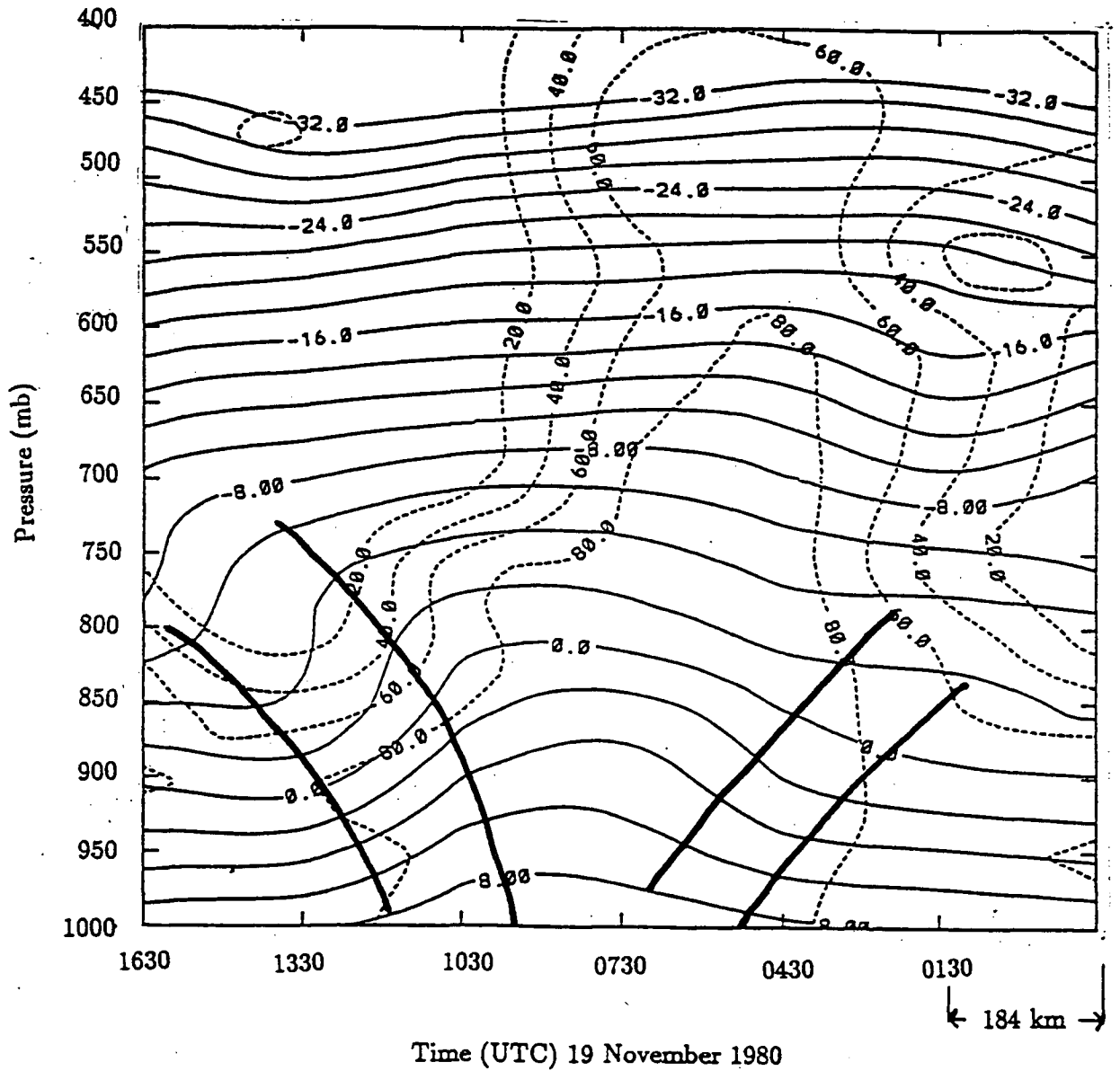


Figure 3.1: Time-Pressure cross section of Temperature (solid; contour interval  $2^{\circ}\text{C}$ ) and Relative Humidity (dashed; contour interval 20%) for the ship Vancouver. Heavy lines to the west and east represent the cold and warm frontal transition zones respectively.

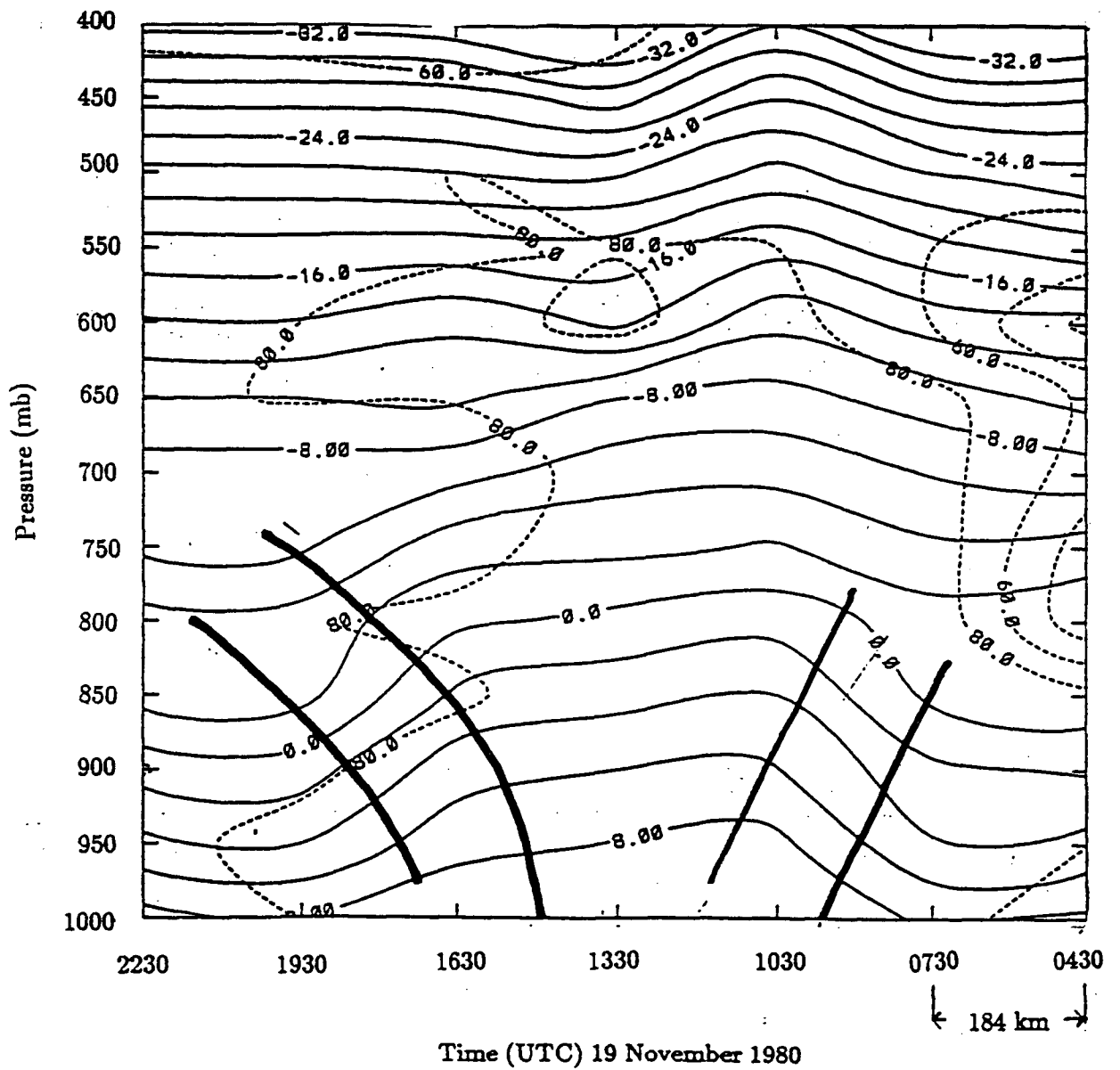


Figure 3.2: Time-Pressure cross section of Temperature (solid; contour interval  $2^{\circ}\text{C}$ ) and Relative Humidity (dashed; contour interval 20%) for the ship Oceanographer. Heavy lines to the west and east represent the cold and warm frontal transition zones respectively.

the east indicate the warm frontal zone with a transition region about 100 km wide at the Vancouver and  $\sim 120$  km in width at the Oceanographer. The passage of the surface front over the Vancouver (figure 3.1) again corresponds to the time as determined by the shipboard measurements as it does to within the data resolution at the Oceanographer.

Contours of relative humidity (RH) can give information regarding the cloud distribution. The areas of cloud from the satellite images roughly correspond to the regions of the section with RH values of 60 – 80% or greater. Figure 3.1 indicates that as the system passed through the Vancouver, the main cloud area was  $\sim 600$  km wide at the surface and narrowed and sloped towards the east until the tops were reached at  $\sim 300$  mb. The satellite (figure 2.4b) imagery supports this conclusion by showing that the cold front was just ahead of the trailing edge of low cloud and that the main area of cold cloud tops ( $-51.2$  °C to  $-60.2$  °C, or about 300 mb height) was located a considerable distance ( $\sim 400$  km) to the west of the surface cold front. The cloud observations made from the ships also support the cloud field inferred from the RH contours in figure 3.1. There is a strong moisture gradient west of the main cloud zone at about 725 mb directly above the surface cold front. This feature is similar to the upper cold fronts described by other authors (see Browning and Monk 1982; McBean and Stewart, 1991). Over this 140 km, the RH decreases from more than 80% to less than 20%. The cold frontal zone was very dry as it passed by the Vancouver, with a RH less than 20% everywhere above 750 mb. This dryness is indicative of air that has descended and therefore warmed; a kata-front.

As the system passed over the Oceanographer, to the south and west, the RH field appeared somewhat different (figure 3.2). The eastern half of the section was similar to that at the Vancouver, with the main area of  $RH \geq 80\%$  slightly ahead of the cold front and extending to near 500 mb in height. The 1930 UTC sounding was missing however, and this limits our confidence in the contours in the western edge of the section. Again, the GOES images can be used to support the inferences made from the RH contours.

The sharp moisture gradient that was directly above the surface cold front when the system passed the Vancouver is not evident as it passed the Oceanographer to the south. The beginning of precipitation at the Oceanographer ( $\sim 0600$  UTC) corresponds closely with the eastern edge of the high cloud region in figure 2.4b and with the region of strong moisture gradient in the eastern portion of the cross-section. The rain, which lasted the remainder of the day, did not cease with the passing of the region of cold cloud top temperatures (which, near 1500 UTC agrees to the  $RH = 80\%$  on the cross-section) however. These facts lead us to believe that the front was not a kata-front at the location of the southern section.

Variability in the along frontal direction is a likely explanation of the differences in the moisture fields. The lower cloud area is more extensive in the section through the Oceanographer since it is farther to the south and the warm sector of the system is wider than it is at the Vancouver. Also, the alignment of the region of high cloud tops suggests that the precipitation associated with them would occur over a longer time at the Oceanographer than it would at the Vancouver.

The pattern of temperature (at both ships) and moisture (at the Vancouver) isolines is remarkably similar to the storm of two days earlier that was studied by McBean and Stewart (1991); however it is quite different from the cold front of November 15 that Bond and Fleagle (1985) analysed.

The vertical soundings in figure 3.3 show typical profiles of temperature and dew point temperature in the three main sectors of system; pre-frontal, warm sector, and post-frontal. These profiles are strikingly close to those presented by Bond and Fleagle (1985) of the frontal system of four days earlier. Figure 3.4 shows a plot of potential temperature soundings based on air-sonde balloons that were released from the Vancouver. These air-sondes ascended more slowly than the radiosondes and therefore give higher resolution temperature data (every 5 seconds). Figure 3.4 indicates that the base of the inversion

capping the pre-frontal boundary layer was at about 700 m ( $\sim 920$  mb). Figure 3.3 shows that the pre-frontal boundary layer was near saturation and above this there was a layer from 800 – 550 mb that was quite dry. In the warm sector no well defined boundary layer existed (figure 3.4), which is similar to the Bond and Fleagle (1985) analysis of the near-frontal region. Figure 3.3 indicates that the profile was at or near saturation for virtually the entire height of the ascent in the warm sector. The post-frontal boundary layer appears to be slightly deeper than the pre-frontal one (figure 3.4) and shows the same moisture pattern of high moisture content in the boundary layer and much drier air above as the pre-frontal air (3.3). While the general structure of these soundings is similar to those of Bond and Fleagle (1985), their post-frontal boundary layer was nearly twice as deep as the pre-frontal case, whereas this storm exhibited similar pre and post-frontal boundary layer thicknesses. Figure 3.4 shows that both the pre and post-frontal boundary layers were well mixed with respect to  $\theta$ . The air in the lower regions of the warm sector was statically stable with respect to  $\theta$ .

### 3.3 Potential Temperatures

Contours of potential temperature,  $\theta$ , (figures 3.5 and 3.6) for both ships show the greatest concentration of isentropes in the frontal zones, primarily the cold front transition region for the Vancouver's cross-section. Both behind the cold front and ahead of the warm front, the boundary layer air was of nearly constant  $\theta$  in both the vertical and horizontal. Figure 3.7, the static stability field for the Vancouver, shows that most of the cross-section was slightly stable ( $\partial\theta/\partial p$  slightly less than 0) with respect to dry processes, except for an area of marked stability ( $\partial\theta/\partial p < 0$ ) in the upper part of the cold frontal zone where the maximum stability of  $-1^\circ\text{C}/10$  mb was observed. The static stability for the Oceanographer (not shown) showed a very similar pattern except for

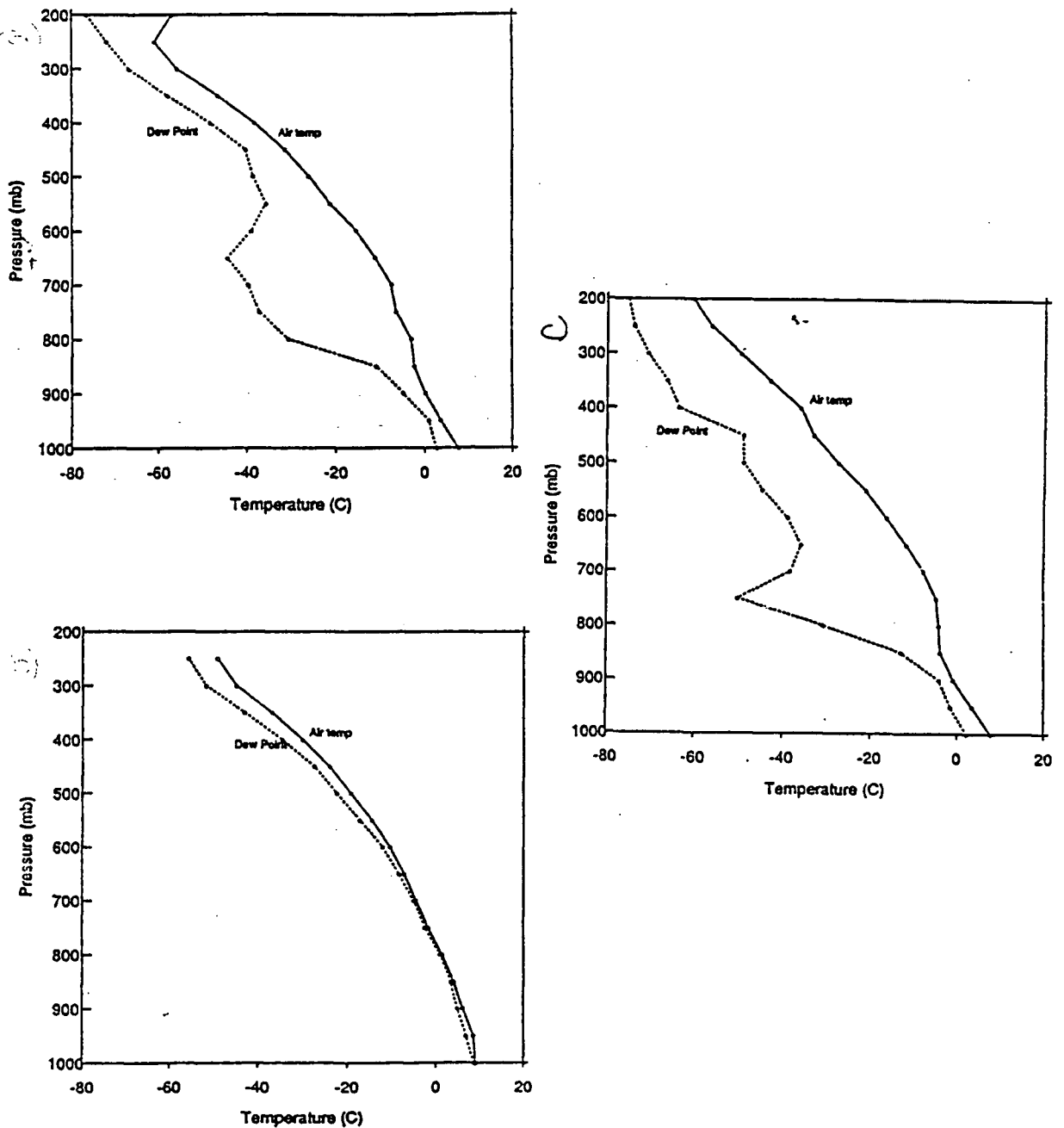


Figure 3.3: Temperature soundings for a) pre-warm frontal (Vancouver 0000 UTC), b) warm sector (Oceanographer 1200 UTC), and c) post-cold frontal (Vancouver 1500 UTC).

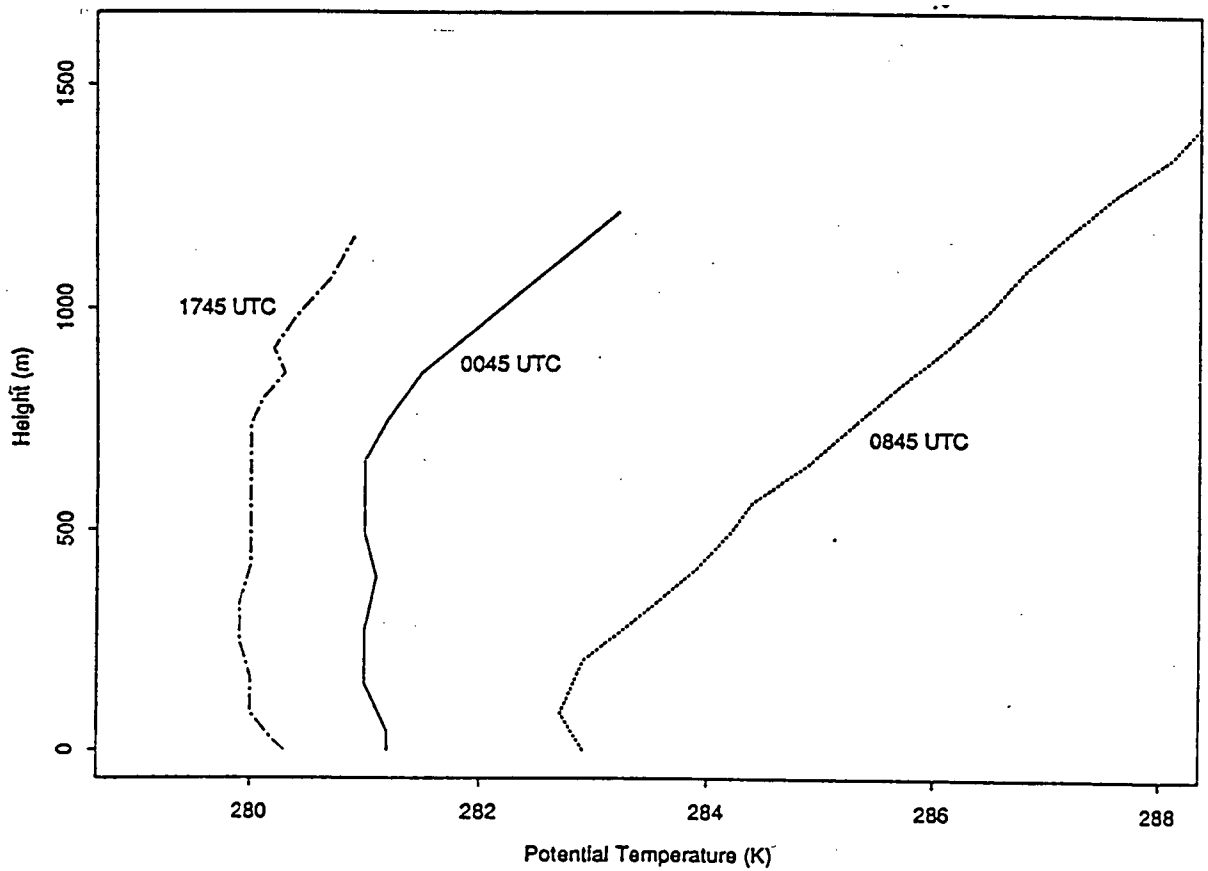


Figure 3.4: Potential temperature soundings for pre-warm frontal (0045 UTC), warm sector (0845 UTC), and post-cold frontal (1745 UTC) for the ship Vancouver.

another region of similarly strong stability in the upper warm frontal zone.

Rather than potential temperature, for the remaining analyses equivalent potential temperature,  $\theta_e$ , which is a conserved variable for pseudo-adiabatic processes will be used. The contours of  $\theta_e$  for the Vancouver and the Oceanographer are shown respectively in figures 3.8 and 3.9. Again, these two cross-sections show very similar patterns with cold air regions ( $\sim 22^\circ\text{C}$ ) both ahead of the warm front and behind the cold front in both sections. Warmer air (of either southern origin or which had undergone warming) existed in the warm sectors at both ships with the  $32^\circ\text{C}$  isotherm reaching down to  $750\text{ mb}$  at the Vancouver and to  $950\text{ mb}$  at the Oceanographer. In both sections equivalent potential temperatures also exhibit large gradients in the frontal zones, with the strongest occurring in the cold region at the Vancouver and the warm frontal zone at the Oceanographer.

At both ships the boundary layer was unstable in terms of  $\theta_e$  (figures 3.10 and 3.11,  $\partial\theta_e/\partial p > 0$ ) both behind the cold front and ahead of the warm front with the largest  $\partial\theta_e/\partial p$  of  $0.9^\circ\text{K}(10\text{ mb})^{-1}$  about  $400\text{ km}$  behind the cold front in each figure. There was the same area of marked stability in the upper cold frontal zone as with respect to  $\theta$  with a maximum magnitude of  $\partial\theta_e/\partial p = -1.4^\circ\text{K}(10\text{ mb})^{-1}$  at  $800\text{ mb}$  in the Vancouver's section and  $-1.0^\circ\text{K}(10\text{ mb})^{-1}$  at  $725\text{ mb}$  for the Oceanographer. The remainder of the cross-sections were nearly neutrally stratified ( $\partial\theta_e/\partial p \simeq 0$ ) except for the upper regions of the warm frontal zone at the Oceanographer where there was another region of marked stability of  $\partial\theta_e/\partial p = -1.4^\circ\text{K}(10\text{ mb})^{-1}$ . McBean and Stewart (1991) found similar patterns and magnitudes for their storm as did Hsie et. al. (1984) in their model results.

The cross-frontal horizontal gradients of  $\theta_e$  are shown in figures 3.12 and 3.13. Both cold frontal zones exhibit positive values of  $\partial\theta_e/\partial x$  with the largest value for the Vancouver of  $6.5 \times 10^{-5}^\circ\text{K m}^{-1}$  at about  $900\text{ mb}$  in the cold frontal zone. The cold frontal zone at the Oceanographer also exhibited a peak in this field, however at  $3.5 \times 10^{-5}^\circ\text{K m}^{-1}$

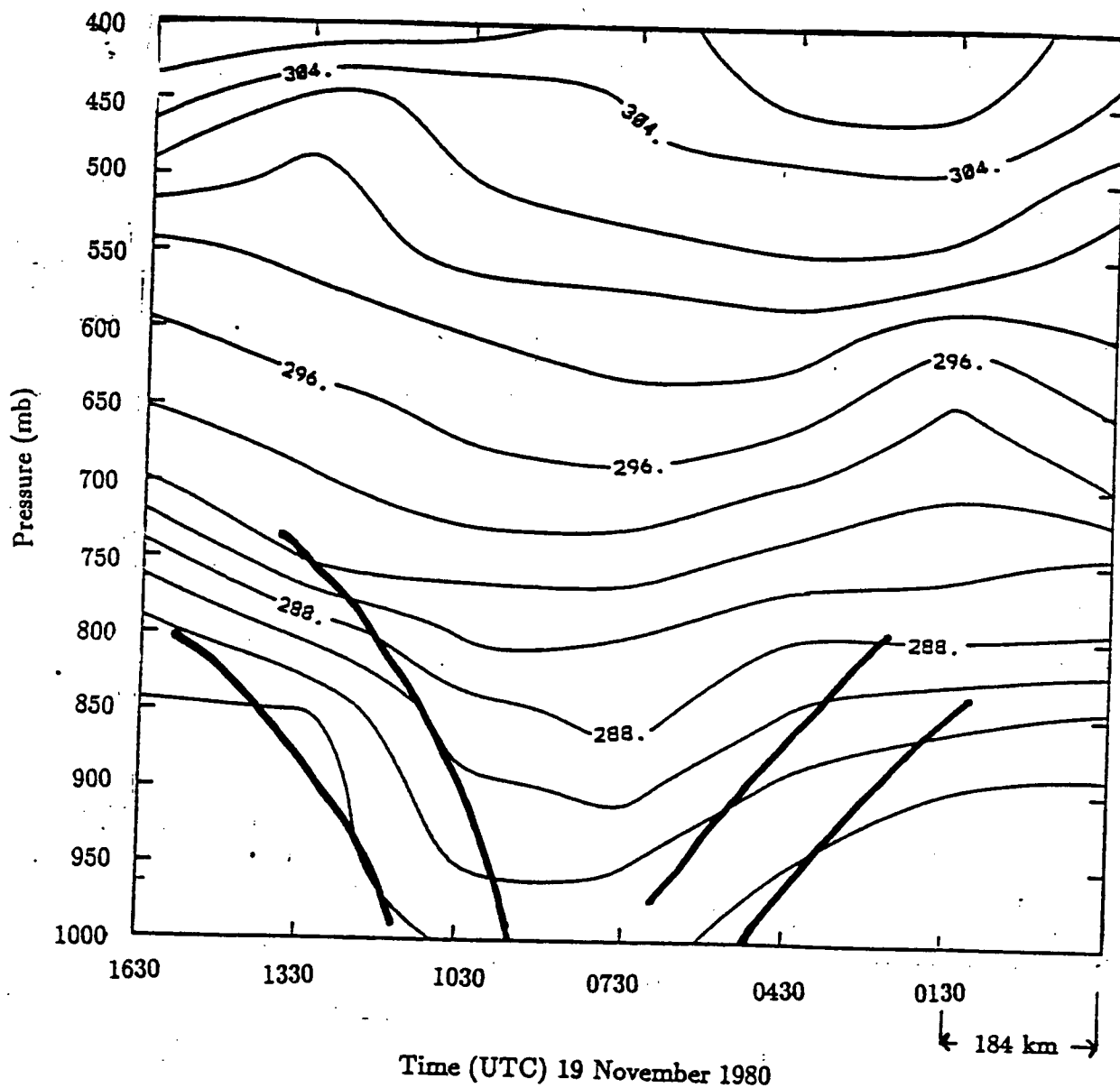


Figure 3.5: Time-Pressure cross section of Potential Temperature at the ship Vancouver (contour interval  $2^{\circ}K$ ).

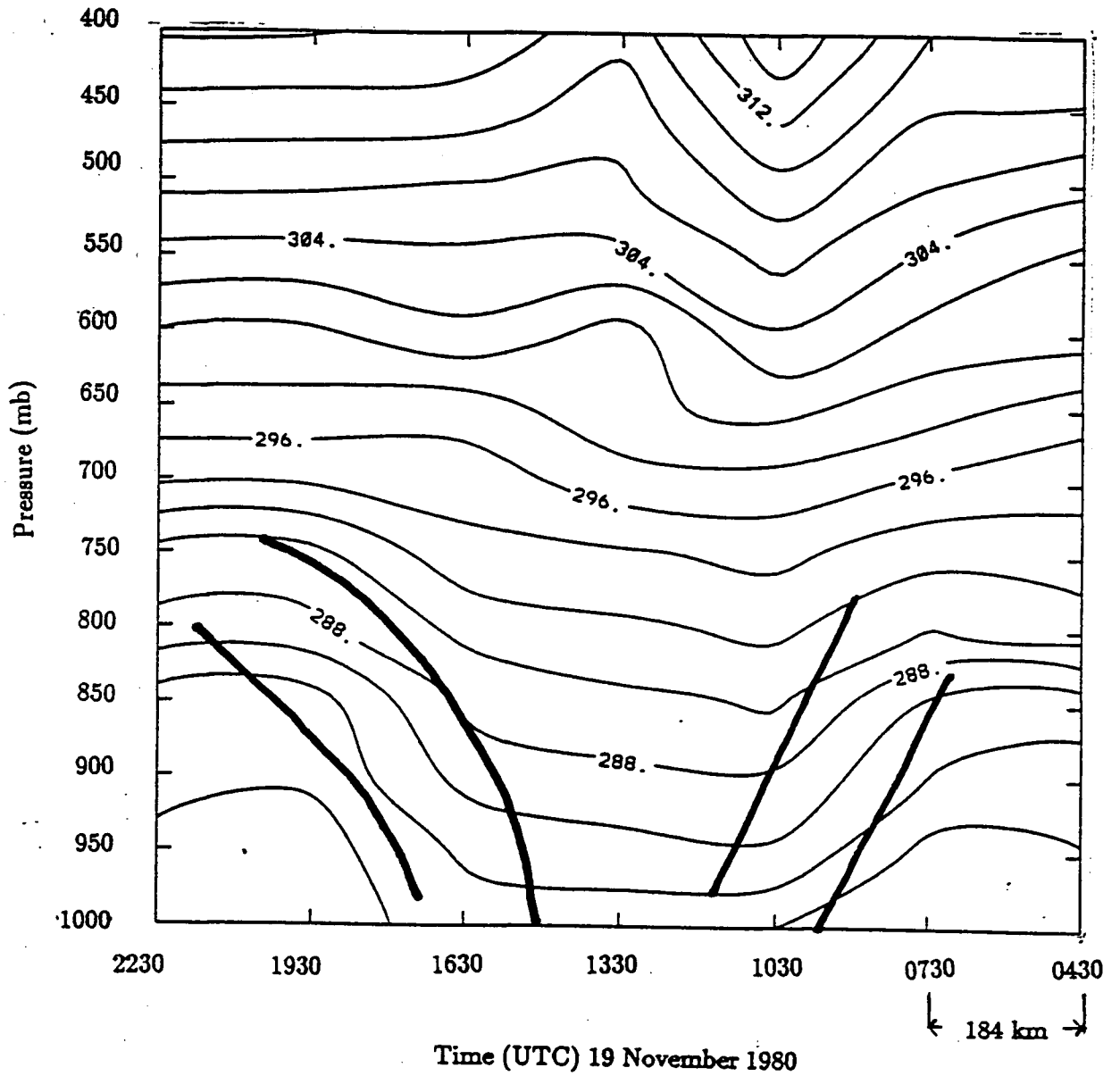


Figure 3.6: Time-Pressure cross section of Potential Temperature at the ship Oceanographer (contour interval  $2^{\circ}K$ ).

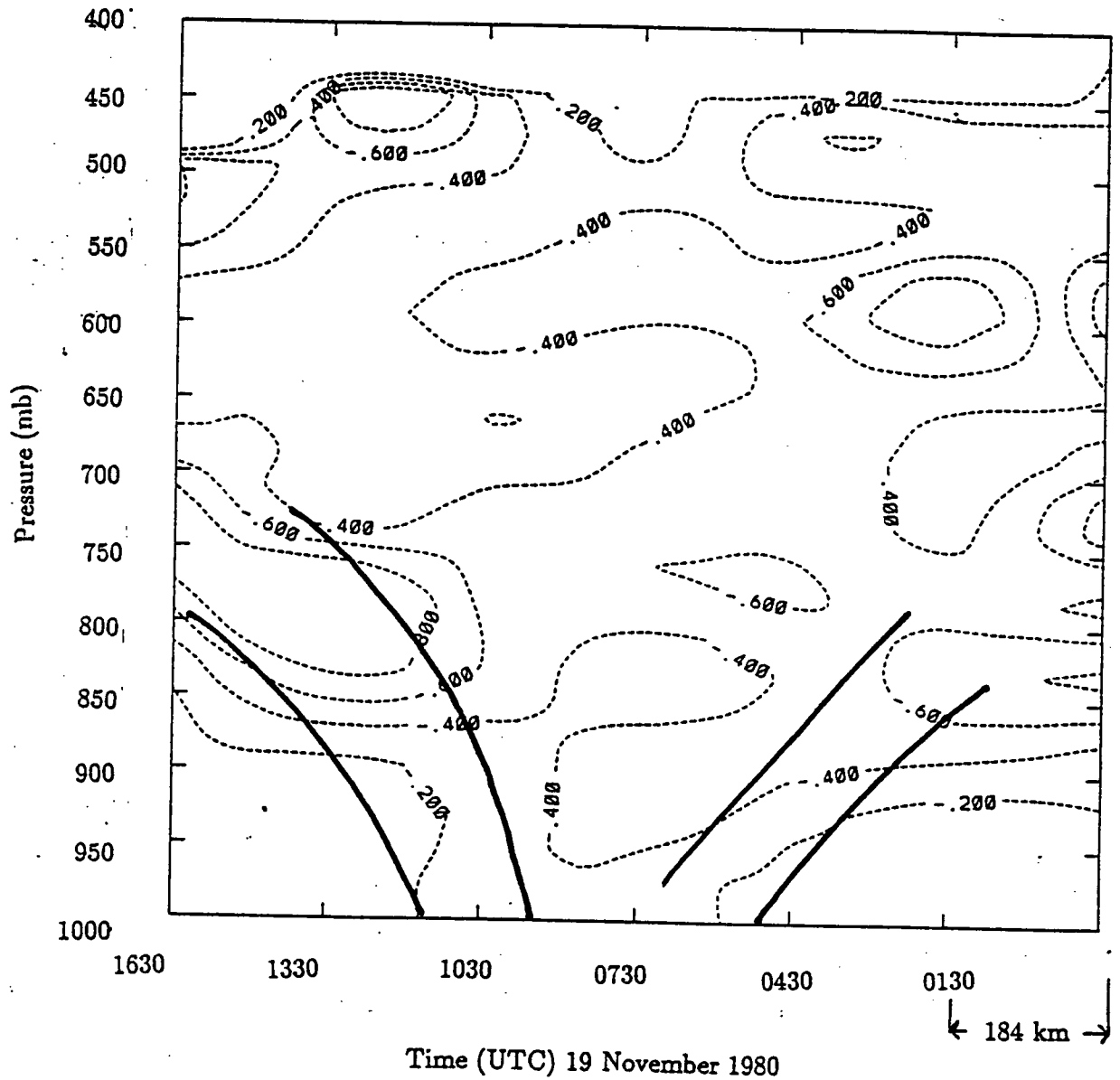


Figure 3.7: Time-Pressure cross section of  $\frac{\partial\theta}{\partial p}$  at the ship Vancouver. Dashed lines indicate negative values (Units  $\frac{^{\circ}K}{10mb}$ ).

near 900 *mb* it was smaller in magnitude than that for the northern section. The warm frontal zones each show negative values of  $\partial\theta_e/\partial x$  with the maximum magnitude at the Oceanographer of  $-6.5 \times 10^{-5} \text{ }^\circ\text{K m}^{-1}$  nearly twice as large as that at Vancouver. These cross-frontal gradients are also similar to those calculated by McBean and Stewart (1991) and Hsie et al., (1984).

The along frontal gradient of equivalent potential temperature,  $\partial\theta_e/\partial y$  is shown in figure 3.14. As a result of the technique used to calculate these values, along-frontal derivatives are only shown at the Vancouver. The cold frontal zone exhibits peak values of this gradient of  $-3.0 \times 10^{-5} \text{ }^\circ\text{K m}^{-1}$  at 875 *mb*. The other region of high gradients lies just to the west of the warm front at 800 *mb* where the same magnitude is reached. These values are in close agreement with the 850 and 700 *mb* National Meteorological Centre analyses shown in figure 2.3.

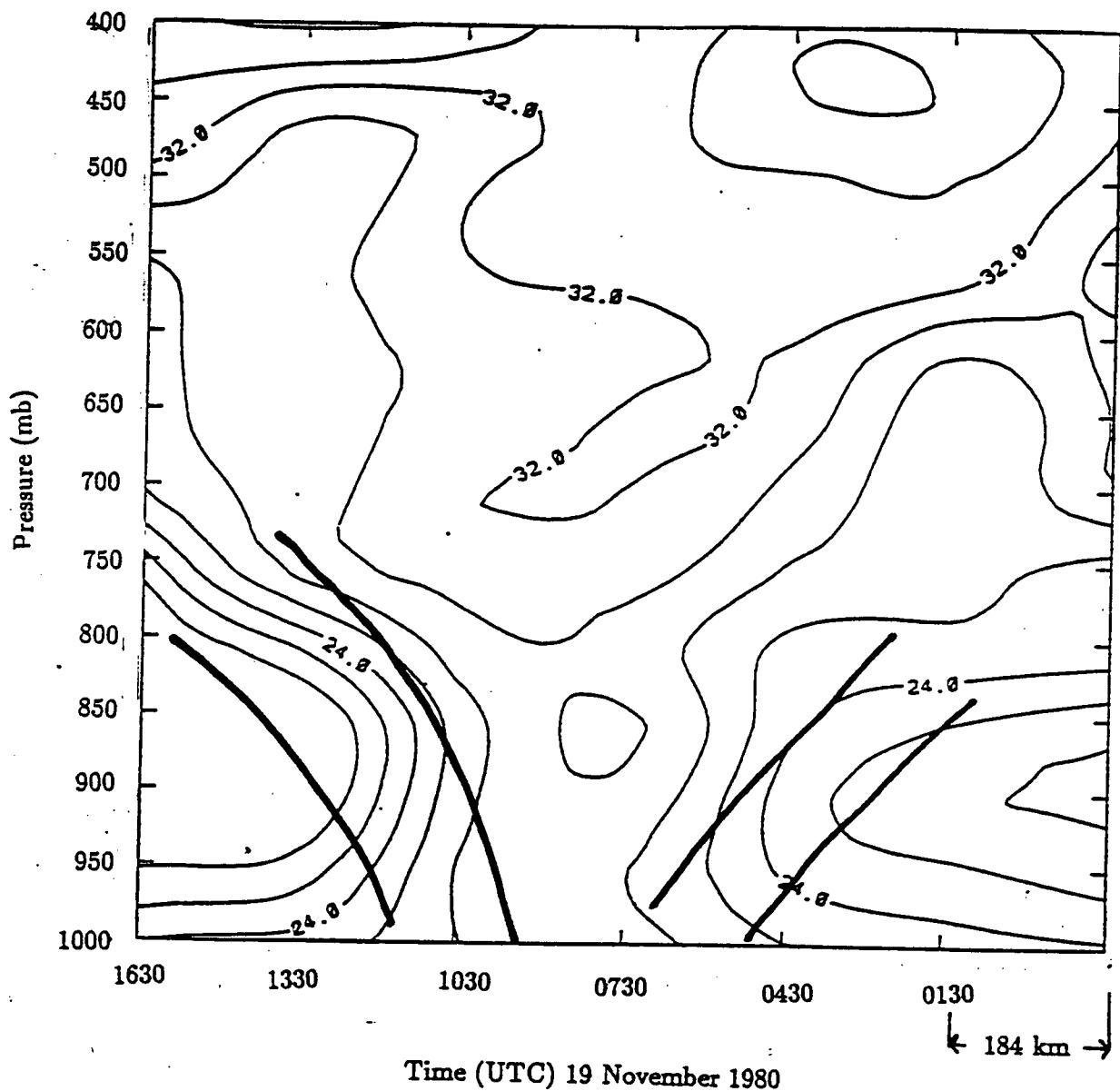


Figure 3.8: Time-Pressure cross section of Equivalent Potential Temperature at the ship Vancouver (contour interval 2°C).

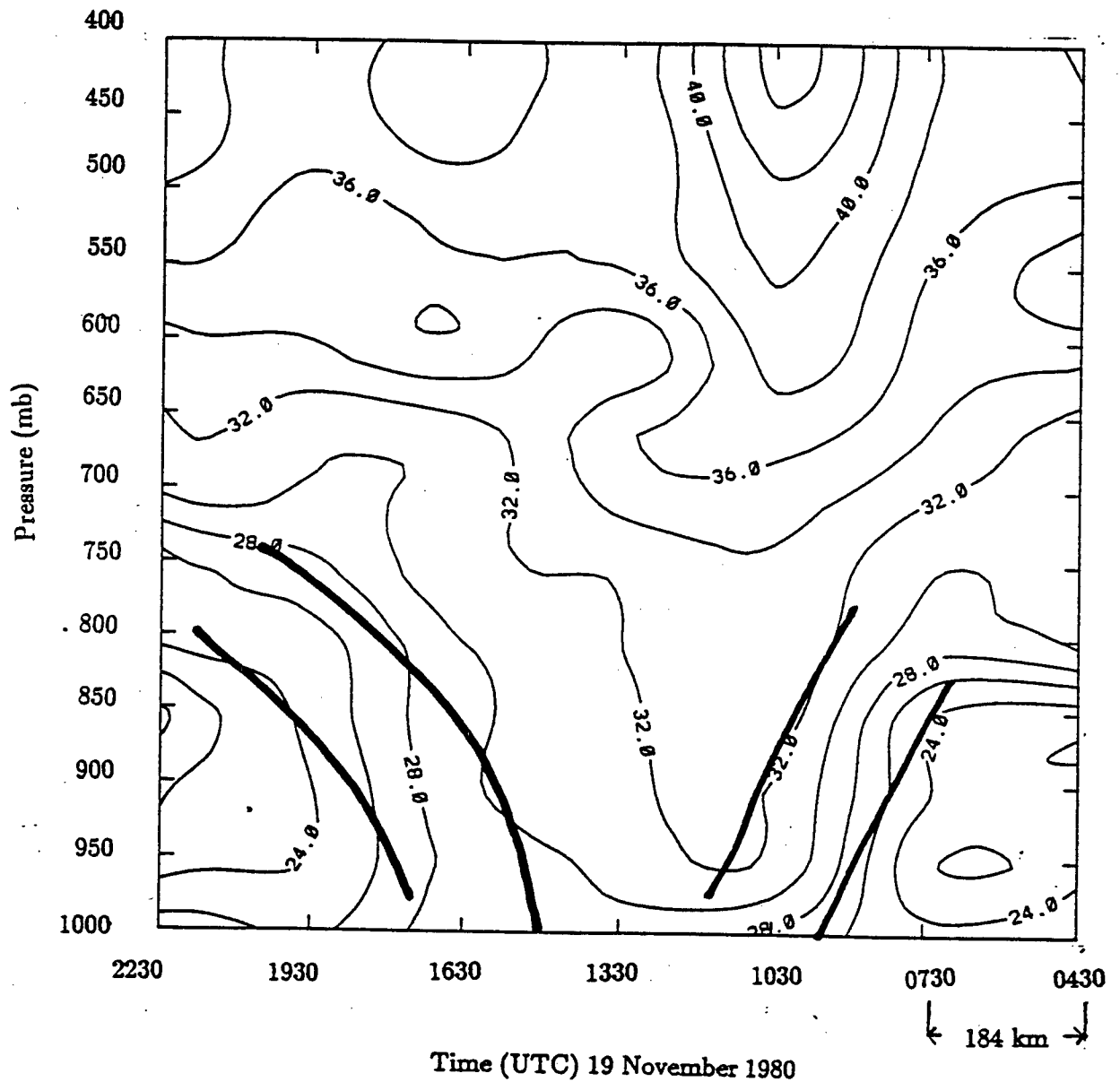


Figure 3.9: Time-Pressure cross section of Equivalent Potential Temperature at the ship Oceanographer (contour interval  $2^{\circ}\text{C}$ ).

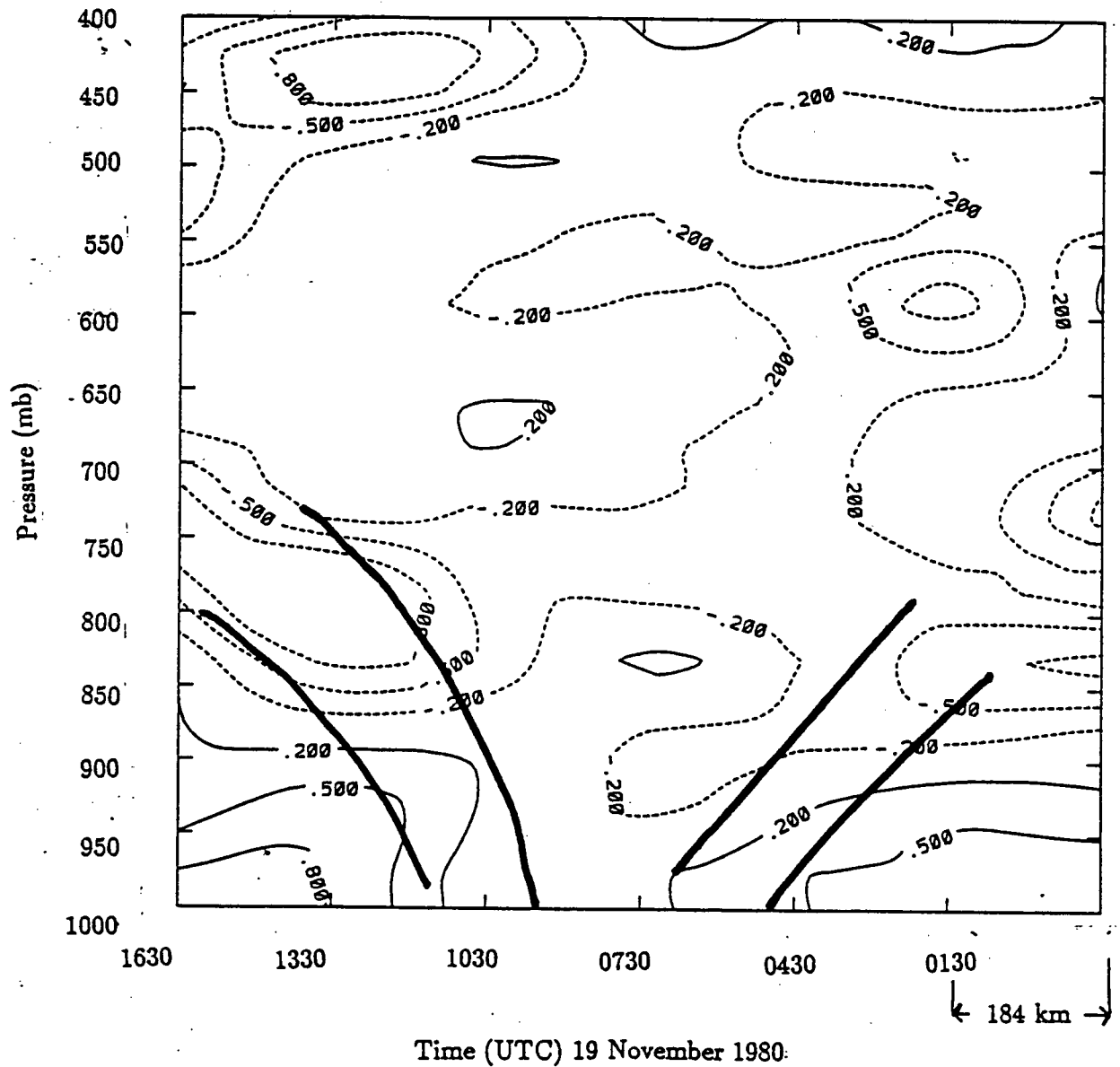


Figure 3.10: Time-Pressure cross section of  $\frac{\partial \theta_s}{\partial p}$  at the ship Vancouver. Dashed lines indicate negative values (Units  $\frac{^{\circ}K}{10mb}$ ).

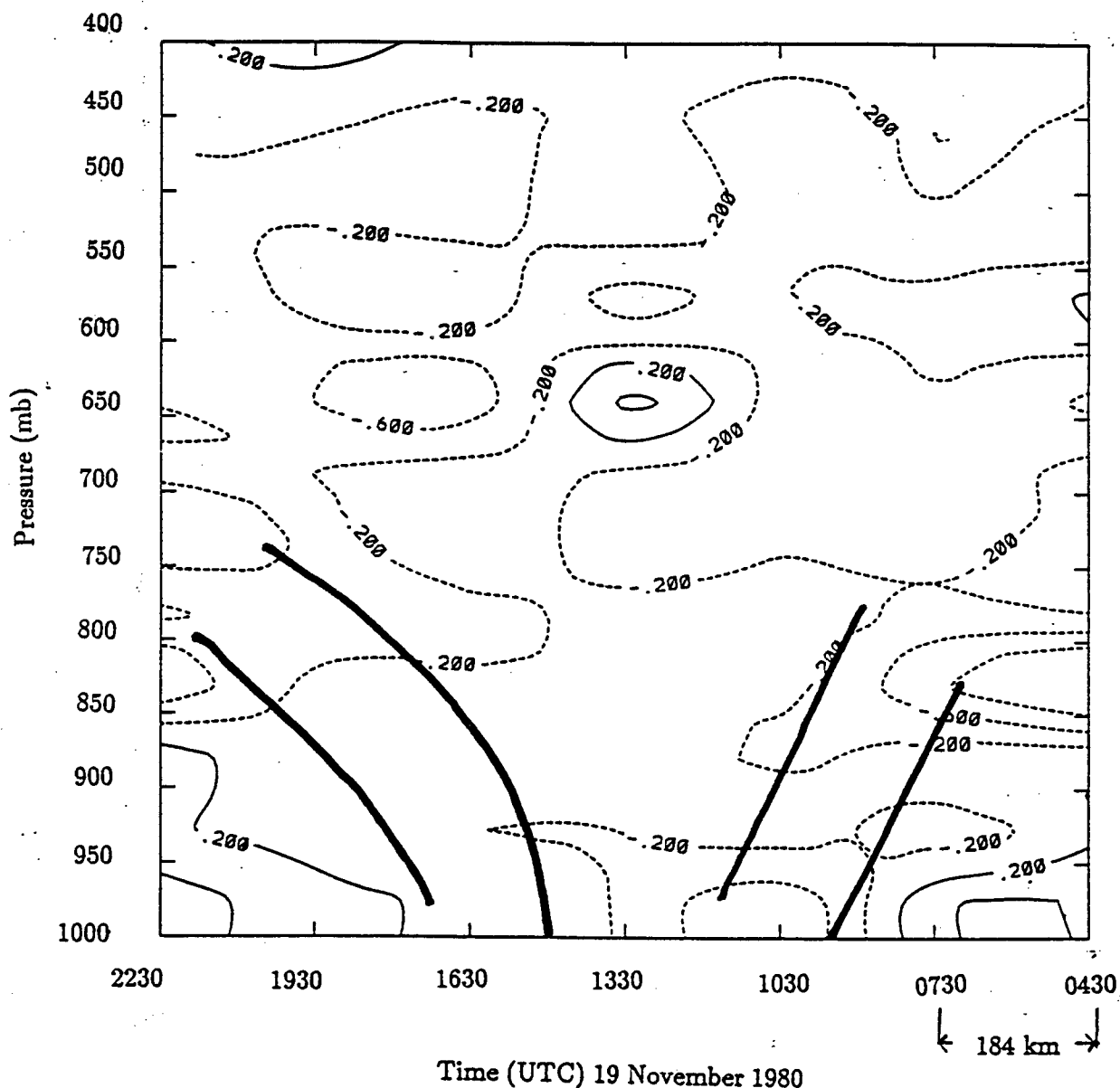


Figure 3.11: Time-Pressure cross section of  $\frac{\partial \theta_e}{\partial p}$  at the ship Oceanographer. Dashed lines indicate negative values (Units  $\frac{^{\circ}K}{10mb}$ ).

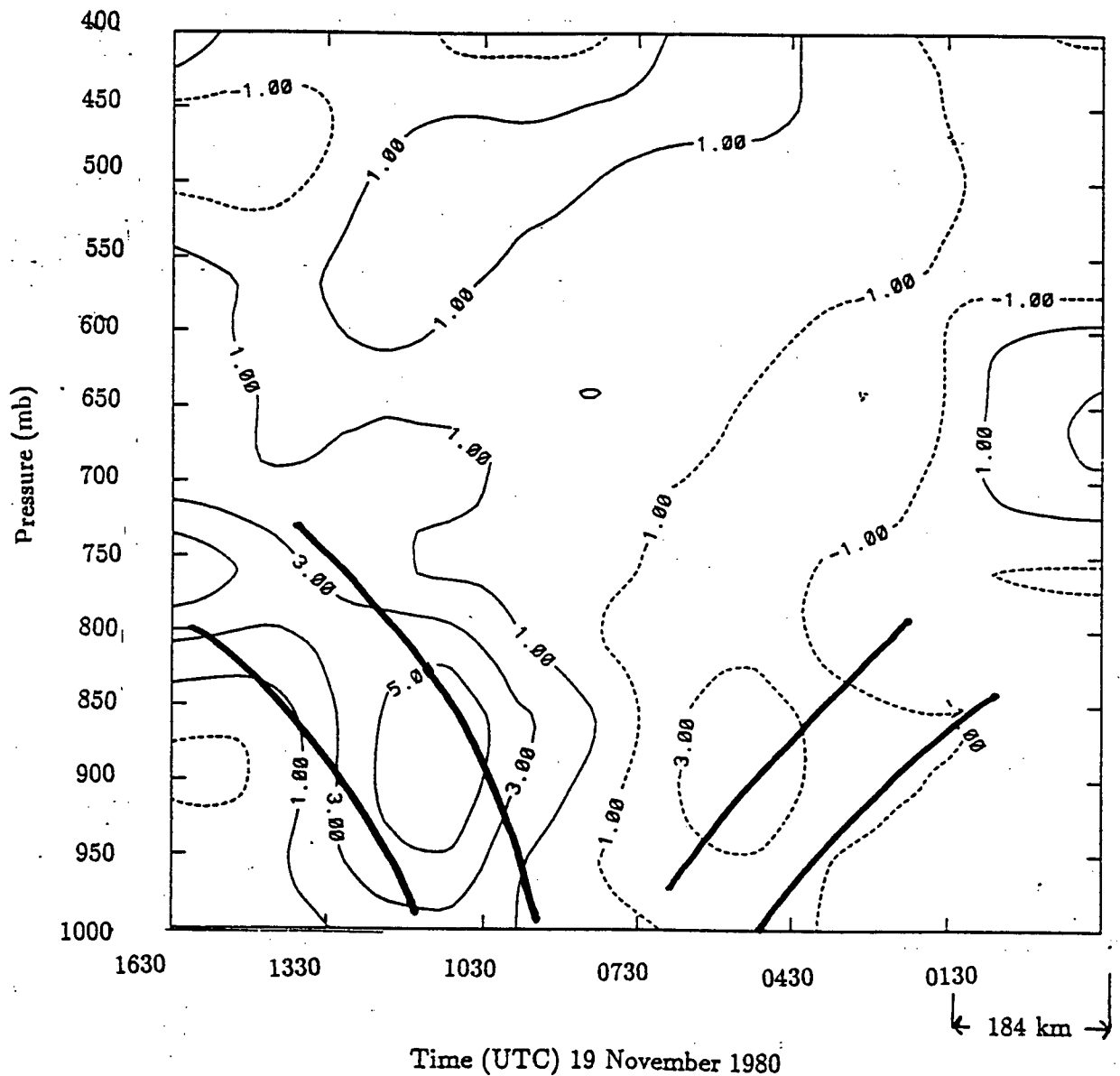


Figure 3.12: Time-Pressure cross section of  $\frac{\partial \theta_e}{\partial x}$  at the ship Vancouver. Dashed lines indicate negative values (Units  $10^{-5} \text{ } ^\circ\text{K m}^{-1}$ ).

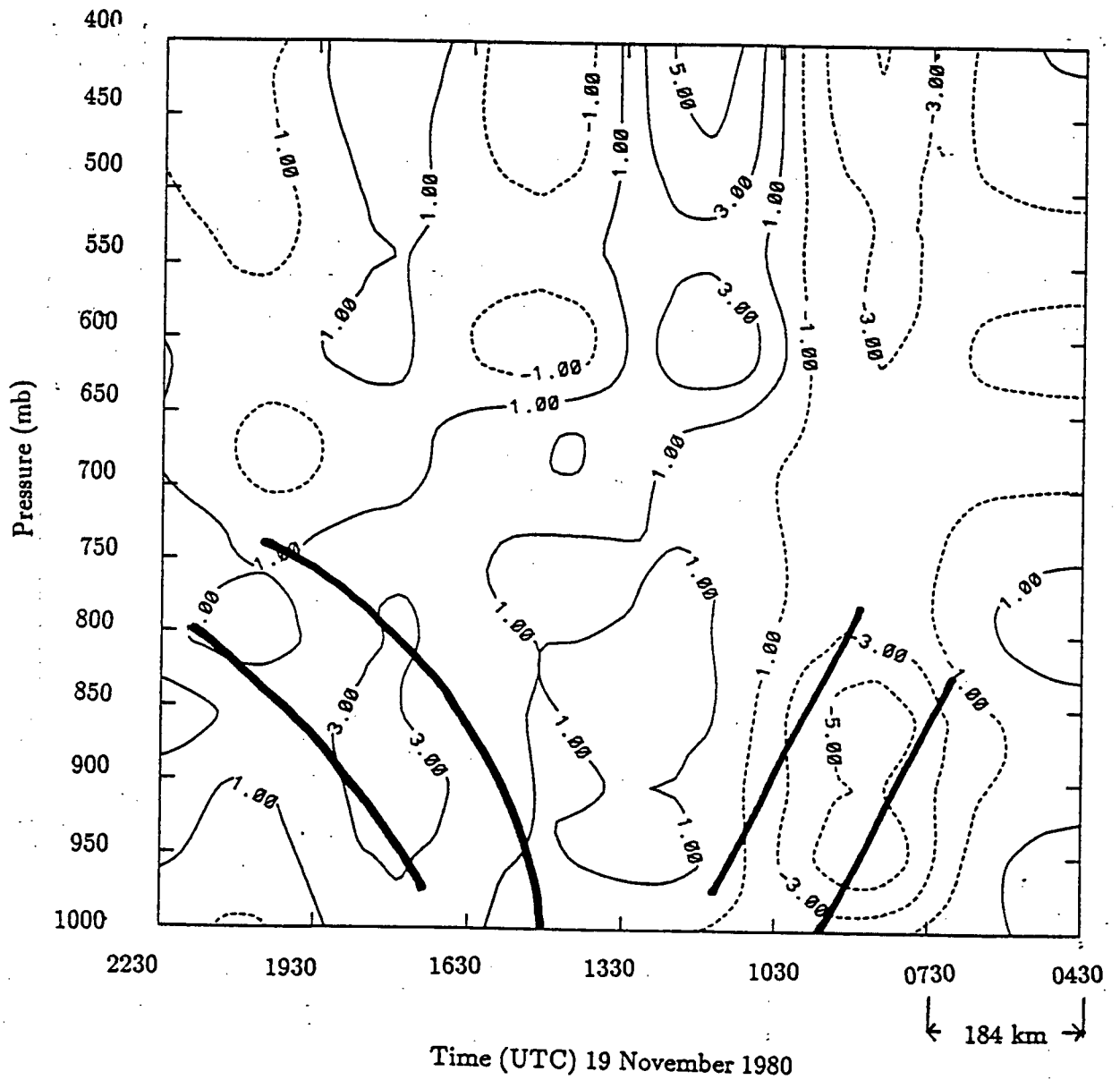


Figure 3.13: Time-Pressure cross section of  $\frac{\partial \theta_z}{\partial x}$  at the ship Oceanographer. Dashed lines indicate negative values (Units  $10^{-5} \text{ } ^\circ K \text{ m}^{-1}$ ).

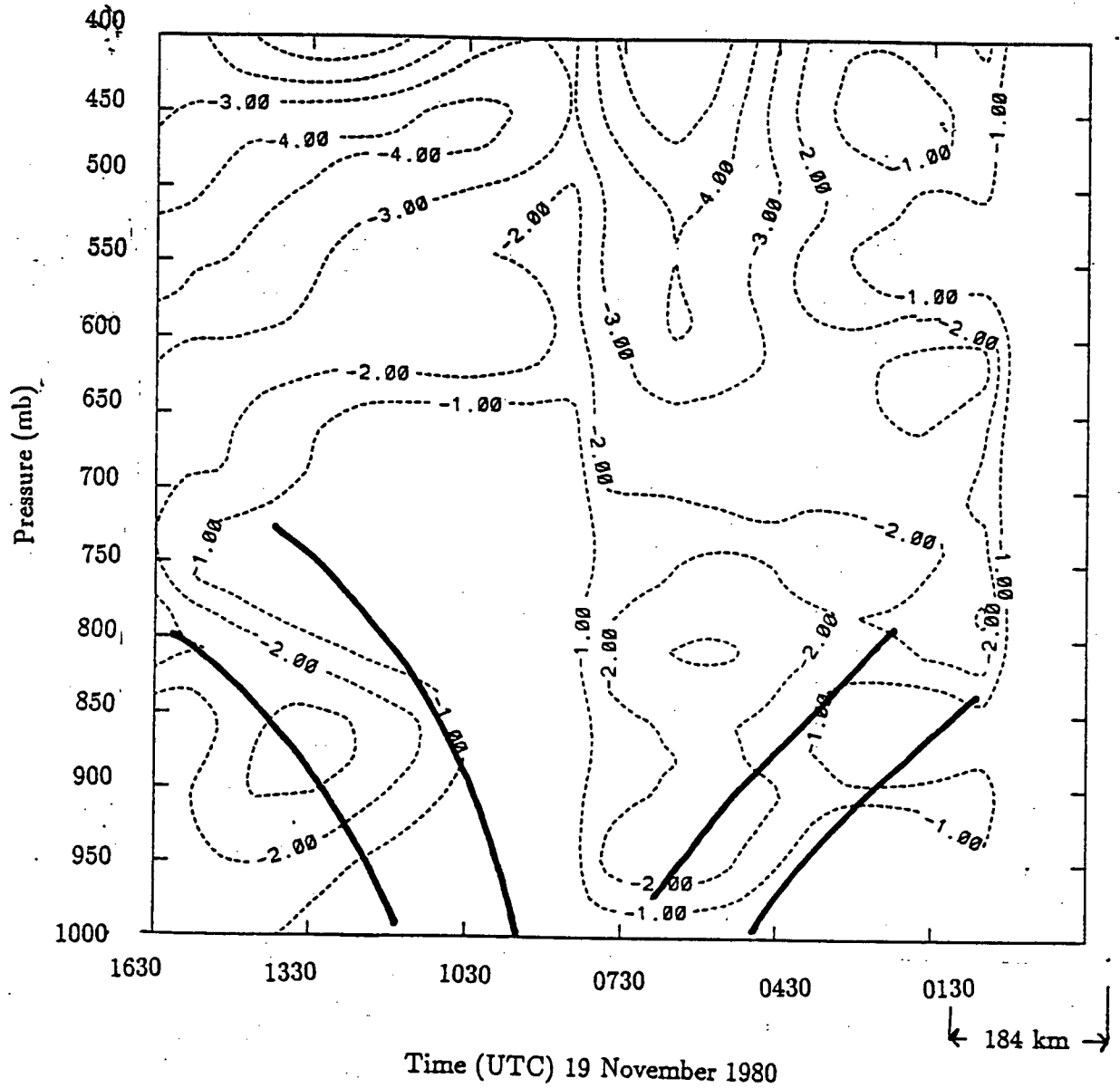


Figure 3.14: Time-Pressure cross section of  $\frac{\partial \theta_e}{\partial y}$ . Dashed lines indicate negative values (Units  $10^{-5} \text{ } ^\circ\text{K m}^{-1}$ ).

## Chapter 4

### Kinematic Structure

#### 4.1 Horizontal Winds

The wind components were calculated according to the coordinate system previously discussed such that the x-axis is aligned parallel to the direction of system motion and the y-axis is in the along frontal direction. Further, the origin is moving with the system so that the cross sections show the relative u wind (cross-frontal, positive to the east in this co-ordinate system) after subtracting the speed of the system ( $17 \text{ m s}^{-1}$ ). The wind gradients were calculated as described in the previous chapter. The uncertainty in the horizontal winds of  $3 \text{ m s}^{-1}$  (McBean and Phillips, 1986) combines with the errors in the distance between soundings to produce an uncertainty in the cross-frontal gradients of the wind components of  $0.2 \times 10^{-4} \text{ s}^{-1}$ . The error in the along front distance between the two ships soundings also leads to an uncertainty in the  $y$  gradients of the horizontal winds of  $0.2 \times 10^{-4} \text{ s}^{-1}$ . The 10% error in the spacing between vertical grid points accounts for the uncertainty in the vertical derivatives of  $u$  and  $v$  of  $0.6 \times 10^{-5} \text{ m s}^{-1} \text{ mb}^{-1}$ . As in the previous chapter, all fields of derivatives are plotted such that only contours greater than the probable errors are shown.

The  $u$  wind component in both cross-sections (figures 4.1 and 4.3) is easterly everywhere throughout the section in the lowest layers in a similar manner to Hobbs et al. (1975). The flow is moderately negative (easterly) at the surface ahead of the warm front ( $\sim -7 \text{ m s}^{-1}$ ). An outflow to the west behind the cold front of similar intensity is evident

in both sections, however this region of easterly winds is deeper (up to  $\sim 800\text{ mb}$ ) than in the pre-warm frontal region. Westerly winds ( $u$  positive) predominate in the upper regions of both cross-sections with values near  $14\text{ m s}^{-1}$  at  $500\text{ mb}$ . In summary, there is a strong inflow to the system from the east at the lower levels (similar to those shown by Carbone, 1982, Hobbs and Persson, 1982, Bond and Fleagle, 1985, and McBean and Stewart, 1991) and a generally westerly flow aloft.

The along-frontal wind components (figures 4.2 and 4.4) are also very similar at both locations. The north-south wind is generally positive (southerly) except for a region of weak northerly winds ( $-5\text{ m s}^{-1}$  at the Vancouver and  $-1\text{ m s}^{-1}$  at the Oceanographer) below  $800\text{ mb}$  behind the cold front. Ahead of the surface warm front there is a strong ( $19\text{ m s}^{-1}$  for the Vancouver and  $27\text{ m s}^{-1}$  at the Oceanographer) jet below  $900\text{ mb}$ . As will be discussed later, this jet corresponds to the so-called cold conveyor belt. Directly above at  $550\text{ mb}$  the Vancouver shows a second jet of  $21\text{ m s}^{-1}$ . While the Oceanographer's section does not exhibit this second region of peak southerly winds they still remain strong ( $\geq 12\text{ m s}^{-1}$ ) up to  $550\text{ mb}$ . Low level jets in the along front wind component ahead of the surface cold front have been found by others (Browning and Pardoe, 1972, Hobbs and Persson, 1982, McBean and Stewart, 1991), however Krietzberg (1968) represents the only well documented case of a pre-warm frontal low level jet similar to that of this storm.

The largest gradient of  $\partial u/\partial x$  (figure 4.5) for the ship Vancouver occurred in the cold frontal zone away from the surface, with the maximum value of  $0.35 \times 10^{-4}\text{ s}^{-1}$  at  $750\text{ mb}$ . Small negative values ( $-0.1 \times 10^{-4}\text{ s}^{-1}$ ) of this gradient appeared in the warm frontal transition zone. The same field is shown for the Oceanographer in figure 4.6. Even less of the section exhibited values greater than the uncertainty for this section than for the Vancouver. The largest gradient was convergence in the lower warm frontal zone of  $0.35 \times 10^{-4}\text{ s}^{-1}$ . As with the Vancouver, the mid cold frontal zone did exhibit

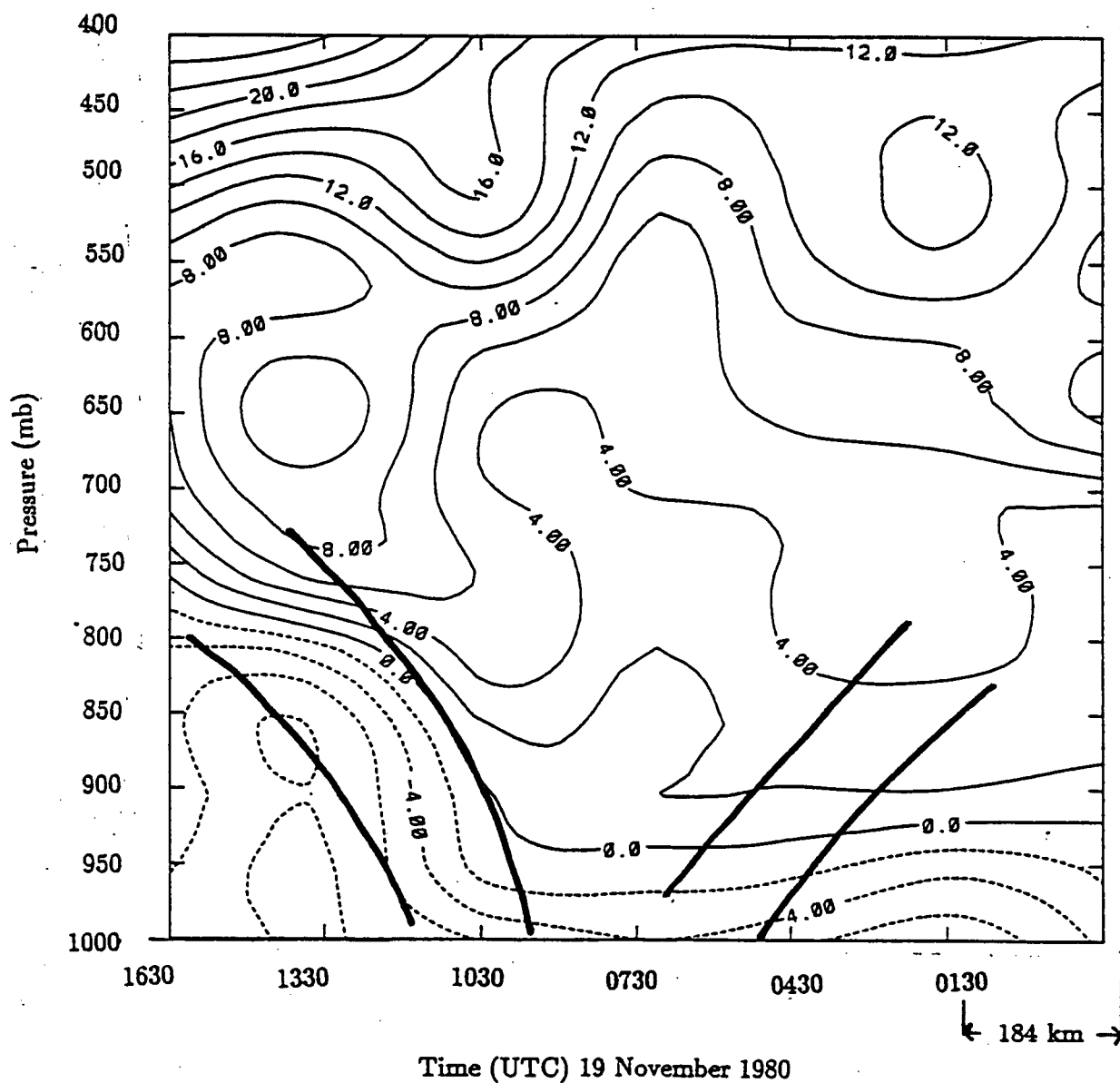


Figure 4.1: Time-Pressure cross section of u wind component at the ship Vancouver as defined in text (contour interval  $2 m s^{-1}$ ).

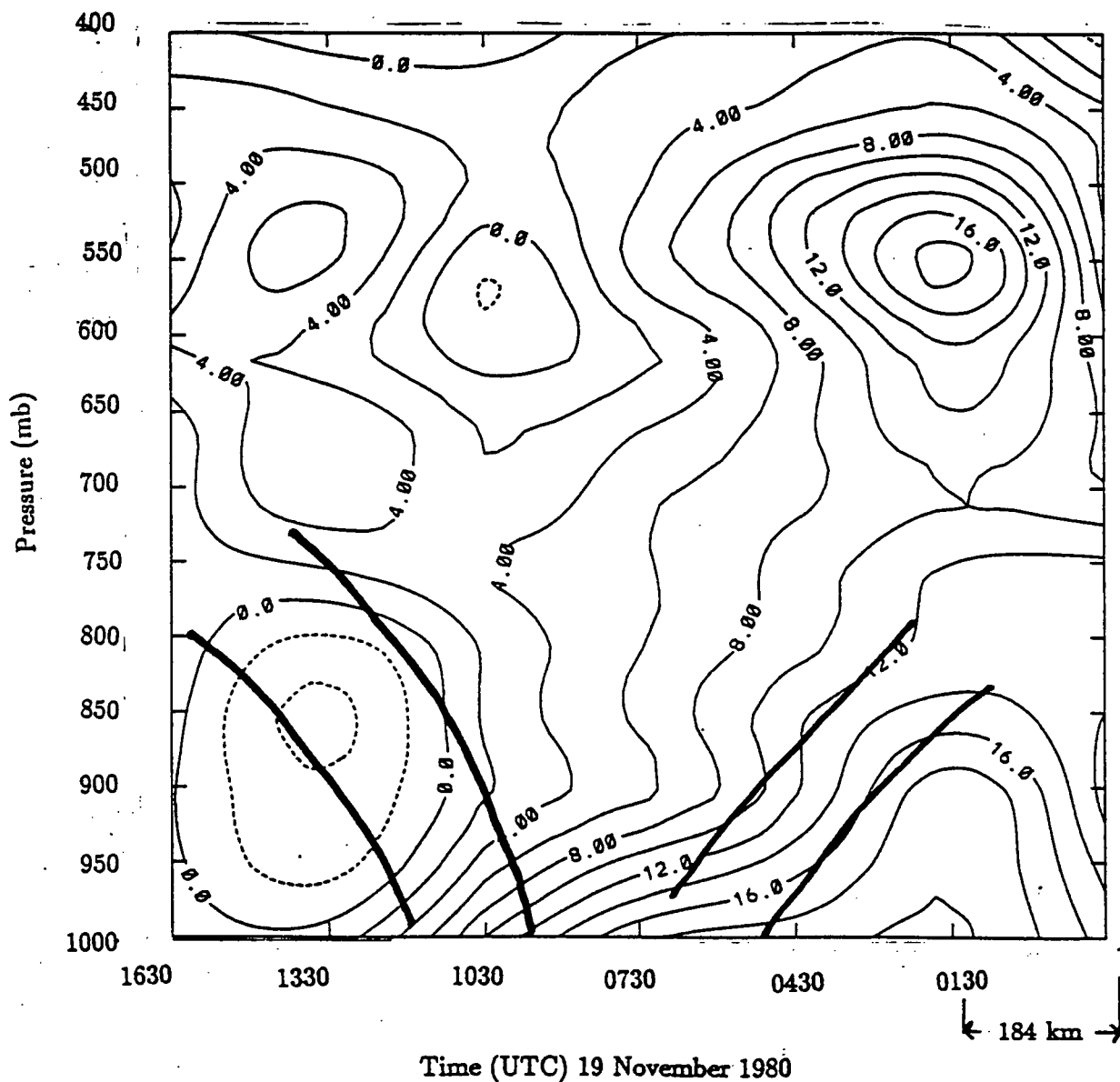


Figure 4.2: Time-Pressure cross section of v wind component at the ship Vancouver as defined in text (contour interval  $2 ms^{-1}$ ).

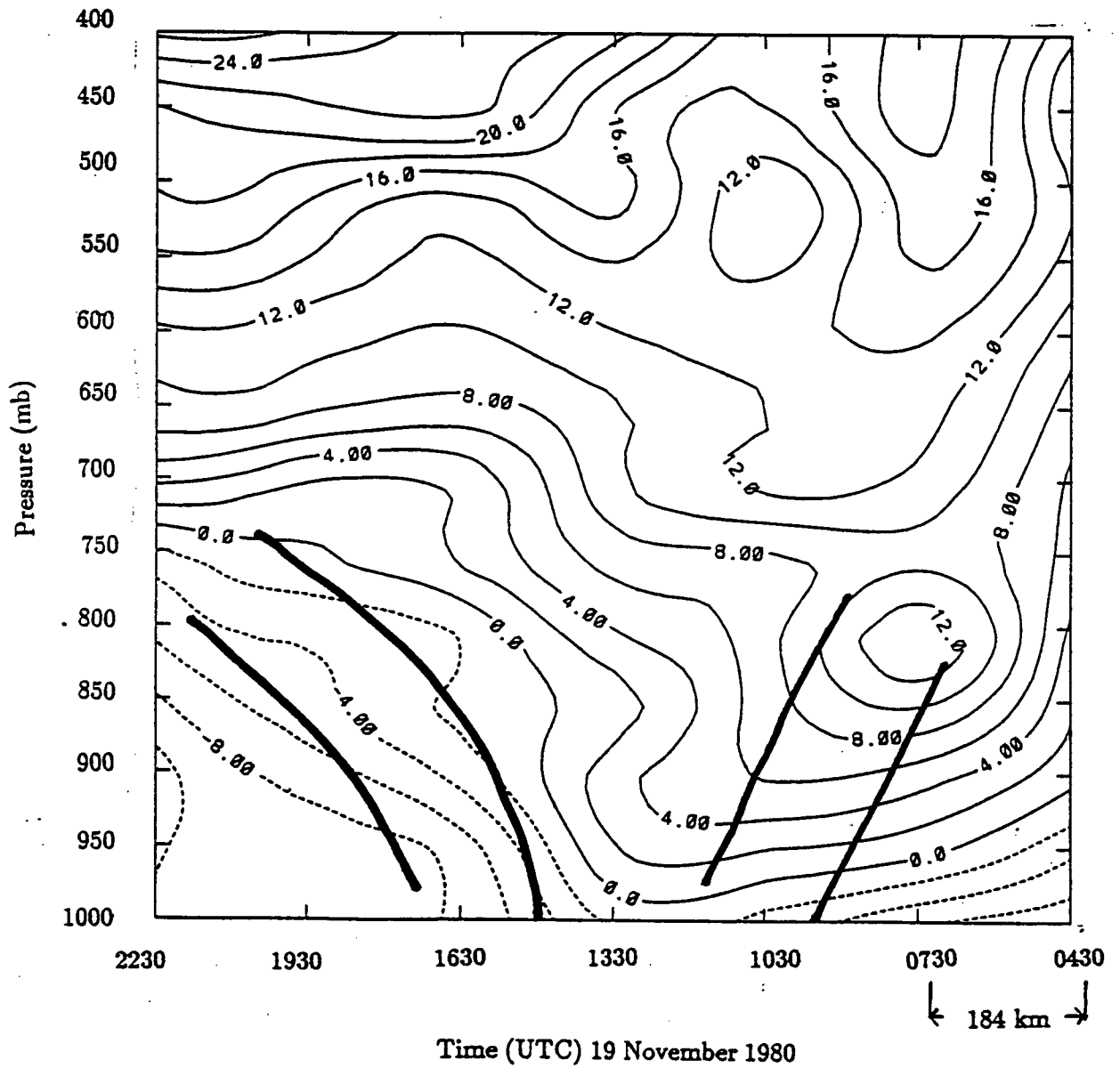


Figure 4.3: Time-Pressure cross section of u wind component at the ship Oceanographer as defined in text (contour interval  $2\text{ms}^{-1}$ ).

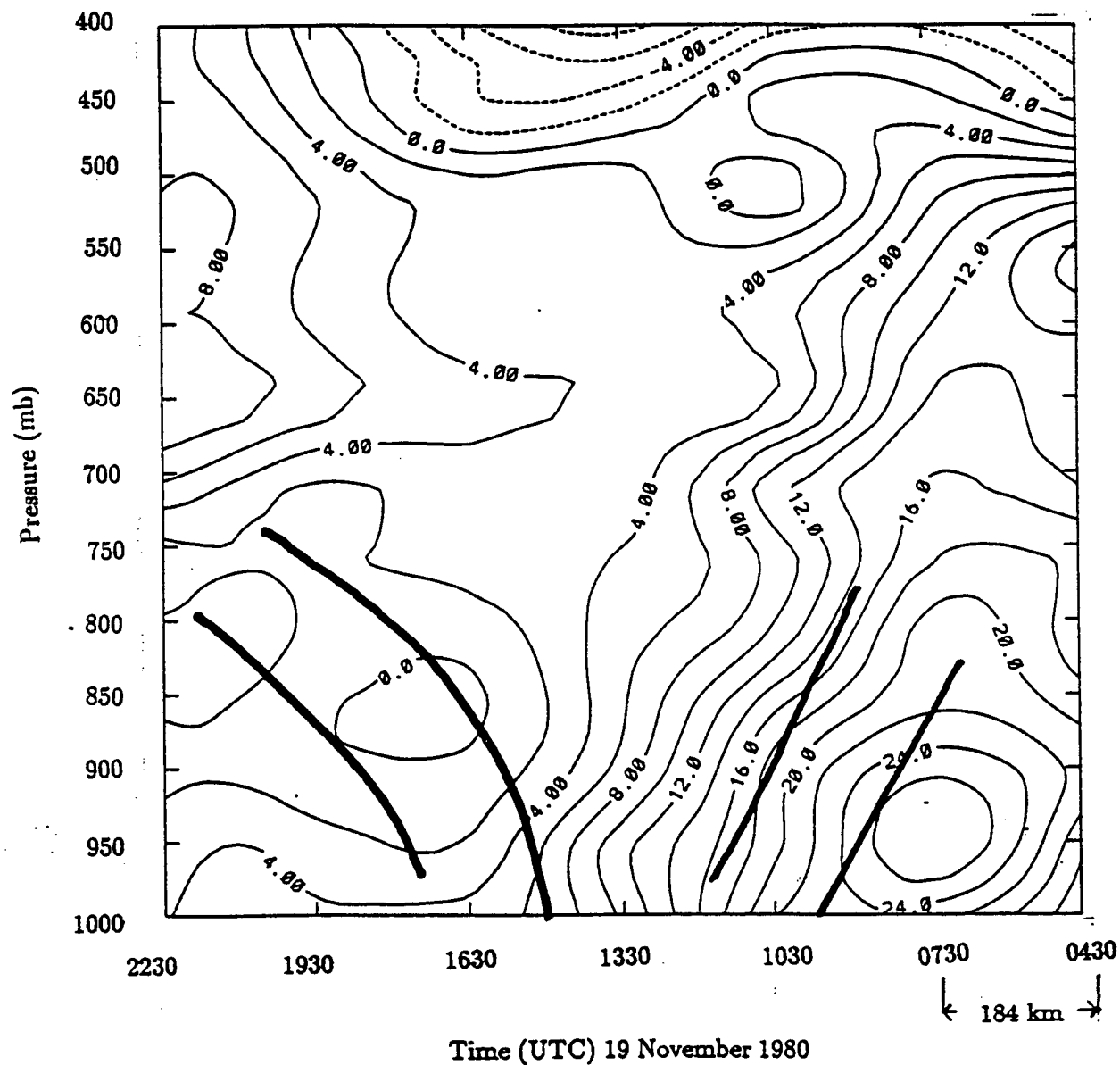


Figure 4.4: Time-Pressure cross section of v wind component at the ship Oceanographer as defined in text (contour interval  $2 \text{ms}^{-1}$ ).

some divergence, albeit of lesser magnitude with a peak of  $0.25 \times 10^{-4} \text{ s}^{-1}$ .

The  $\partial v/\partial y$  field is shown in figure 4.7. The warm frontal zone is a region of relatively strong convergence in the along front wind ( $-0.65 \times 10^{-4} \text{ s}^{-1}$  at 900 and 825 *mb*), which is stronger than the convergence in the cross-frontal wind at either ship in this region. The near surface area of the cold frontal zone experiences divergence in  $\partial v/\partial y$  of  $0.2 \times 10^{-4} \text{ s}^{-1}$ .

The horizontal wind divergence,  $\partial u/\partial x + \partial v/\partial y$ , as calculated at the Vancouver is shown in figure 4.8. The warm frontal zone, dominated by  $\partial v/\partial y$ , is a region of strong convergence with the peak magnitude of  $-0.9 \times 10^{-4} \text{ s}^{-1}$  at 900 *mb*. The cold frontal zone, primarily influenced by  $\partial u/\partial x$ , is a region of smaller, yet still significant, divergence. There is a broad region of  $\sim 0.3 \times 10^{-4} \text{ s}^{-1}$  from 950 to 800 *mb* and a smaller region at 750 *mb* in the upper cold front with divergence of  $0.45 \times 10^{-4} \text{ s}^{-1}$ . The general pattern of divergence in the cold frontal zone which is observed at both ships is significantly different from most other studies (see Bond and Fleagle, 1985; McBean and Stewart, 1991; Rao, 1966; Baldwin et al., 1984; Ogura and Portis, 1982) which exhibit convergence in the region of the surface cold front.

The pattern of horizontal wind shear,  $\partial v/\partial x$ , for each ship is shown in figures 4.9 and 4.10 respectively. For the Vancouver (figure 4.9) it is similar to  $\partial u/\partial x$  in that the peak values  $0.75 \times 10^{-4} \text{ s}^{-1}$  are in the cold frontal zone although in this case they extend from the surface up to 800 *mb*. A secondary peak of  $0.45 \times 10^{-4} \text{ s}^{-1}$  also exists at 900 *mb* in the warm frontal zone. The pattern of wind shear at the Oceanographer (figure 4.10) shows some different features. The warm frontal zone exhibits high values of wind shear, although the maximum gradient,  $0.75 \times 10^{-4} \text{ s}^{-1}$ , occurs slightly to the west of the trailing edge of the warm frontal zone. In a similar fashion to other parameters in the cold frontal zone at the Oceanographer, the wind shear is small, indicating that this is region does not exhibit strong frontal characteristics.  $\partial u/\partial y$  (figure 4.11) shows two main regions of large magnitudes. In the upper cold frontal zone the value is  $0.4 \times 10^{-4} \text{ s}^{-1}$ . At 800 *mb*

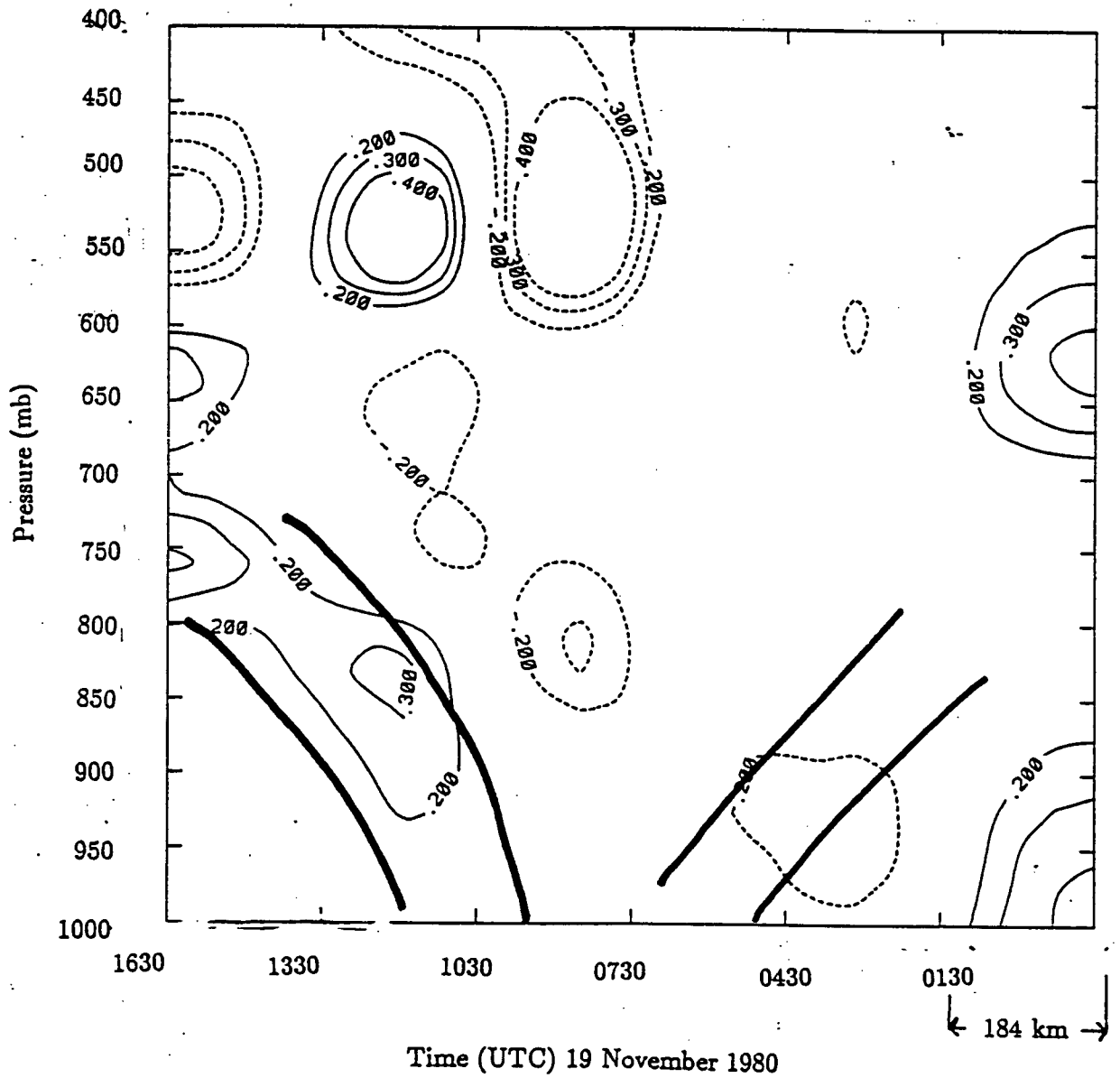


Figure 4.5: Time-Pressure cross section of  $\frac{\partial u}{\partial z}$  for the ship Vancouver. Dashed lines indicate negative values (Units  $10^{-4} s^{-1}$ ).

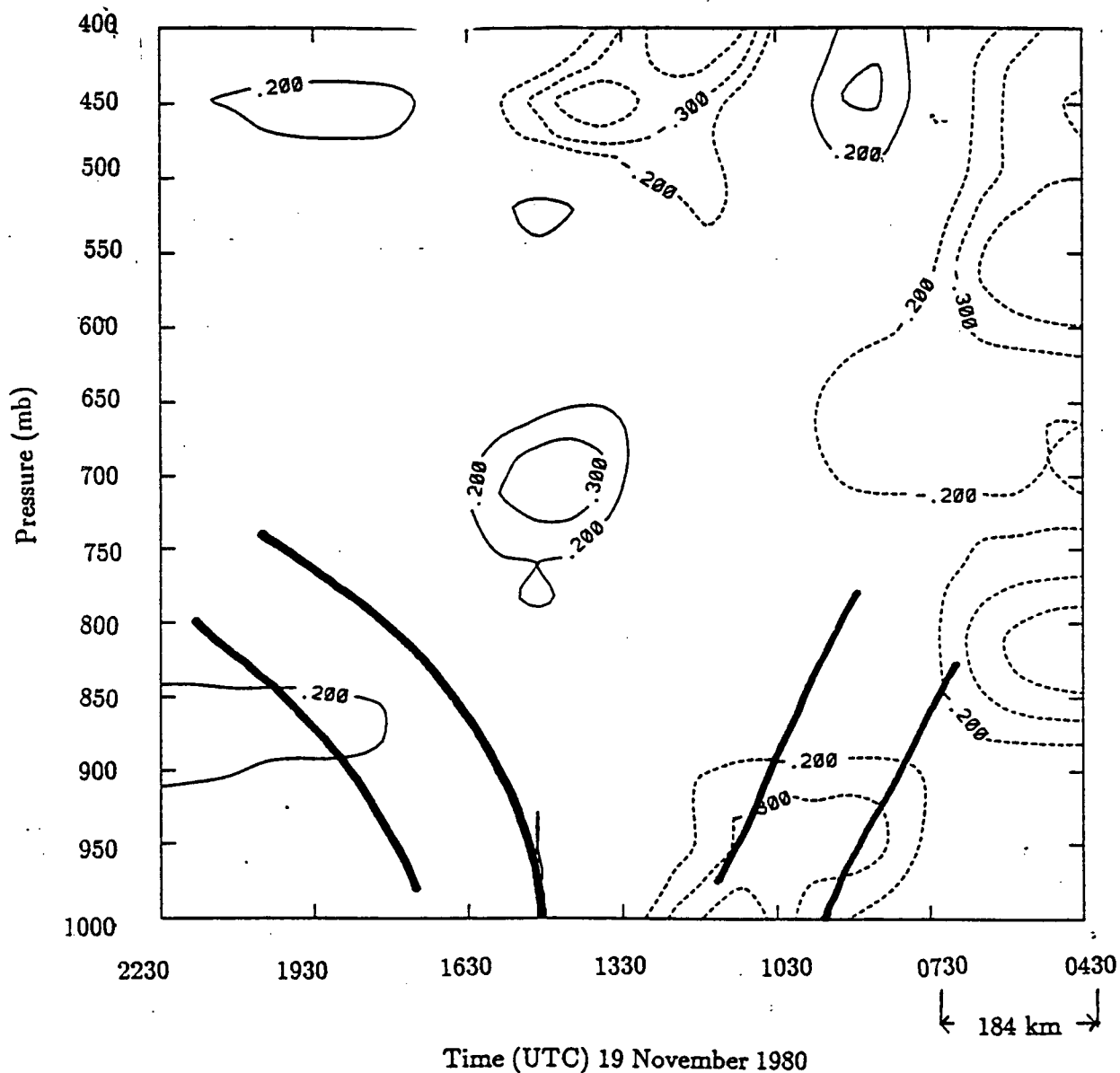


Figure 4.6: Time-Pressure cross section of  $\frac{\partial u}{\partial x}$  for the ship Oceanographer. Dashed lines indicate negative values (Units  $10^{-4} s^{-1}$ ).

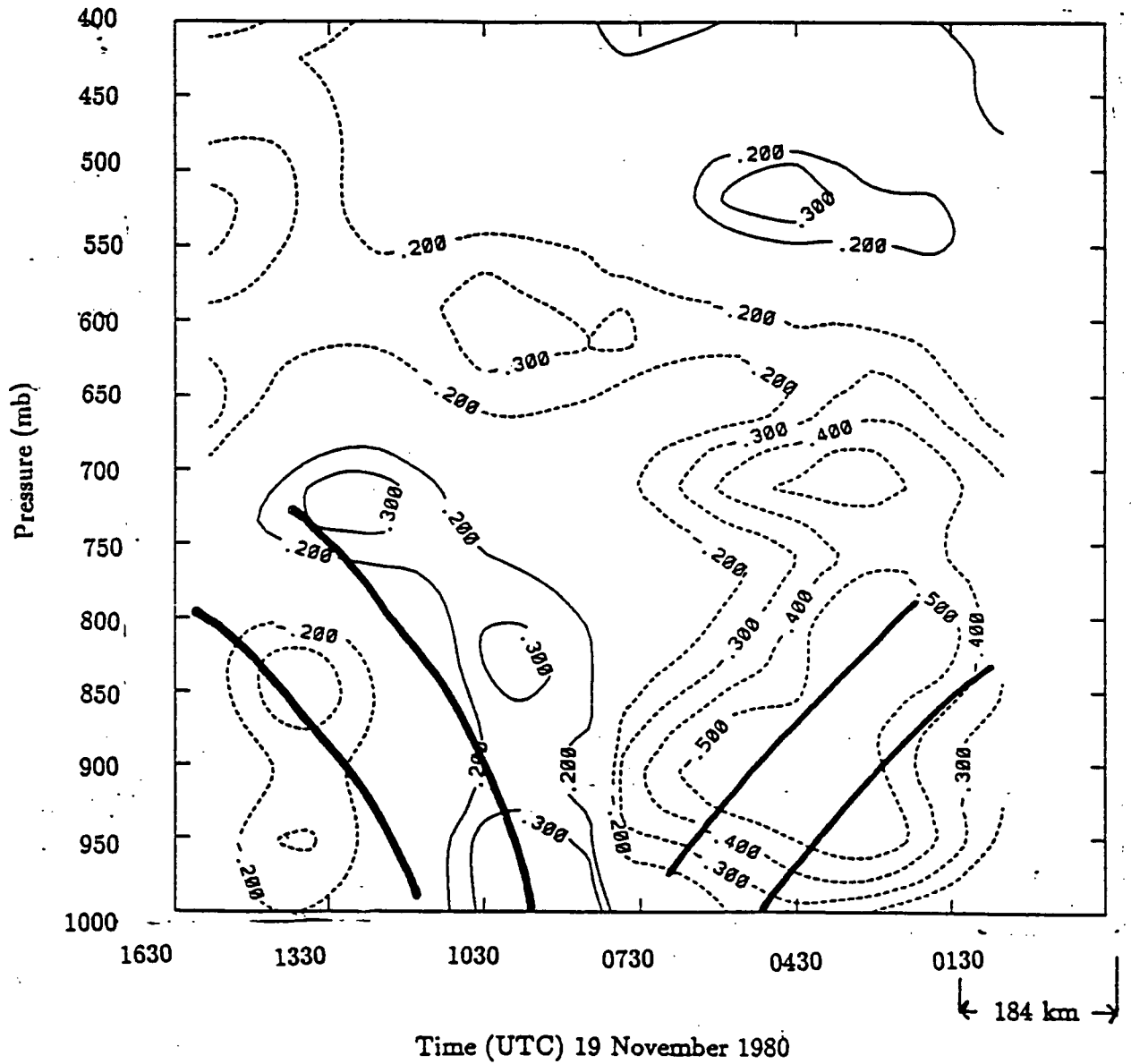


Figure 4.7: Time-Pressure cross section of  $\frac{\partial v}{\partial y}$ . Dashed lines indicate negative values (Units  $10^{-4} s^{-1}$ ). Contours greater than  $\pm 0.5 \times 10^{-4} s^{-1}$  not included.

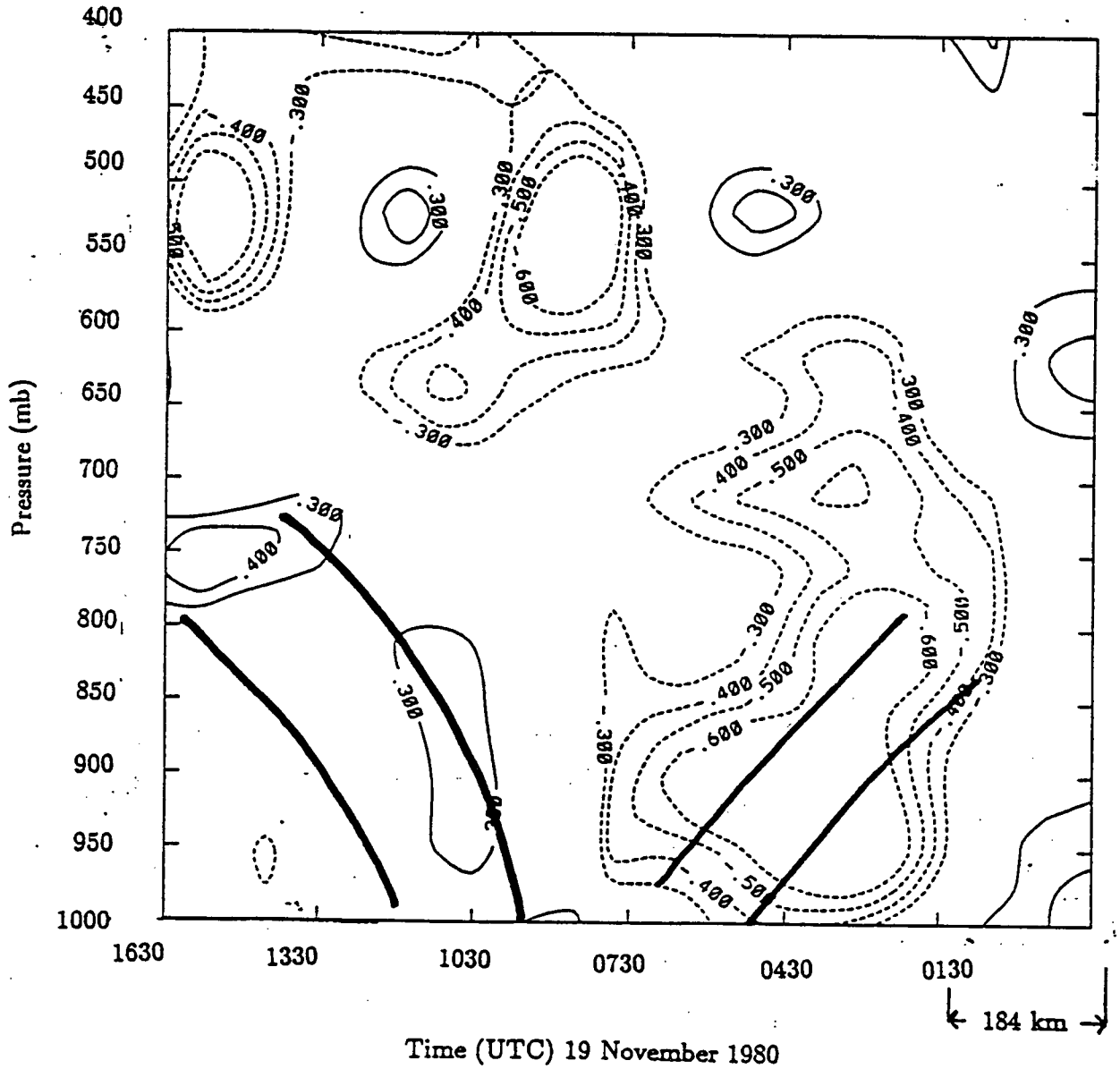


Figure 4.8: Time-Pressure cross section of horizontal divergence,  $\frac{\partial u}{\partial x} + \frac{\partial v}{\partial y}$ . Dashed lines indicate negative values (Units  $10^{-4} s^{-1}$ ). Contours greater than  $\pm 0.6 \times 10^{-4} s^{-1}$  not included.

just to the west of the warm frontal zone is a region of peak negative  $\partial u/\partial y$  with the maximum at  $-0.9 \times 10^{-4} \text{ s}^{-1}$ . We would normally expect the maximum gradient to occur in the frontal zone (since they are defined as regions of strong gradients) but notice that it is slightly offset to the west which may be a result of the technique of aligning the fronts for the calculation of the y derivatives.

The vertical component of relative vorticity,  $\partial v/\partial x - \partial u/\partial y$ , (figure 4.12) also shows a pattern with two regions of peak magnitude. There is an axis of high vorticity coincident with the cold frontal zone extending from the surface up to near 800 mb with a peak of  $0.7 \times 10^{-4} \text{ s}^{-1}$ . These values in the cold frontal transition zone are dominated by the term  $\partial v/\partial x$ . Axes of relative vorticity have been used by others to define fronts (see Bond and Fleagle, 1985) and although in this case the frontal zone has been defined based on the thermodynamic structure it corresponds closely with the line of maximum relative vorticity. The pattern and magnitude of the vorticity in the region of the cold front are very similar to those shown by Ogura and Portis (1982) in their study of a cold front over the south-central United States. Bond and Fleagle (1985) and McBean and Stewart (1991) have shown similar patterns of maximum cyclonic vorticity in the region of the frontal zone however magnitudes of the peaks in these studies are higher than in the present case. On the western edge of the warm frontal zone, at 875 mb, lies the other region of strong cyclonic vorticity ( $0.95 \times 10^{-4} \text{ s}^{-1}$ ). Since this feature is dominated by  $\partial u/\partial y$  as discussed above, it is possible that the location is slightly misplaced and that the maximum should be centred in the warm frontal zone. While strong cyclonic vorticity has not been observed in warm frontal zones of other studies, it is a characteristic that is generally associated with frontal zones and therefore this observation should not be surprising.

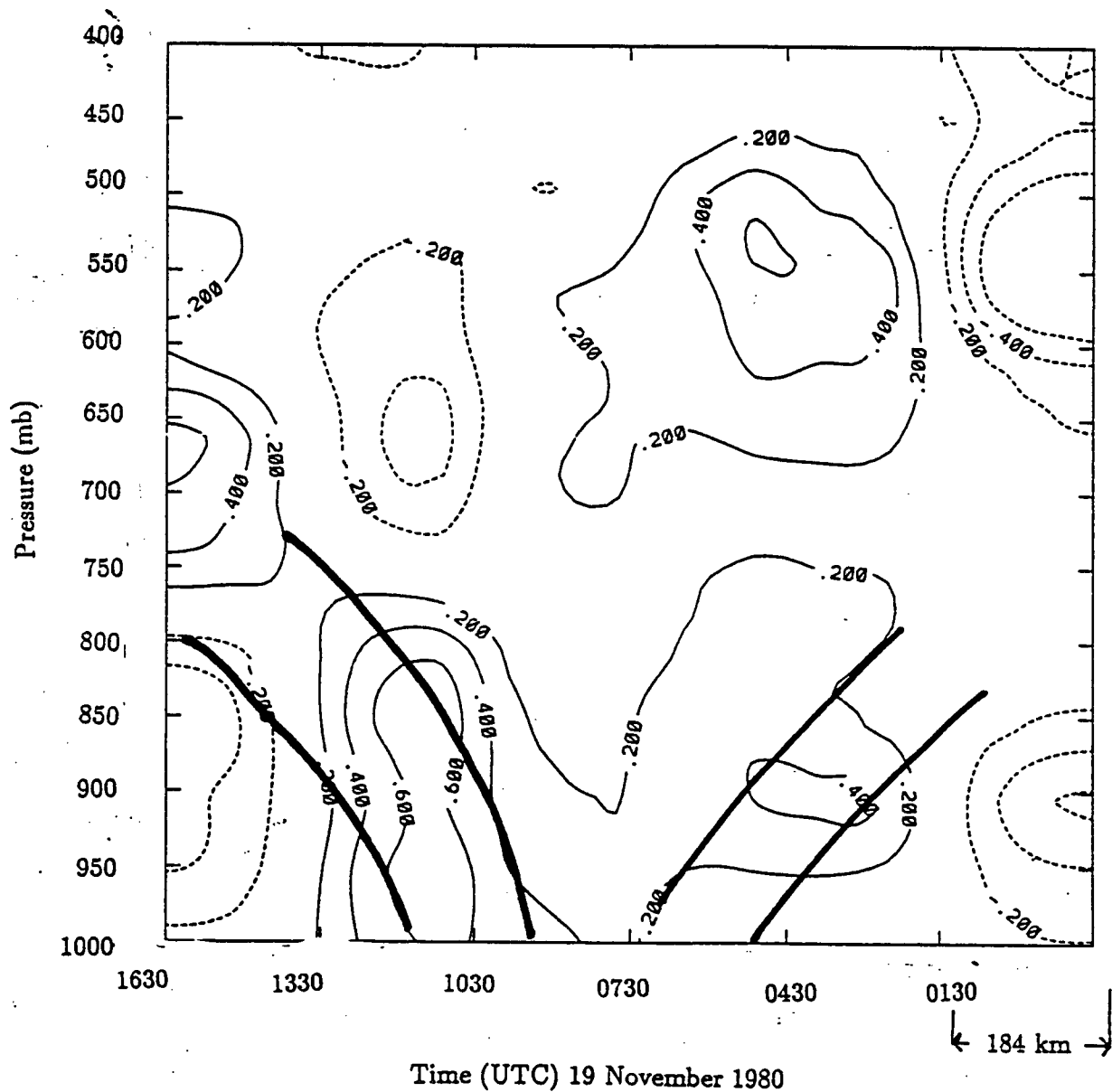


Figure 4.9: Time-Pressure cross section of  $\frac{\partial v}{\partial x}$  for the ship Vancouver. Dashed lines indicate negative values (Units  $10^{-4} s^{-1}$ ).

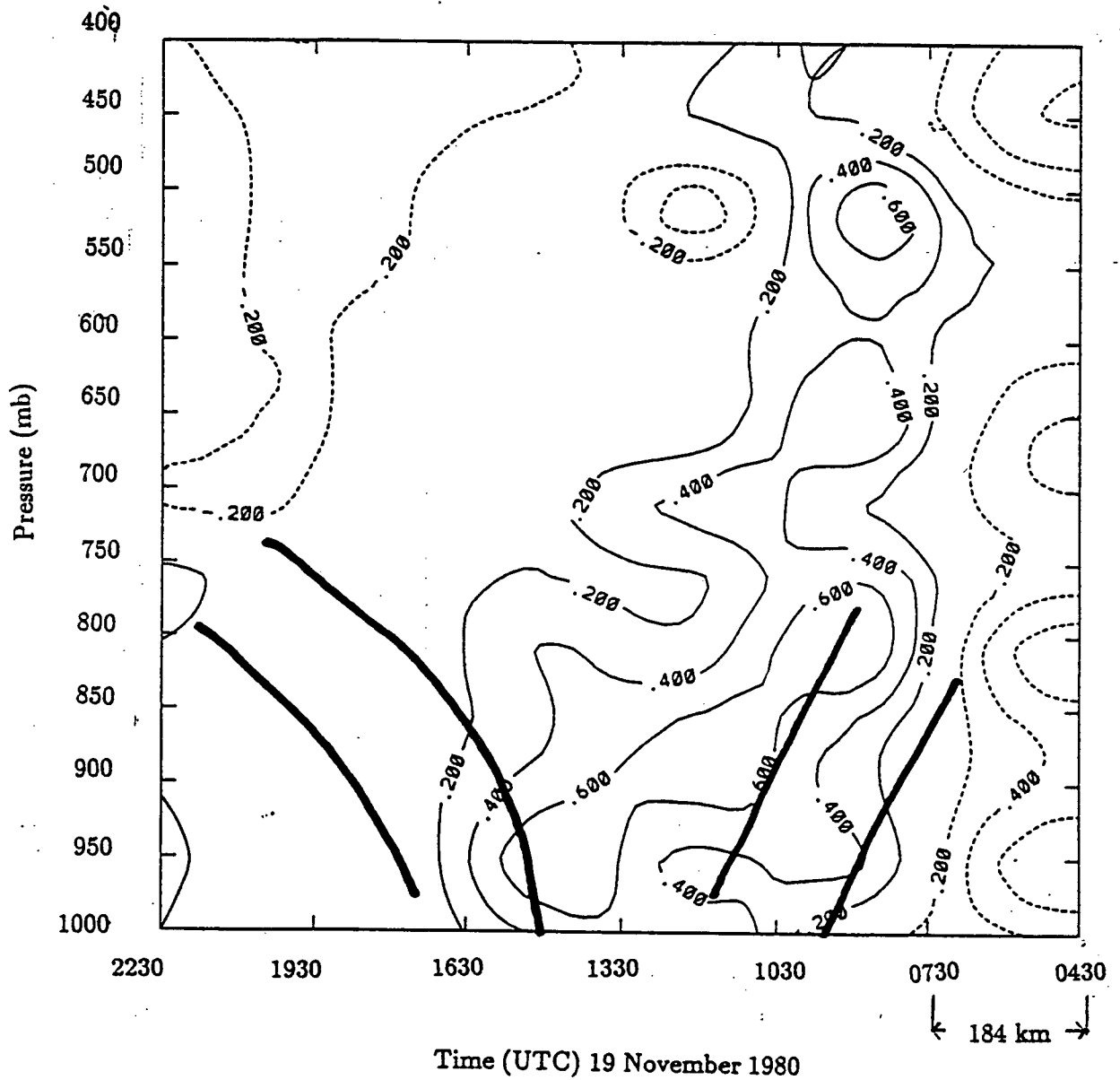


Figure 4.10: Time-Pressure cross section of  $\frac{\partial v}{\partial x}$  for the ship Oceanographer. Dashed lines indicate negative values (Units  $10^{-4} s^{-1}$ ).

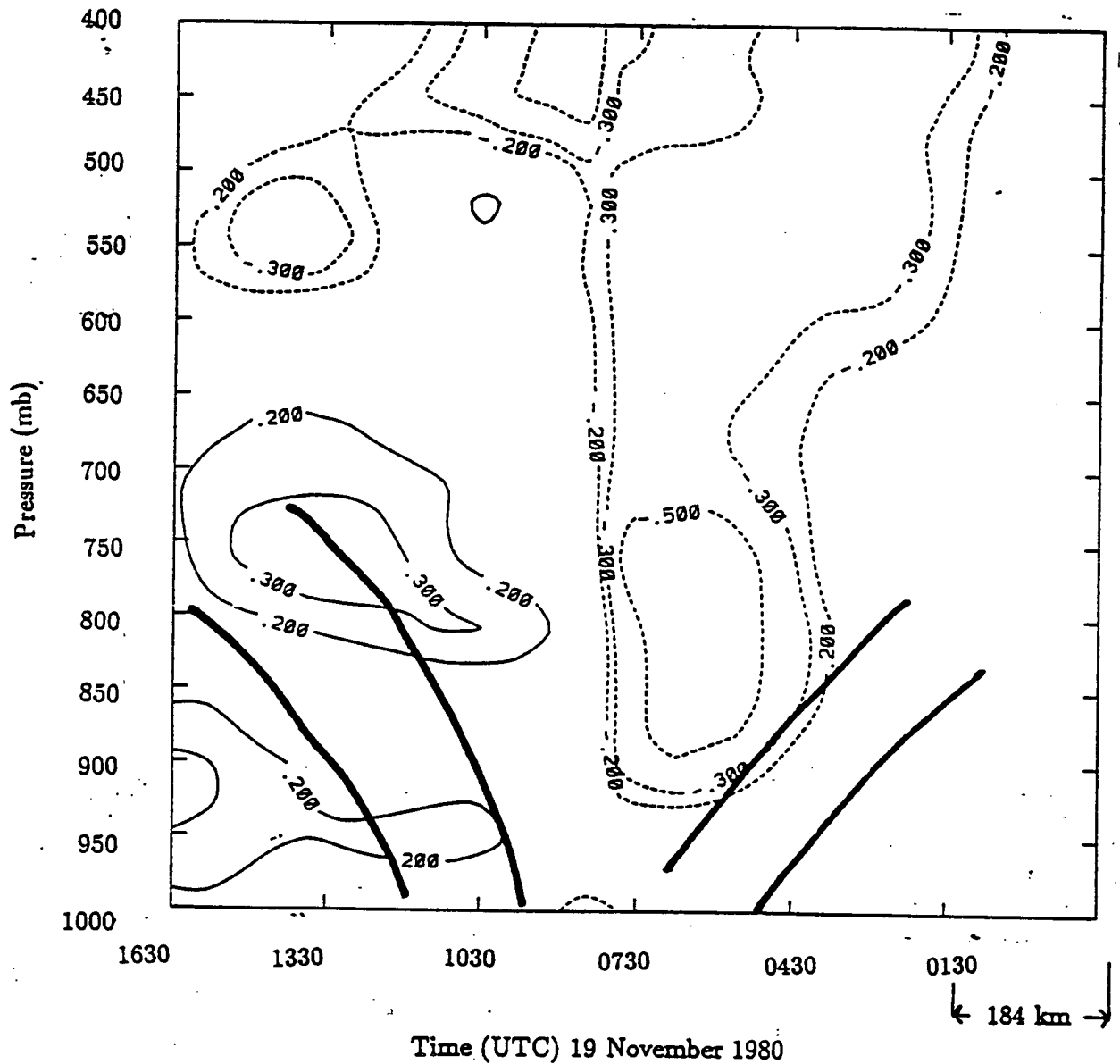


Figure 4.11: Time-Pressure cross section of  $\frac{\partial u}{\partial y}$ . Dashed lines indicate negative values (Units  $10^{-4} s^{-1}$ ). Contours greater than  $\pm 0.5 \times 10^{-4} s^{-1}$  not included.

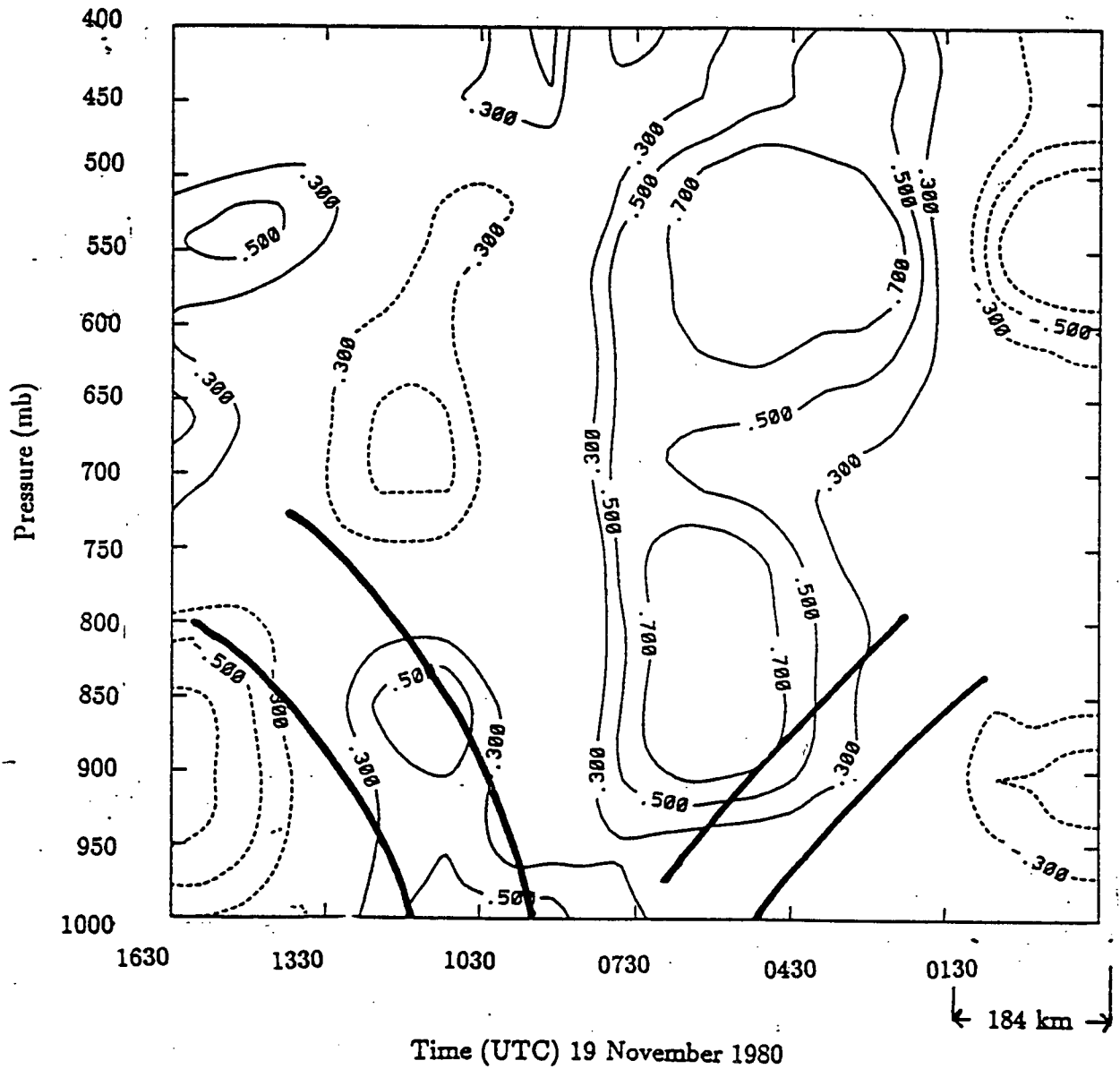


Figure 4.12: Time-Pressure cross section of vertical component of relative vorticity  $\frac{\partial v}{\partial x} - \frac{\partial u}{\partial y}$ . Dashed lines indicate negative values (Units  $10^{-4} s^{-1}$ ). Contours greater than  $\pm 0.5 \times 10^{-4} s^{-1}$  not included.

## 4.2 Vertical Velocity

The vertical velocity ( $\omega$ ) field was calculated using the kinematic method. This technique is based on the isobaric continuity equation,

$$\left(\frac{\partial u}{\partial x} + \frac{\partial v}{\partial y}\right)_p + \frac{\partial \omega}{\partial p} = 0.$$

After integrating the form is

$$\omega(p) = \omega(p_0) + (\Delta p) \left[ \frac{\partial \langle u \rangle}{\partial x} + \frac{\partial \langle v \rangle}{\partial y} \right]_p,$$

where  $\langle ( ) \rangle = \frac{1}{p-p_0} \int_{p_0}^p ( ) dp$  is a pressure weighted vertical average and  $p_0$  is the reference surface pressure. The boundary condition of  $\omega = 0$  at  $p = p_0$  was included in the calculations. The kinematic method is popular because the only assumption it requires is that of an atmosphere in hydrostatic balance and it does not require time derivatives or density in order to calculate the vertical velocity. The problem with this method lies in the difficulty in accurately measuring the horizontal winds. Small errors in the measurement of the horizontal winds can easily lead to large errors in the vertical velocity. Furthermore, the errors are summed with height through the integral.

Using estimates of the uncertainties in horizontal wind speed and horizontal distance between soundings as previously discussed, contours of vertical velocity greater than the uncertainty were plotted as the significant vertical velocity (figure 4.13). We see that the main area of ascent ( $\omega < 0$ ) is in the region of the warm front and the main area of descending motion is associated with the cold front. This follows from the previously discussed divergence in the cold frontal region and convergence in the warm frontal transition zone. The maximum descent is  $0.09 Pa s^{-1}$  in the upper regions of the cold front and the maximum ascent is  $-0.06 Pa s^{-1}$  in the higher regions of the warm frontal zone. The descent along the cold front is in sharp contrast to most other studies which

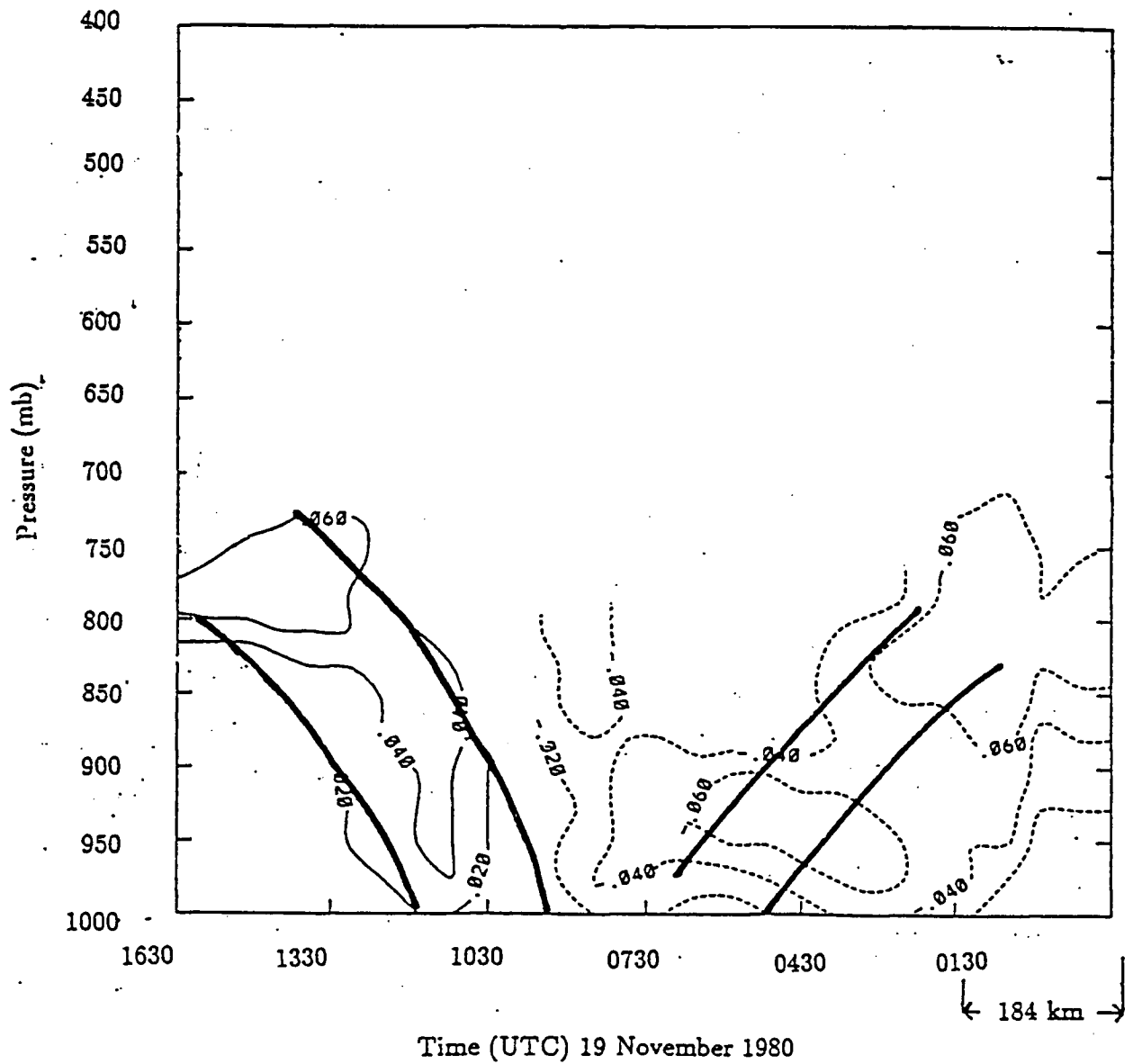


Figure 4.13: Time-Pressure cross section of significant vertical velocity at the ship Vancouver as calculated kinematically. Dashed lines indicate negative values (upward motion) (Units  $Pa s^{-1}$ ). Contours end in the figure since the uncertainties increase with height. Contours greater than  $\pm 0.06 Pa s^{-1}$  not included.

find ascent in the lower cold frontal regions. Bond and Fleagle (1985) found a peak of  $-1.0 Pa s^{-1}$ , Ogura and Portis (1982) found a maximum of  $-0.6 Pa s^{-1}$ , and McBean and Stewart (1991) calculated the peak ascent to be  $-0.4 Pa s^{-1}$ . The downward motion in the cold frontal zone, compared with the upwelling in this region found by most other authors (see for example Bond and Fleagle (1985), Ogura and Portis (1982), and McBean and Stewart (1991)), results directly from the observed horizontal divergence in this region calculated previously.

### 4.3 Air Streams

This section uses relative isentropic analysis (see Carlson; 1980, Donaldson and Stewart, 1989) to determine the air motion relative to the moving system. If we assume that all motions are adiabatic, then the potential temperature,  $\theta$ , is a conserved quantity for dry processes. Furthermore, the equivalent potential temperature,  $\theta_e$ , is conserved for both dry and moist processes so the air parcels will move on surfaces of constant  $\theta_e$ .

#### 4.3.1 Warm Conveyor Belt

Figure 4.14 shows the pressure (height) of the  $30^\circ C$   $\theta_e$  surface and vectors based on the analysed wind field at the northern and southern extremes of the surface. The trough in this surface lies just above the warm and cold fronts at the northern end of the section. The vectors (determined from figures 4.1 to 4.4) show that the air in this warm core is moving strongly towards the north at the Oceanographer ( $\sim 14 m s^{-1}$ ) and more moderately so at the Vancouver ( $\sim 5 m s^{-1}$ ). The  $0 m s^{-1}$  east-west wind contour at the Oceanographer corresponds closely with this surface and at the Vancouver there is a  $\sim 3 m s^{-1}$  westerly component to the total wind vector. At the southern end of the surface, the eastern boundary of the isentropic surface corresponds roughly with the warm

side boundary of the warm frontal transition zone. This isentropic surface also rises from the south (where it is below 950 *mb*) to the north (where it is near 800 *mb*). An air parcel moving along the trough of this surface from the south to the north would undergo an ascent rate on the order of  $0.1 \text{ Pas}^{-1}$  which is slightly larger than the maximum kinematically calculated vertical velocity in this region. There is also vertical motion occurring along the steep sides of the trough. The eastern slope appears to be an anasurface with rising motion above the warm front while the western kata-edge is the location of downward vertical motion in agreement with the previously calculated vertical velocity. This trough of this surface appears to match very closely the warm conveyor belt described by Carlson (1980) and Stewart and Macpherson (1989). Due to the limited domain of data values one can not verify with measurements their anticyclonic curvature of this stream as it extends north of the surface low, however, the feathering out of the upper clouds to the north-east of the low as shown by the satellite images suggests that the WCB does indeed behave in the manner as suggested by the previous authors. The precipitation occurring just ahead of the surface warm front is associated with the leading edge of this warm core of air.

### 4.3.2 Cold Airstreams

Figure 4.14 also shows two isentropic surfaces at  $22^\circ\text{C}$ , one to the east of the warm front and the other to the west of the cold front. The eastern surface corresponds very closely to the maximum southerly easterly jet as shown in figure 4.2. The *u* component of the horizontal wind on this surface is near 0 at both ships. This stream is referred to as the cold conveyor belt by Carlson (1980) and others. The moist cold conveyor belt flows below the warm conveyor and accounts for the eastern extent of the low cloud as shown previously. The surface is nearly level from its southern to its northern extent and therefore the air does not experience strong vertical velocities. We have no data

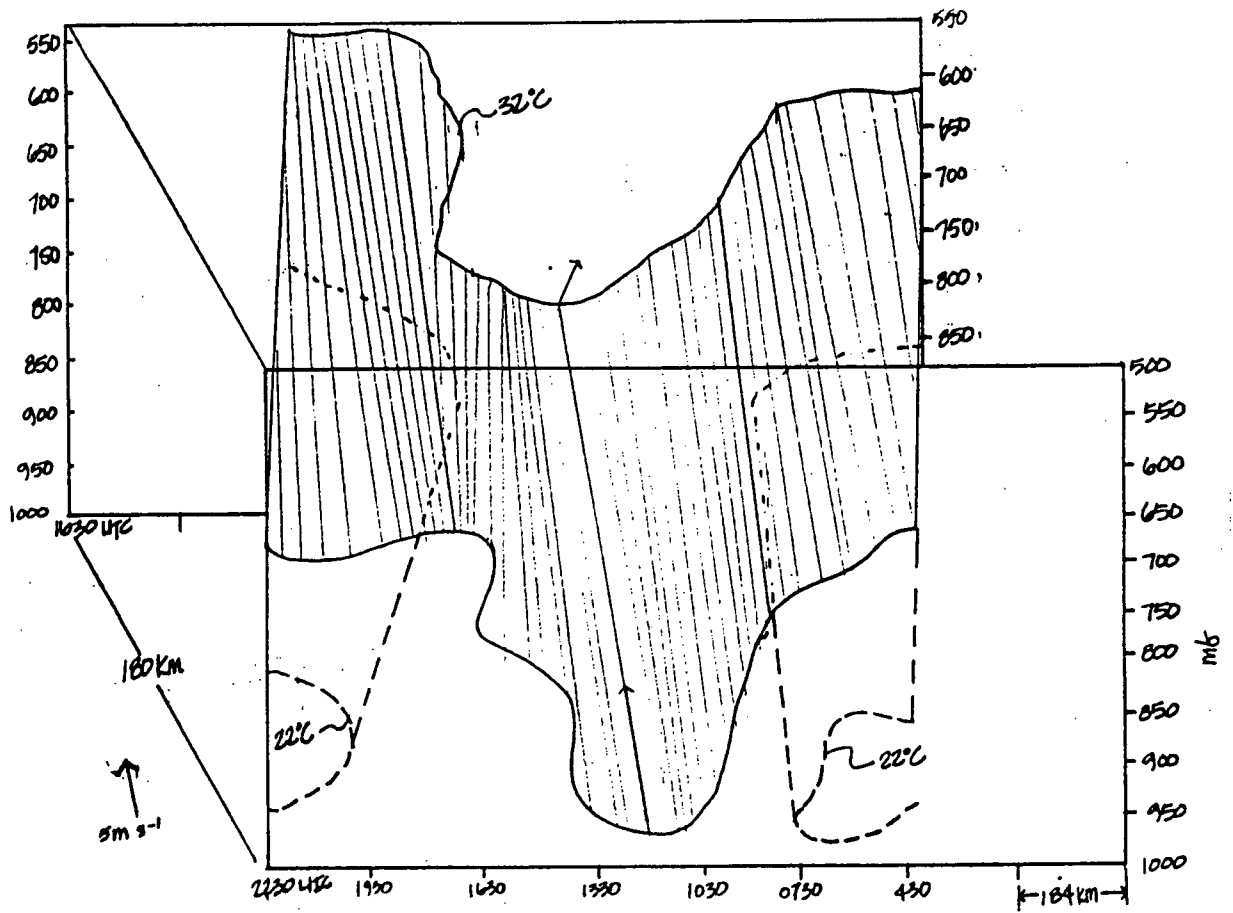


Figure 4.14: Pressure of constant  $30^\circ\text{C}$   $\theta_e$  and  $22^\circ\text{C}$   $\theta_e$  surfaces. Vectors indicate wind components on the surface at each ship.

to suggest whether the cold conveyor belt, after passing the junction of the warm and cold fronts, turns anticyclonically as in Carlson (1980) and Browning and Monk (1981) or cyclonically as in Stewart and Macpherson (1989).

A second cold airstream is suggested by the western cold isentropic surface. This jet, which flows near the surface moving to the south at around  $5 \text{ m s}^{-1}$  at the Vancouver and  $\sim 1 \text{ m s}^{-1}$  at the Oceanographer and to the west (around  $6 \text{ m s}^{-1}$ ) at both ships does not appear in the analyses of Carlson (1980), Stewart and Macpherson (1989) but is similar to the feature reported by Donaldson and Stewart (1989) for their east-coast winter storm.

Figure 4.15 illustrates the flow along these three isentropic surfaces.

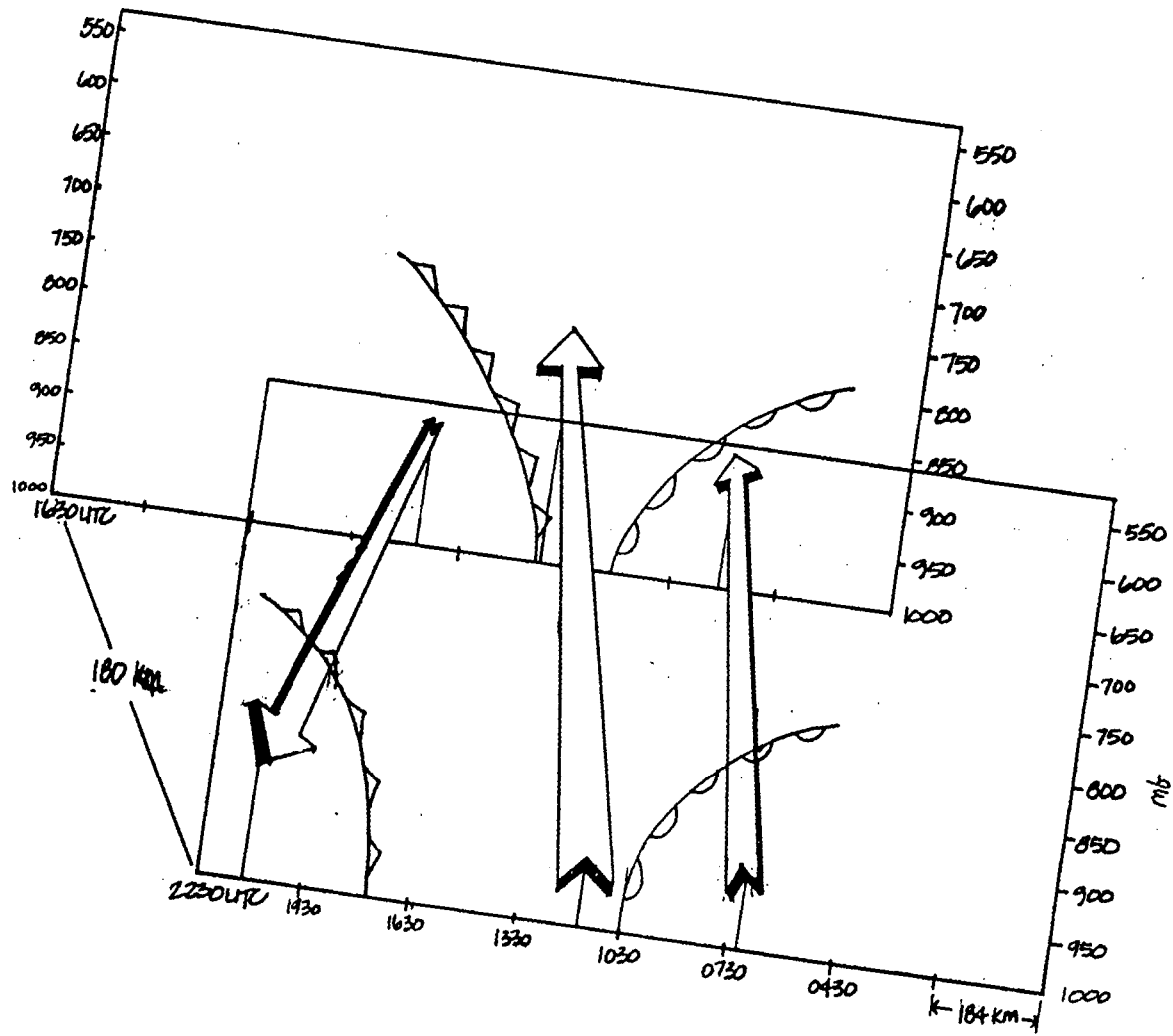


Figure 4.15: Three air-streams along isentropic surfaces as described in text.

## Chapter 5

### Diagnosis of Frontogenesis

#### 5.1 Introduction

Since frontal zones characteristically exhibit large gradients of horizontal potential temperature and static stability we can use prognostic equations for these parameters to study the kinematic frontogenetic processes. A number of authors have used similar analyses (eg. Miller, 1948b; Sanders, 1955; Rao, 1966; Ogura and Portis, 1982; Baldwin et al., 1984; Bond and Fleagle, 1985) to study the characteristics of frontogenesis of individual storm events.

Defining frontogenesis as the process that acts to concentrate the gradient of any given property  $\xi$  (Petterssen, 1956) we can create a three-dimensional frontogenetic function  $F_3$ , such that

$$F_3 = \frac{d}{dt} (\nabla_3 \xi). \quad (5.1)$$

Now, upon expanding  $\nabla_3$  and  $d/dt$ , equation 5.1 becomes

$$F_3 = \nabla_3 \frac{d\xi}{dt} - \left( \frac{\partial \xi}{\partial x} \nabla_3 u + \frac{\partial \xi}{\partial y} \nabla_3 v + \frac{\partial \xi}{\partial p} \nabla_3 \omega \right). \quad (5.2)$$

This equation is the same as the scalar formulation of Miller (1948b). In the following sections we will study cross-frontal and vertical gradients, the frontogenetic functions  $F_x$  and  $F_p$ . The corresponding components from equation 5.2 are

$$F_x = \frac{d}{dt} \left( \frac{\partial \xi}{\partial x} \right) = \overbrace{\left( \frac{\partial}{\partial x} \frac{d\xi}{dt} \right)}^A + \overbrace{\left( - \frac{\partial \xi}{\partial x} \frac{\partial u}{\partial x} - \frac{\partial \xi}{\partial y} \frac{\partial v}{\partial x} - \frac{\partial \xi}{\partial p} \frac{\partial \omega}{\partial x} \right)}^B, \quad (5.3)$$

and

$$F_p = \frac{d}{dt} \left( \frac{\partial \xi}{\partial p} \right) = \overbrace{\left( \frac{\partial}{\partial p} \frac{d\xi}{dt} \right)}^A + \overbrace{\left( - \frac{\partial \xi}{\partial x} \frac{\partial u}{\partial p} - \frac{\partial \xi}{\partial y} \frac{\partial v}{\partial p} - \frac{\partial \xi}{\partial p} \frac{\partial \omega}{\partial p} \right)}^B. \quad (5.4)$$

in a co-ordinate system moving with the front under investigation.

In both the equations above terms *A* represent nonconserved effects such as diabatic heating. Terms *B*, the kinematic effects, are shown in figure 5.1.

The terms in these equations were calculated for the ship Vancouver as described in the previous section. An error analysis was also performed following the technique and uncertainties shown in the previous sections. Figures are plotted such that only contour lines greater than the calculated uncertainties are included.

## 5.2 Horizontal Potential Temperature Gradient

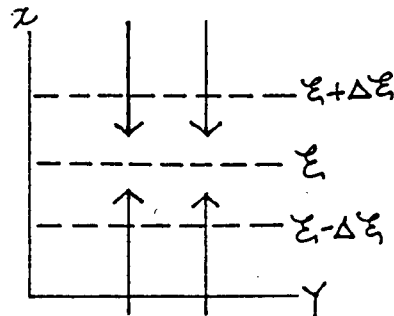
To investigate the effects of frontogenesis on the horizontal equivalent potential temperature gradient the form of Petterssen's frontogenetic function given in equation 5.3 is used after substituting  $\theta_e$  for  $\xi$ . The resulting equation is

$$\overbrace{\frac{d}{dt} \left( \frac{\partial \theta_e}{\partial x} \right)}^I = - \overbrace{\left( \frac{\partial u}{\partial x} \frac{\partial \theta_e}{\partial x} \right)}^{II} - \overbrace{\left( \frac{\partial v}{\partial x} \frac{\partial \theta_e}{\partial y} \right)}^{III} - \overbrace{\left( \frac{\partial \omega}{\partial x} \frac{\partial \theta_e}{\partial p} \right)}^{IV} + \overbrace{\left( \frac{\partial}{\partial x} \frac{d\theta_e}{dt} \right)}^V. \quad (5.5)$$

Term *I* is the time rate of change of  $\partial\theta_e/\partial x$  in the frame of reference moving with the front. Term *II* represents confluence (diffluence) concentrating (weakening) the cross-frontal  $\theta_e$  gradient. The effects of horizontal shear in rotating the along front temperature gradient into the cross-frontal direction are taken into account in term *III*. Term *IV* quantifies the tilting of the isentropes by differential vertical motion. The final term accounts for the effects of the gradient of the diabatic heating rate.

The confluence term, Term *II*, represents the increase (decrease) in the baroclinicity

### A CONFLUENCE



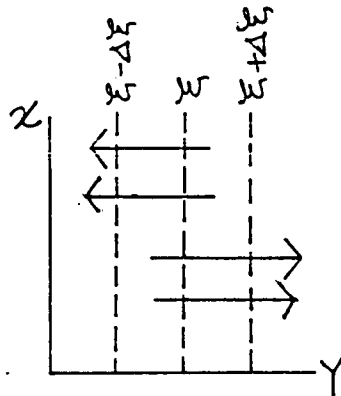
$$\partial u / \partial x < 0$$

$$\partial \xi / \partial x > 0$$

$$-(\partial u / \partial x) \cdot (\partial \xi / \partial x) > 0$$

FRONTOGENETIC

### B SHEAR



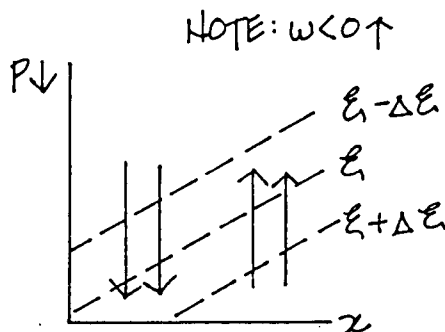
$$\partial \xi / \partial y > 0$$

$$\partial v / \partial x < 0$$

$$-(\partial v / \partial x) \cdot (\partial \xi / \partial y) > 0$$

FRONTOGENETIC

### C. TILTING



$$\partial w / \partial x < 0$$

$$\partial \xi / \partial p > 0$$

$$-(\partial w / \partial x) \cdot (\partial \xi / \partial p) > 0$$

FRONTOGENETIC

Figure 5.1: Frontogenetical effect of terms from equation. Frontogenesis due to; a) confluence, b) shear, and c) tilting. Vectors represent winds, dashed lines are contours of  $\xi$ .

$(\partial\theta_e/\partial x)$  by the convergence (divergence) of the cross-frontal horizontal wind. The maximum contribution of this term will occur in regions where high values of baroclinicity are coincident with large convergence. Figure 5.2 shows the distribution of this term  $(-\frac{\partial u}{\partial x} \frac{\partial \theta_e}{\partial x})$ . Throughout the cold frontal zone, with the exception of the lowest 25 mb, this term is frontolytic ( $< 0$ ). This occurs since both divergence (figure 4.5) and baroclinicity (figure 3.12) show positive maxima in the cold transition region. While there is a peak of convergence in the warm frontal zone the coincidental negative temperature gradient leads to a frontolytic contribution in this region as well. In the lowest regions of the cross-section the frontal zones are the only areas with values greater than the uncertainties. Table 5.1 lists the maximum values of each term in the prognostic equation for  $(d/dt)(\partial\theta_e/\partial x)$  for this study and that of Bond and Fleagle (1985) as well as the terms of the equation for  $(d/dt)(\partial\theta/\partial x)$  as used by other authors. In this case, the confluence term contributes to frontolysis in both the cold and warm frontal zones with the peaks of  $-1.9 \times 10^{-9} \text{ }^\circ\text{K m}^{-1}\text{s}^{-1}$  and  $-1.1 \times 10^{-9} \text{ }^\circ\text{K m}^{-1}\text{s}^{-1}$  at 875 mb and 900 mb respectively. We note that for all of the other studies where this term was a large component, it acted frontogenetically. This is primarily due to the fact that the other studies each exhibited convergence in the cold frontal zone as opposed to the divergence shown in the present case. Note that the studies of Bond and Fleagle (1985) and Sanders (1955), which showed terms more than two orders of magnitude greater than the others, were calculated for horizontal scales of 700 m and 25 km respectively. These small scales account for the large gradients needed to produce terms with these high magnitudes. The study of Rao (1966) was the only one of those listed in table 5.1 that exhibited a cold-warm frontal structure similar to ours. The others were all concerned with either occluded or cold fronts alone. The Rao (1966) study showed frontogenetic tendencies due to this term that were of the same magnitude (but opposite sign) as ours in both the warm and cold zones. The front studied by Ogura and Portis (1982) also exhibited a frontogenetic effect of similar

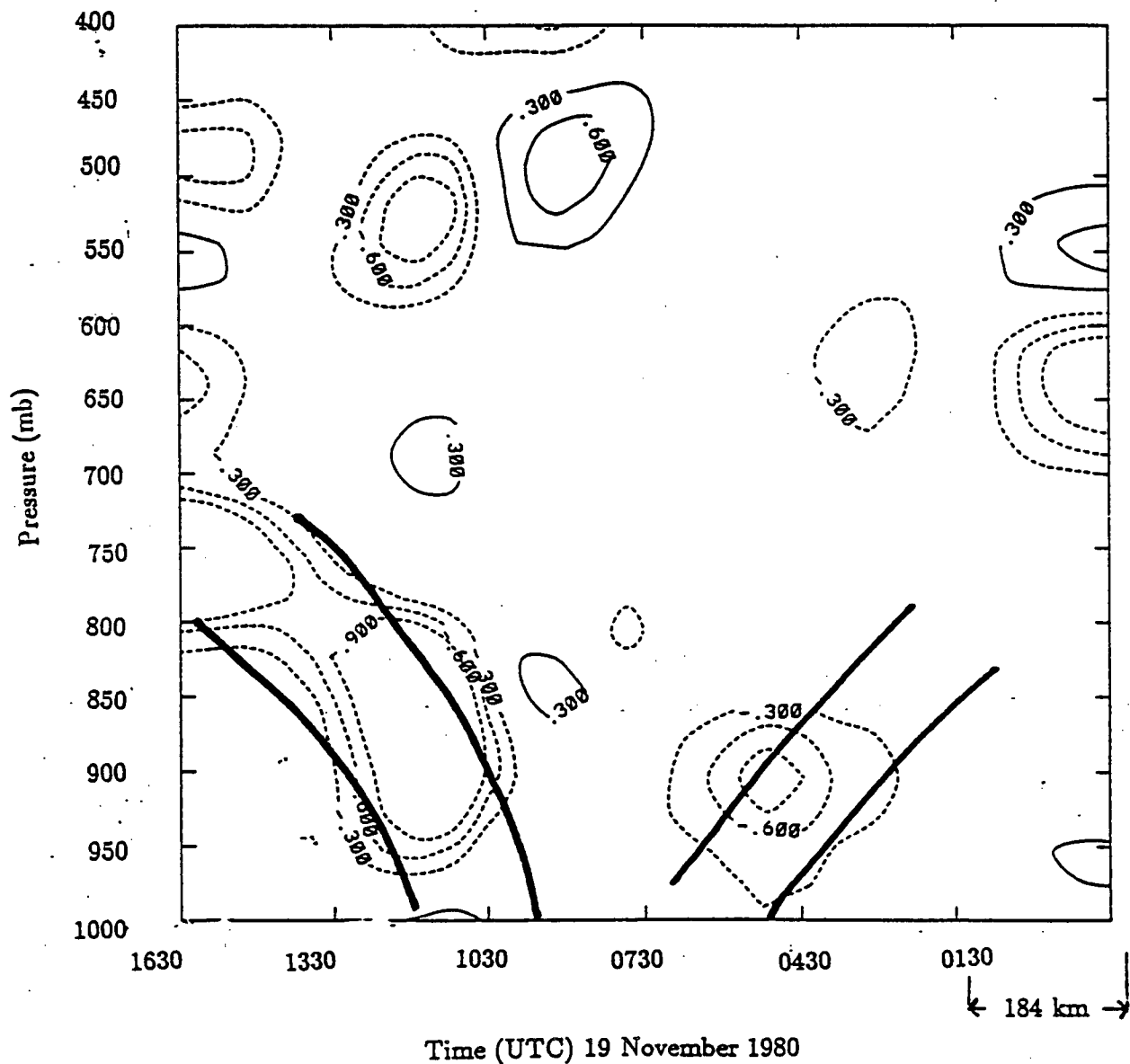


Figure 5.2: Time-Pressure cross section of frontogenetical effect of  $(-\frac{\partial u}{\partial x} \frac{\partial \theta_e}{\partial x})$ . Positive values indicate frontogenesis in the  $\theta_e$  field (Units  $10^{-9} \text{ } ^\circ K m^{-1} s^{-1}$ ). Contours greater than  $\pm 0.9 \times 10^{-9} \text{ } ^\circ K m^{-1} s^{-1}$  not included.

Frontogenesis terms ( $\times 10^{-9} \text{ }^\circ\text{K m}^{-1}\text{s}^{-1}$ )								
Study	Confluence		Twisting		Tilting		Diabatic	
	Max	Ht(mb)	Max	Ht(mb)	Max	Ht(mb)	Max	Ht(mb)
Present	-1.9 -1.1	875C 900W	+1.5 +0.9	875C 900W	$\leq -0.01$		$\leq 0.06$	PBL
MS	$\leq \pm 0.3$		$\leq 1$		-0.6	800C	4.0	
BF	$+2 \times 10^3$	900C			$+10 \times 10^3$ $-90 \times 10^3$	950C 875C	$1 \times 10^3$	950C
OP		+2.0 900C *			-1.6	900C		
Sanders	+460	950C			-370	950C		
Baldwin	+0.5	900C	+0.7	950C			-0.5 850C *	
Rao	+0.6 +1.2	800C 800W			-1 -0.9	800C 800W		

Table 5.1: Typical maximum values of frontogenetic terms for a number of studies; Ht refers to height of maximum magnitude, W refers to the warm frontal zone; C refers to the cold frontal zone; \* these two terms were summed in their figures; MS stands for McBean and Stewart (personal communication); OP for Ogura and Portis (1982); BF for Bond and Fleagle (1985); Sanders for Sanders (1955); Baldwin for Baldwin et al. (1984); Rao for Rao (1966); and PBL for Planetary Boundary layer.

magnitude to the frontolytic effect in our cold frontal zone, although they combined the confluence and twisting terms in their figure. The confluence term in both Baldwin et al. (1984) and McBean and Stewart (personal communication) were one order of magnitude smaller than in the present study.

Term III represents the twisting of the along front gradient of  $\theta_e$  into the cross frontal direction by the horizontal wind shear (which is approximately the vertical component of relative vorticity). The maximum contribution of this twisting term occurs where the relative vorticity and along frontal temperature gradients exhibit coincidentally large magnitudes. Since the vorticity (figure 4.12) is strongly positive in the frontal zones and  $\partial\theta_e/\partial y$  (figure 3.14)  $< 0$  everywhere we would expect positive contributions towards frontogenesis from the shear term in both frontal zones. Figure 5.3 shows a plot of this

twisting term, in both the warm and cold frontal regions it does indeed contribute towards frontogenesis. In a similar manner to the confluence term it is primarily the peaks in the two frontal zones that have magnitudes larger than the calculated uncertainty. The maximum contribution in the cold frontal zone is  $+1.5 \times 10^{-9} \text{ }^\circ\text{K m}^{-1}\text{s}^{-1}$  at 850 mb and both in and just above the warm frontal zone at 900 and 800 mb there are secondary peaks contributing toward frontogenesis of  $+0.9 \times 10^{-9} \text{ }^\circ\text{K m}^{-1}\text{s}^{-1}$ . Baldwin et al. (1984) found that this shear term was frontogenetic in their study with peak values of  $+0.7 \times 10^{-9} \text{ }^\circ\text{K m}^{-1}\text{s}^{-1}$  in the lowest layers of the frontal zone. The study of McBean and Stewart (personal communication) showed that the magnitude of this term was small everywhere compared with other terms in the budget. All other authors assumed that the along-frontal variations of  $\theta_e$  were negligible, an assumption that in our case is not valid as indicated by the figures 2.3 and 3.14 as well as by the significance of this term.

The fourth, tilting, term accounts for the change in horizontal temperature gradient due to differential motion of the isentropic surfaces. This term presents some difficulties in quantifying due to the previously discussed uncertainties in determining the vertical velocity. The largest contribution of this term results from regions where large  $\partial\omega/\partial x$  and  $\partial\theta_e/\partial p$  occur together. For unstable air, this process will be frontogenetic ahead of an updraught of air and frontolytic behind it. This term (not shown) had a peak value ( $1.0 \times 10^{-11} \text{ }^\circ\text{K m}^{-1}\text{s}^{-1}$ ) that was two orders of magnitude smaller than those for the confluence and twisting terms. This result follows from the small values of calculated vertical velocity. Furthermore, due to the large calculated errors in the vertical velocity this term is smaller than the uncertainty everywhere. Sanders (1955), Rao (1966), Ogura and Portis (1982), and Baldwin et al. (1984) all found that the tilting term was frontolytic in the frontal zone but frontogenetic in the air just ahead of the frontal updraught (although they presented no evidence of values being greater than the uncertainties). However, these studies each used the prognostic equation for  $\theta$  rather than  $\theta_e$ . Bond and Fleagle

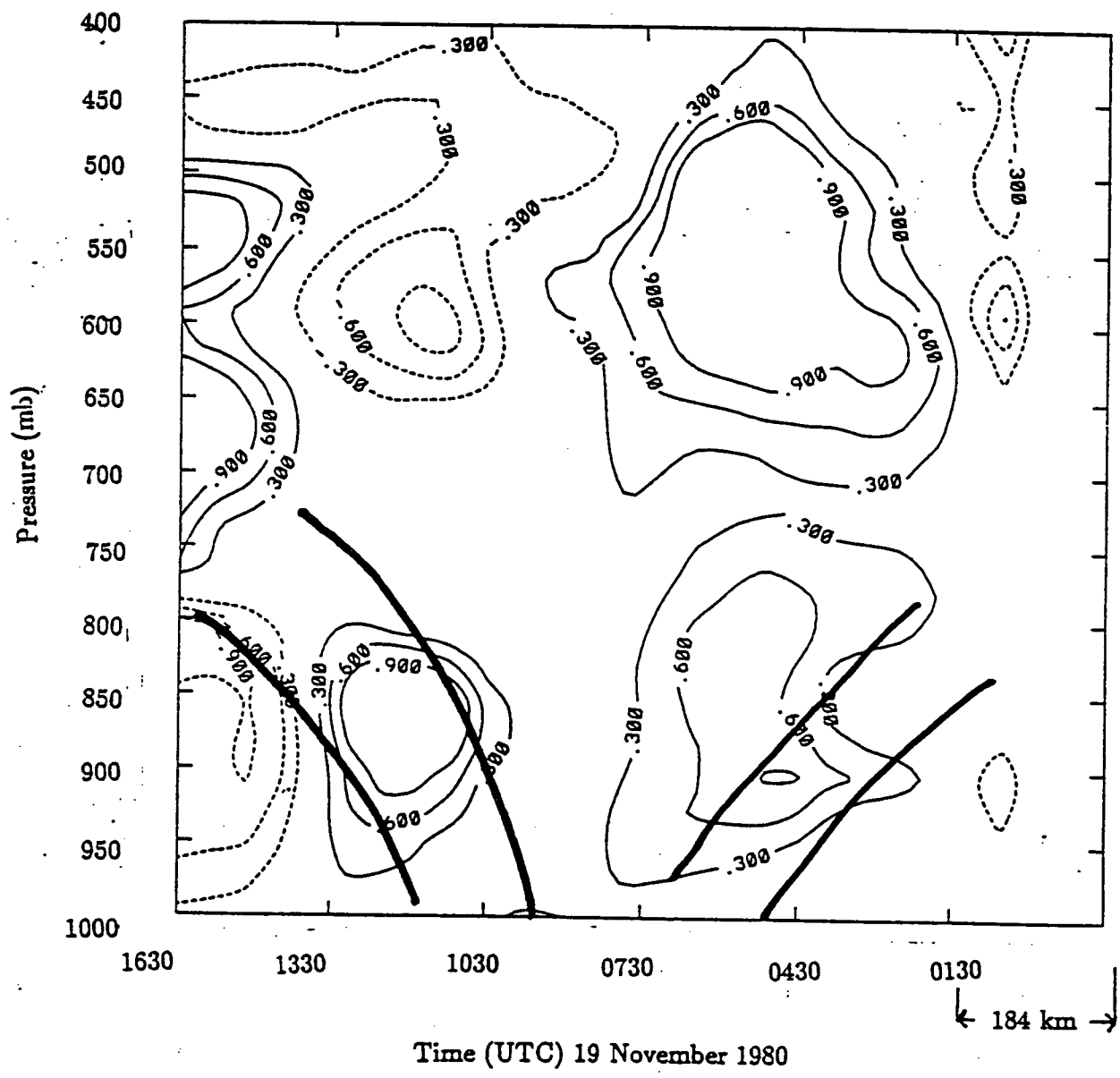


Figure 5.3: Time-Pressure cross section of frontogenetical effect of  $(-\frac{\partial v}{\partial x} \frac{\partial \theta_e}{\partial y})$ . Positive values indicate frontogenesis in the  $\theta_e$  field (Units  $10^{-9} \text{ } ^\circ\text{K m}^{-1}\text{s}^{-1}$ ). Contours greater than  $\pm 0.9 \times 10^{-9} \text{ } ^\circ\text{K m}^{-1}\text{s}^{-1}$  not included.

(1985), who used  $\theta_e$  in their calculations suggest that the large frontogenetic effect just ahead of the surface front shown by the other authors due to adiabatic cooling is actually offset by warming due to the release of latent heat, which is not included in  $\theta$ , but must be considered a diabatic effect. For this reason, the equivalent potential temperature, which takes into account condensation and evaporation, is more suited to calculations in regions near saturation. Furthermore, the uncertainties in determining vertical velocity make it desirable to use a variable which incorporates these phase changes rather than having to estimate their effect based on the  $\omega$  field.

Term  $V$  (not shown) accounts for the effects of the gradient of the diabatic heating rate. Following Baldwin et al. (1984), Bond and Fleagle (1985), and McBean and Stewart (personal communication) the effects of vertical divergence of the turbulent heat flux have been considered. Using wind speed and air-sea temperature differences recorded at the ship, bulk aerodynamic formulae were used to calculate the heat flux at the surface. The flux was then assumed to decrease linearly to the top of the boundary layer, which was determined subjectively from the radiosonde profiles. The resulting gradient of the diabatic heating rate (not shown) had a maximum magnitude of  $6.0 \times 10^{-11} \text{ }^\circ\text{K m}^{-1}\text{s}^{-1}$  and the term is therefore negligible when compared with the other terms.

Figure 5.4 shows the combined frontogenetic effect of the two dominant terms (confluence and twisting) in equation 5.5,  $\simeq \left( \frac{d}{dt} \frac{\partial \theta_e}{\partial x} \right)$ . The cold frontal zone, except for the very lowest layer, is a region of net frontolysis with maximum values near  $-1.0 \times 10^{-9} \text{ }^\circ\text{K m}^{-1}\text{s}^{-1}$  through the region. In the warm frontal zone, the combination of the frontogenetic effect of the twisting term and the frontolytic effect of the confluence term counteract each other and the net effect is neither frontogenetic nor frontolytic. Just above the warm frontal zone, at 825 mb, there is frontogenesis with a magnitude of about  $0.9 \times 10^{-9} \text{ }^\circ\text{K m}^{-1}\text{s}^{-1}$ . Below 600 mb, with exception of the extreme western portion and the two previously discussed regions, the values for the remainder of the section are

below the uncertainty. Behind the cold front in the lowest layers the small magnitude of the confluence term and the strong frontolysis of the twisting term combine to give a region of net frontolysis that is larger than the errors. However, since this region lies on the edge of the data used we have less confidence in the validity of the spline derivatives and therefore in this field at the edge of the cross-section. In the warm frontal zone the significant frontogenesis of the twisting term and the frontolysis of the confluence oppose each other such that the net effect is values of frontogenesis that are smaller than the uncertainty.

### 5.3 Static Stability

In a similar manner to that for baroclinicity we develop an equation for the frontogenetic (destabilizing) effect on the static stability by using equation 5.4 and again substituting  $\theta_e$  for  $\xi$ . This results in

$$\overbrace{\frac{d}{dt} \left( \frac{\partial \theta_e}{\partial p} \right)}^I = - \overbrace{\left( \frac{\partial u}{\partial p} \frac{\partial \theta_e}{\partial x} \right)}^{II} - \overbrace{\left( \frac{\partial v}{\partial p} \frac{\partial \theta_e}{\partial y} \right)}^{III} - \overbrace{\left( \frac{\partial \omega}{\partial p} \frac{\partial \theta_e}{\partial p} \right)}^{IV} + \overbrace{\left( \frac{\partial}{\partial p} \frac{d\theta_e}{dt} \right)}^V. \quad (5.6)$$

Term *IV* in equation 5.6 represents the confluence of  $\partial\theta_e/\partial p$  by convergence in the vertical velocity field. Terms *II* and *III* combine to represent the shear or twisting terms, rotating the cross or along frontal temperature gradients into the vertical by vertical shear in the cross and along frontal winds. There is no analogy to the tilting term of equation 5.5. Term *V* again represents the effect of diabatic heating. The static stability,  $\partial\theta_e/\partial p$ , has been evaluated and is shown in figure 3.10 with the boundary layer being unstable and the areas of greatest stability occurring in the upper cold and warm frontal zones. Since no other studies exist that have studied the destabilizing effect on static stability in this manner, there are no results to compare with those of this study.

The first of the shear terms, term *II*, results from an interaction of the vertical

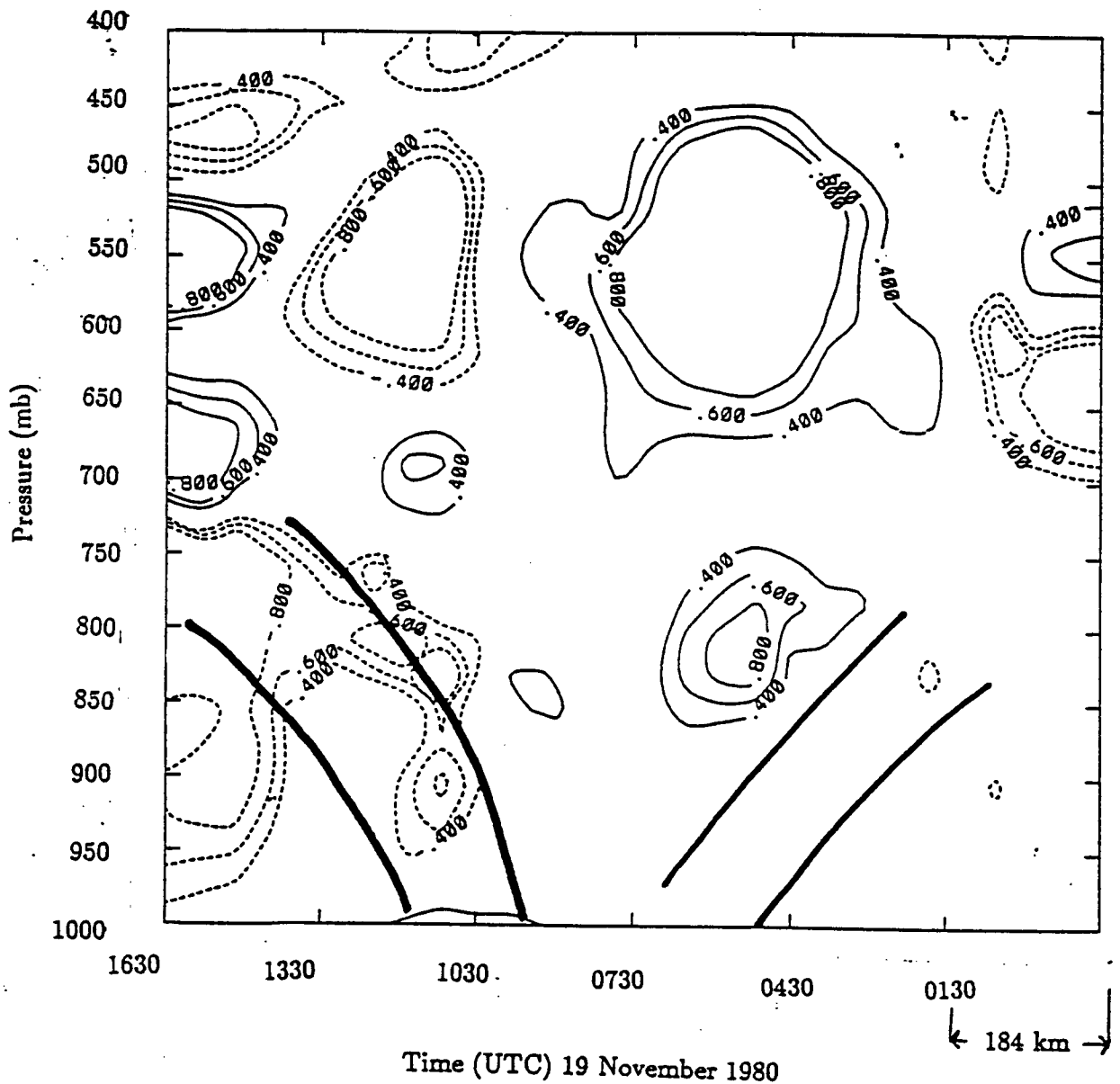


Figure 5.4: Time-Pressure cross section of total frontogenetic effect of confluence and twisting terms  $\approx \left(\frac{d}{dt} \frac{\partial \theta_e}{\partial x}\right)$ . Positive values indicate frontogenesis in the  $\theta_e$  field (Units  $10^{-9} \text{ } ^\circ K m^{-1} s^{-1}$ ). Contours greater than  $\pm 0.8 \times 10^{-9} \text{ } ^\circ K m^{-1} s^{-1}$  not included.

gradient of the  $u$  wind and the cross-front horizontal gradient of equivalent potential temperature. The greatest effect of this term occurs when the vertical  $u$  wind shear and the cross-wind  $\theta_e$  gradient have coincidental maximum contributions.  $\partial\theta_e/\partial x$  (figure 3.12) is positive throughout the cold frontal zone and negative in the warm frontal region. This combines with the  $u$  wind (figure 4.1) generally increasing with height to produce the effect shown in figure 5.5. This term is frontogenetic in the cold frontal zone with peaks near the surface and in the upper levels of the transition zone of  $3.5 \times 10^{-8} \text{ }^\circ\text{K s}^{-1} \text{Pa}^{-1}$  and  $4.5 \times 10^{-8} \text{ }^\circ\text{K s}^{-1} \text{Pa}^{-1}$  respectively. The peak in the negative, or frontolytic field, is  $-3.5 \times 10^{-8} \text{ }^\circ\text{K s}^{-1} \text{Pa}^{-1}$  at 950  $mb$  in the warm frontal zone. McBean and Stewart (personal communication) found a similar pattern, although in their case the locations of the peak magnitudes were 50 – 100  $mb$  higher and their peak magnitudes for both frontogenetic and frontolytic forcing were  $\sim 1.0 \times 10^{-8} \text{ }^\circ\text{K s}^{-1} \text{Pa}^{-1}$ .

Term III, the second of the shear terms in equation 5.6, results from the interaction of the vertical gradient of the  $v$  wind and the along-frontal gradient of equivalent potential temperature.  $\partial\theta_e/\partial y$  is negative everywhere in the cross-section (figure 3.14), the along front component of wind is decreasing with height in the lower regions to the west of the surface cold front and then increases with height above 850  $mb$ . In the warm frontal zone  $\partial v/\partial p$  is generally negative (wind speed increasing with height). The combined effects of these components (figure 5.6) is a frontogenetic maximum with a peak magnitude of  $1.6 \times 10^{-8} \text{ }^\circ\text{K s}^{-1} \text{Pa}^{-1}$  occurring at 950  $mb$  in the warm frontal zone. Near 850  $mb$  in the cold frontal zone is a region where this term is strongly frontolytic ( $-2.5 \times 10^{-8} \text{ }^\circ\text{K s}^{-1} \text{Pa}^{-1}$ ) which is coincident with the strong gradient on the top of the southward flowing low level jet shown in figure 4.2. McBean and Stewart (personal communication) found a similar peak in the upper cold frontal zone.

The fourth term (not shown) on the right hand side of equation 5.6 accounts for the change in  $\partial\theta_e/\partial p$  by convergence in the vertical motion field. The  $\partial\omega/\partial p$  field shows

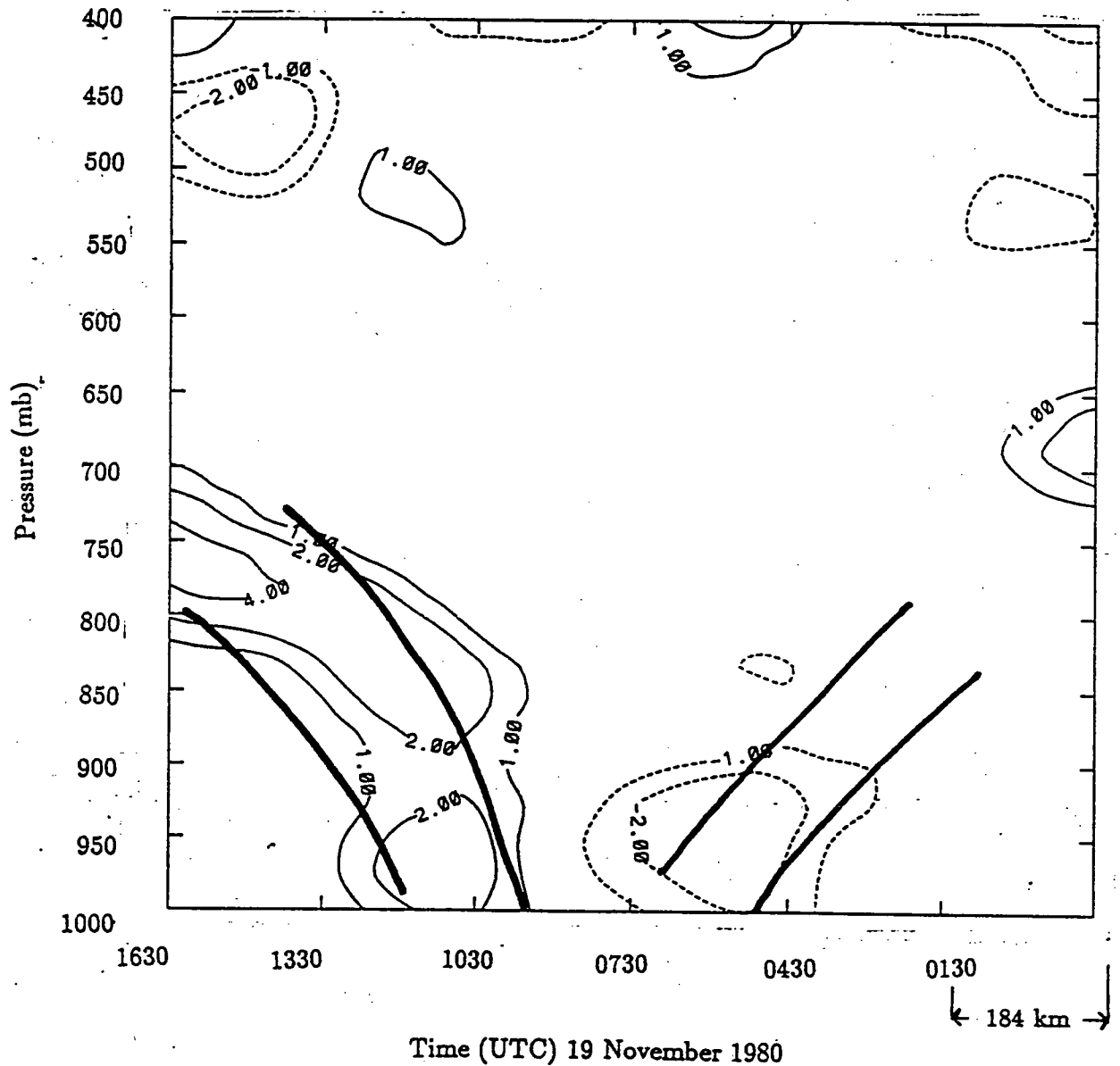


Figure 5.5: Time-Pressure cross section of frontogenetical effect of  $(-\frac{\partial u}{\partial p} \frac{\partial \theta_e}{\partial x})$ . Positive values indicate frontogenesis in the  $\theta_e$  field (Units  $10^{-8} \text{ } ^\circ K s^{-1} Pa^{-1}$ ). Contours greater than  $\pm 4.0 \times 10^{-8} \text{ } ^\circ K s^{-1} Pa^{-1}$  not included.

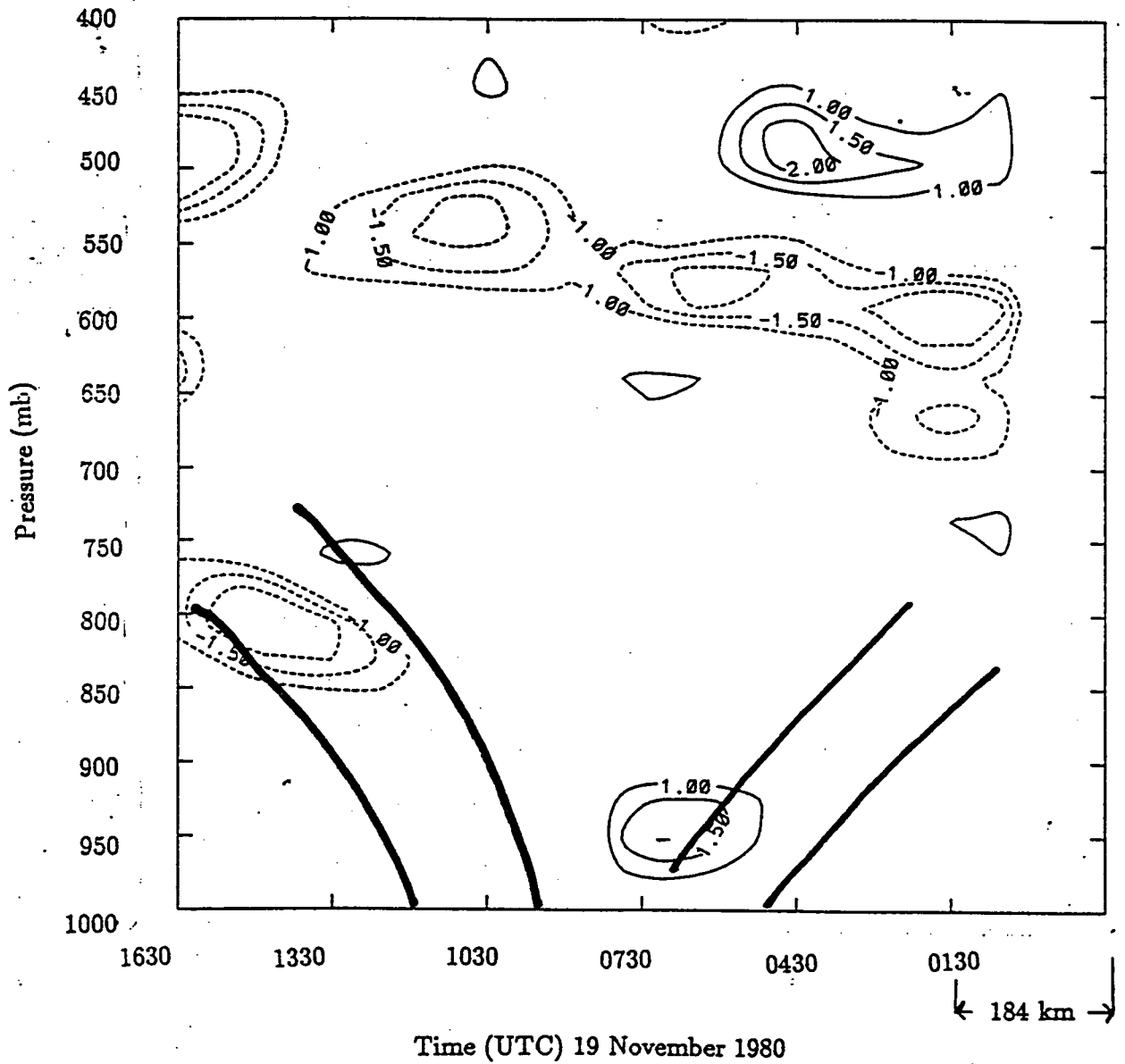


Figure 5.6: Time-Pressure cross section of frontogenetical effect of  $(-\frac{\partial v}{\partial p} \frac{\partial \theta_e}{\partial y})$ . Positive values indicate frontogenesis in the  $\theta_e$  field (Units  $10^{-8} \text{ } ^\circ K \text{ s}^{-1} Pa^{-1}$ ). Contours greater than  $\pm 2.0 \times 10^{-8} \text{ } ^\circ K \text{ s}^{-1} Pa^{-1}$  not included.

considerable fluctuations but it indicates a peak negative value in the upper cold frontal zone near  $825\text{ mb}$  that is nearly coincidental with the region of maximum stability previously discussed. The vertical derivative of  $\omega$  is also strongly negative at  $900\text{ mb}$  in the cold frontal zone, however the same region shows nearly neutral stability with respect to  $\theta_e$ . The upper cold frontal zone is a region of peak frontolytic effect due to this term. However the magnitude is  $> 0.5 \times 10^{-8} \text{ }^\circ\text{K s}^{-1}\text{Pa}^{-1}$  in this region and much less everywhere else. Therefore, this term is not significant when compared with the previous two or when compared with the uncertainties. In the study of their storm, McBean and Stewart (personal communication) found this term to dominate the other two between  $900 - 950\text{ mb}$  in the cold frontal zone with a magnitude of  $\sim 5.0 \times 10^{-8} \text{ }^\circ\text{K s}^{-1}\text{Pa}^{-1}$ .

The last term (not shown) in equation 5.6 represents the effects of the vertical gradient of diabatic heating. Since we are using the equivalent potential temperature, the effects of condensation, evaporation, and precipitation melting need not be considered. The divergence of the turbulent heat flux was calculated following the technique outlined in the previous section and the resulting term was again at least two orders of magnitude smaller than the magnitudes of the confluence and twisting terms.

Figure 5.7 shows the combined frontogenetic effect of the two dominating twisting terms on the right hand side of equation 5.6,  $\simeq d/dt(\partial\theta_e/\partial p)$ . In the upper cold frontal zone the frontolysis of the second shear term cannot completely offset the frontogenetic effect of first and the result is a frontogenetic component of  $4.5 \times 10^{-8} \text{ }^\circ\text{K s}^{-1}\text{Pa}^{-1}$  at  $750\text{ mb}$ . In the lower cold frontal zone, where both terms are positive, the combined effect is also frontogenetic with a magnitude of  $3.5 \times 10^{-8} \text{ }^\circ\text{K s}^{-1}\text{Pa}^{-1}$  just above the surface. The lower warm frontal region undergoes frontogenesis due to the second term and stronger frontolysis due to first. The combined effect is frontolysis of  $2.5 \times 10^{-8} \text{ }^\circ\text{K s}^{-1}\text{Pa}^{-1}$  at  $950\text{ mb}$ .

Baldwin et al. (1984) studied the destabilizing effect on static stability using a slightly

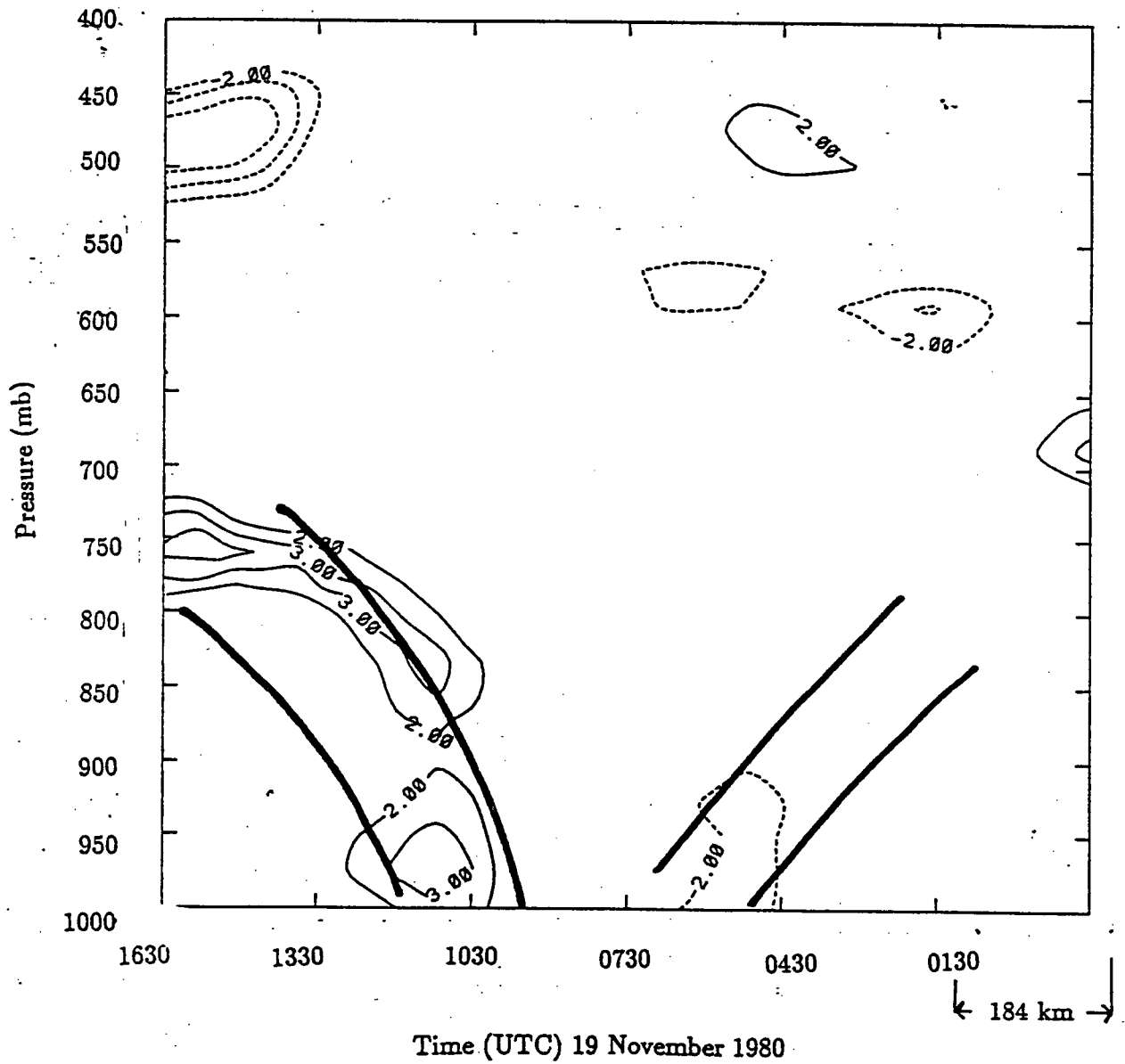


Figure 5.7: Time-Pressure cross section of total frontogenetic effect of the two twisting terms  $\approx \left(\frac{d}{dt} \frac{\partial \theta_e}{\partial p}\right)$ . Positive values indicate frontogenesis in the  $\theta_e$  field (Units  $10^{-8} \text{ }^\circ\text{K s}^{-1} \text{Pa}^{-1}$ ). Contours greater than  $\pm 4.0 \times 10^{-8} \text{ }^\circ\text{K s}^{-1} \text{Pa}^{-1}$  not included.

different equation,

$$\overbrace{\frac{d}{dt} \left( \frac{\partial \theta}{\partial \sigma} \right)}^I = - \overbrace{\left( \frac{\partial u_a}{\partial \sigma} \frac{\partial \theta_e}{\partial x} + \frac{\partial v_a}{\partial \sigma} \frac{\partial \theta}{\partial y} \right)}^{II} - \overbrace{\left( \frac{\partial u_g}{\partial \sigma} \frac{\partial \theta}{\partial x} + \frac{\partial v_g}{\partial \sigma} \frac{\partial \theta}{\partial y} \right)}^{III} - \overbrace{\left( \frac{\partial \omega}{\partial \sigma} \frac{\partial \theta}{\partial \sigma} \right)}^{IV} - \overbrace{\left( \frac{\partial}{\partial \sigma} \frac{d\theta}{dt} \right)}^V. \quad (5.7)$$

where  $u_a$  and  $v_a$  refer to the ageostrophic wind components, those with subscripts  $g$  stand for the geostrophic components, and  $\sigma$  is the vertical co-ordinate. They called term *II* the tilting of the horizontal potential temperature gradient into the vertical by the ageostrophic wind shear. This term is negative (stabilizing) throughout the frontal zone and while the two terms oppose each other behind the front, a stable capping inversion was generated because of the dominance of the  $u_a$  term. Note that we can not compare their magnitudes with ours since they use sigma co-ordinates. Baldwin et al. (1984) also found that their compression term (*IV* in equation 5.7) was frontolytic in the lower levels of the frontal zone, and of similar magnitude to the term above.

#### 5.4 Summary

A kinematic analysis of the frontogenetic processes acting on  $\partial \theta_e / \partial x$  and  $\partial \theta_e / \partial p$  has been performed employing the prognostic equations for these variables. The main kinematic influences on frontogenesis can be allocated into effects due to confluence, twisting (shear), tilting, and diabatic heating.

The prognostic equation for  $\partial \theta_e / \partial x$  was dominated by the confluence and the shear terms. Contrary to the findings of other authors, the confluence of the cross-frontal wind acted frontolytically in the frontal zones of this storm. This is a direct consequence of the observed horizontal divergence in the cold frontal zone. While most other authors assumed that the along-front  $\theta_e$  gradient, and therefore the twisting term, was negligible it proved to be one of the two large components in this analysis. Shear acted to increase

the cross-frontal  $\theta_e$  gradient in both the warm and cold frontal zones of this study. Other authors have found the tilting term to be of major importance. In this analysis the term was everywhere smaller than the estimated uncertainty in its calculation. Two factors may account for this discrepancy. First, the vertical velocities calculated in this study were generally at least one order of magnitude smaller than those determined by the other authors. Second, most of the other authors used  $\theta$  rather than  $\theta_e$  in their calculations which artificially enhances the importance of this term in regions of strong updraughts by adding the effects of adiabatic cooling but not the offsetting effect of condensation (which is included in this term if  $\theta_e$  is used). This difference in the technique used for the calculation also affects the diabatic heating term. In the studies which used  $\theta$  the heating (cooling) due to condensation (evaporation) show up in this term while calculations using  $\theta_e$  have included these effects in other terms. Diabatic heating due vertical divergence of the turbulent heat flux was small everywhere. The results of this analysis show that two strong effects, the frontolysis of the confluence term and the frontogenesis caused by the shear term, work to counteract each other and the combined effect is smaller than the uncertainty almost everywhere.

The prognostic equation for  $\partial\theta_e/\partial p$  was dominated by the two shear terms. The first of these terms produced a frontogenetic effect in the cold frontal zone and was frontolytic in the warm transition region. The second twisting term is frontogenetic everywhere in the lowest layers and frontolytic in the upper cold frontal zone. As with the previous analysis the terms accounting for differential vertical motion and diabatic heating were much smaller than the first two. The term representing the effect of the convergence of the vertical velocity was also insignificant in this case. The combined frontogenetic effect on the prognostic equation for  $\partial\theta_e/\partial p$  shows that the cold frontal zone is undergoing significant frontogenesis while the warm frontal zone is a region of strong frontolysis.

## Chapter 6

### Summary and Conclusions

The wave cyclone that passed through the STREX study area of the northeast Pacific Ocean on 19 November 1980 has been analysed on the basis of its synoptic, thermodynamic, and kinematic structures and these have been used to diagnose the important processes influencing the kinematic frontogenesis of the storm. This was the third vigorous storm in succession to influence the area and while it was similar in some aspects to the other two, it also exhibited significant differences.

This system consisted of a frontal wave associated with linked surface and upper air low pressure centres and a strong southwesterly flow aloft. A large comma shaped cloud pattern with a well defined trailing edge, typical of mid-latitude frontal systems, was also associated with the storm. Tracking of features from the satellite images and surface analyses indicated that the fronts and clouds were moving with a speed of  $17\text{ ms}^{-1}$  from  $240^\circ$ . Surface observations indicate that there were significant changes in wind speed and direction, dry and wet bulb temperatures and wet bulb depression, and pressure tendency as both the cold front and the warm front passed by the observing platforms. Precipitation was recorded at the ship Vancouver for two hours up to the time of the warm front passage and for brief period just ahead of the cold front while the Oceanographer, 180 km further to the south, experienced light rain throughout most of the day.

Pressure-time (pressure-distance) cross-sections were constructed from the data gathered from radiosondes released at each ship. The temperature cross-sections for both ships show strong thermal gradients in both the cold and warm frontal zones. The fronts, when

defined on this thermal basis, agree with times of frontal passage as determined by the surface observations. Contours of the relative humidity field support the cloud pattern as indicated by the satellite images and the surface observations. The Vancouver's cross-section exhibits a large gradient on the trailing western edge of the clouds that is similar to an upper, or moisture front, as shown by other authors. The western region of the relative humidity field at the Oceanographer does not show this sharp gradient. This difference in the field may be due to either the missing sounding at the southern ship or simply along-front variations in the humidity.

Detailed profiles of the sounding data show that both the pre and post-frontal boundary layers were moist with dryer air above the base of the capping inversion. The post frontal boundary layer was deeper than the pre frontal one and there was no well defined boundary layer in the warm sector of the storm.

Cross-sections indicate that the pre and post frontal boundary layers were statically unstable with respect to the equivalent potential temperature and that there was a region of marked stability in the extreme upper cold frontal regions in both sections. The cross-frontal gradients of  $\theta_e$  exhibit peak values in the frontal zones for both ships with a more intense gradient at the cold front than the warm for the Vancouver and the warm front gradient stronger than that of the cold front at the Oceanographer. The largest values of the along frontal equivalent potential temperature gradient occurred in the cold frontal transition zone.

The horizontal winds also exhibited very similar patterns at both ships. The cross-frontal wind showed a strong easterly inflow into the lower layers from the warm frontal side that carried through the system and resulted in a weak easterly outflow behind the cold front. In the middle layers the cross-frontal wind was very small relative to the speed of the system and there was a strong westerly flow at the higher levels. The along frontal wind component was generally southerly except for the region in the lowest layers

behind the cold front where a weak northerly flow existed. A strong low level southerly jet existed ahead of the warm front and this component remained large up to the higher levels. This jet is in the cold air ahead of the warm front and is the so-called cold conveyor belt.

The cross-frontal gradient of the  $u$  wind component was strongest in the frontal zones at both ships. At the Vancouver the gradients were largest in the cold frontal zone and at the Oceanographer the warm frontal zone was the most intense. The  $y$  gradient of the along frontal wind showed strong convergence in the warm frontal zone. These two components combine to form the horizontal divergence field, which exhibited divergence in the cold frontal zone and convergence in the warm transition region.

The vertical component of relative vorticity, which has been used by some authors to define fronts, consists of the sum of the cross-front gradient of the along frontal wind and the along front gradient of the cross-front wind. Since each term was large in the cold frontal zone, the resultant was also large. The along front gradient of the cross-frontal wind was large in and just to the west of the warm frontal zone. This contributes to the same pattern in the relative vorticity field.

The vertical velocity, which was calculated kinematically, depends on the horizontal divergence and therefore shows a similar pattern. Due to the strong divergence in the cold frontal zone, this region underwent downward motion and is classified a kata-front. East of the cold front the lowest layers experienced upward motion with the largest values occurring in the warm frontal zone. The velocities calculated were in general quite small however in most of the section below  $\sim 750$  mb they were greater than the uncertainties.

Relative isentropic analysis has led to the identification of three major air streams relative to the moving system. A warm moist stream, similar to the so-called warm conveyor belt, flows northward in the warm sector, rising from the south to the north. Slightly to the east of the warm front flows another air stream that resembles the cold

conveyor belt of other authors. A second cold air stream flows gradually to the south behind the cold front.

A kinematic diagnosis of the frontogenetic processes affecting this storm has been performed by analysing prognostic equations for the cross-front potential temperature gradient (baroclinicity) and the static stability. In studying the baroclinicity we found that confluence and shear were the only terms that were significant with respect to the uncertainties while only the shear terms were important for the static stability. In the equation for baroclinicity the confluence term acted frontolytically and the twisting (shear) term acted to increase the baroclinicity. In the case of static stability the first twisting term was frontogenetic in the cold frontal zone and frontolytic in the warm frontal zone. The second shear term acted frontogenetically in the lowest layers of the warm frontal zone and was frontolytic in the upper cold frontal zone. The combined effect was net frontogenesis throughout the cold frontal transition zone and frontolysis in the lower warm frontal region.

Comparing the results of this study with analyses of other storms, especially those of the previous two STREX systems, indicates both similarities and differences between the cases. As with most other studies the largest gradients of the parameters occur in the frontal zones. The upper (moisture) front at the Vancouver's cross-section has been found in the previous storm and by other authors. The line of maximum relative vorticity corresponds well with the front in both zones. While the vast majority of other studies show horizontal convergence as a main characteristic of frontal zones, the cold frontal zone of this storm exhibited divergence. As a result of the divergence the cold frontal zone was a region of downward vertical motion, a kata-front, which is much less common in the literature (but probably as common in the real world) than are ana-fronts. Most studies of frontal waves exhibit cold fronts that are much more intense than the warm frontal transition zones. In this study the two regions are of similar intensity at the

Vancouver and the warm front is the most vigorous as defined on a thermal basis at the Oceanographer. Authors of other studies of the frontogenetic processes acting on other systems have largely left the shear (twisting) term uncalculated. These results show that, at least for this case, this term can be very significant to dominant in the prognostic equations for frontal parameters. Furthermore, other studies have not included error analyses in the calculations of the frontogenetic terms and therefore their results may or may not be significant with respect the large uncertainties in calculating the terms.

Future studies should rely on greater data density to verify similarities and differences of features found in the various case studies. Greater spatial coverage in the along front direction would allow for more accurate reporting of the along-front gradients and allow extension of the relative isentropic analysis. Instrumentation that would provide direct measurement of the vertical wind component would also aid further studies as techniques used to infer this field from other variables either rely heavily on assumptions or have large uncertainties in their calculations.

## Bibliography

- [1] Austin, P. M., (1960) In *Physics of precipitaton* (H. Weickmann, ed.) Geophys. Monog., No. 5, Amer. Geophys. Union, 86-92
- [2] Baldwin, D. G., E. Y. Hsie and R. A. Anthes, (1984) Diagnostic studies of a two-dimensional simulation of frontogenesis in the moist atmosphere, *J. Atmos. Sci.*, 41, 2686-2700
- [3] Barford, N. C., (1986) *Experimental measurements: precision, error, and truth*, J. Wiley and Sons, 159 pp.
- [4] Bergeron, T., (1937) On the physics of fronts, *Bull. Amer. Metero. Soc.*, 18, 265-275
- [5] Bjerknes, J., (1919) On the structure of moving cyclones, *Geophys. Publ.*, 1, No. 2
- [6] Bjerknes, J. and E. Palmén, (1937) Investigations of selected European cyclones by means of serial ascents, *Geophys. Publ.*, 12, No. 2
- [7] Bjerknes, J. and H. Solberg, (1922) Life cycle of cyclones and the polar front theory of atmospheric circulations, *Geophys. Publ.*, 3, 3-18
- [8] Bond, N. A., (1986) *Boundary layer structure and processes in mid-latitude ocean storms*, Ph.D. Thesis, University of Washington
- [9] Bond, N. A. and R. E. Fleagle, (1985) Structure of a cold front over the ocean, *Q. J. Roy. Met. Soc.*, 111, 739-759
- [10] Bond, N. A. and R. E. Fleagle, (1987) Prefrontal and postfrontal processes boundary layer processes over the ocean, *Mon. Wea. Rev.*, 116, 1257-1272

- [11] Browning, K. A., (1971), *Weather*, 26, 320-340
- [12] Browning, K. A. and T. W. Harrold, (1970) Air motion and precipitation at a cold front, *Q. J. Roy. Met. Soc.*, 96, 369-389
- [13] Browning, K. A. and C. W. Pardoe, (1973) Structure of low level jet streams ahead of mid-latitude cold fronts, *Q. J. Roy. Met. Soc.*, 99, 619-638
- [14] Browning, K. A. and B. J. Mason, (1981) Air motion and precipitation growth in frontal systems, *Pageophy*, 119, 577-593
- [15] Browning, K. A., and G. A. Monk, (1982) A simple model for the synoptic analysis of cold fronts, *Q. J. Roy. Met. Soc.*, 108, 435-452
- [16] Carbone, R. E., (1982) A severe winter squall line. Stormwide thermodynamic structure, *J. Atmos. Sci.*, 39, 258-279
- [17] Carlson, T. N., (1980) Airflow through mid-latitude cyclones and the comma cloud pattern. *Mon. Wea. Rev.*, 108, 1498-1509
- [18] Eliassen, A., (1959) On the formation of fronts in the atmosphere, *Rosby Memorial Volume*, Rockefeller Institute and Oxford University, 277-287
- [19] Donaldson, N. R., and R. E. Stewart, (1989) On the precipitating regions within two storms affecting Atlantic Canada, *Atmos. Ocean*, 27, 108-129
- [20] Eliassen, A., (1962) On the vertical circulation in frontal zones, *Geophys. Publ.* (V. Bjerknæs Memorial Volume), 24, 147-167
- [21] Elliott, R. D. and E. L. Hovind, (1964) On convection bands within pacific coast storms and their relation to storm structure, *J. Appl. Meteorol.*, 3, 143-154

- [22] Fleagle, R. E., M. Miyake, J. F. Garrett, and G. A. McBean, (1982) Storm transfer and response experiment, *Bull. Amer. Metero. Soc.*, 63, 6-14
- [23] Fleagle, R. E., N. A. Bond, and W. A. Nuss, (1988) Atmosphere-ocean interaction in midlatitude storms, *Meteor. Atmos. Phys.*, 38, 50-63
- [24] Godske, C. L., T. Bergeron, J. Bjerknes, and R. C. Bundgaard, (1957) *Dynamic meteorology and weather forecasting*, Ch. 14, Amer. Metero. Soc., Boston Massachusetts.
- [25] Harrold, T. W., (1973) Mechanisms influencing the distribution of precipitation within baroclinic disturbances, *Q. J. Roy. Met. Soc.*, 99, 232-251
- [26] Haurwitz, B., et al., (1945) Advection of air and the forecasting of pressure changes, *J. Meteorol.*, 2, 83-93
- [27] Hobbs, P. V., R. A. Houze, and T. J. Matjeka, (1975) The dynamical and microphysical structure of an occluded frontal system and its modification by orography, *J. Atmos. Sci.*, 32, 1542-1562
- [28] Holton, J. R., (1979) *An introduction to dynamic Meteorology*, 2nd ed. Academic Press, 391 pp.
- [29] Hoskins, B. J. and F. P. Bretherton, (1972) Atmospheric frontogenesis models: mathematical formulation and solution. *J. Atmos. Sci.*, 29, 11-37
- [30] Hoskins, B. J. and I. Dragici, (1977) The forcing of ageostrophic motion according to the semigeostrophic equations and in an isentropic coordinate model, *J. Atmos. Sci.*, 34, 1859-1867

- [31] Houghton, H. G. and J. M. Austin, (1946) A study of non-geostrophic flow with applications to the mechanism of pressure changes, *J. Meteorol.*, 3, 57-77
- [32] Houze, R. A. and P. V. Hobbs, (1982) Organization and structure of precipitating cloud systems, *Adv. Geophys.*, 24, 225-315
- [33] Houze, R. A., J. D. Locatelli and P. V. Hobbs, (1976) Dynamics and cloud microphysics of the rainband in an occluded frontal system, *J. Atmos. Sci.*, 33, 1921-1936
- [34] Hsie, E. Y. and R. A. Anthes, (1984) Simulations of frontogenesis in a moist atmosphere using alternative parameterizations of condensation and precipitation, *J. Atmos. Sci.*, 41, 2701-2716
- [35] Keyser, D., (1986) Atmospheric fronts: an observational perspective, *Mesoscale Meteorology and Forecasting*, P. S. Ray. Ed., *Amer. Meteor. Soc.*, 216-258
- [36] Keyser, D. and R. A. Anthes, (1982) The influence of planetary boundary layer physics on frontal structure in the Hoskins-Bretherton horizontal shear model, *J. Atmos. Sci.*, 39, 1783-1802
- [37] Krietzberg, C. W., (1968) The mesoscale wind field in an occlusion, *J. Appl. Met.*, 7, 53-67
- [38] Krietzberg, C. W. and H. A. Brown, (1970) Mesoscale weather systems within an occlusion, *J. Appl. Met.*, 9, 417-432
- [39] McBean, G. A. and D. J. Phillips, (1986) A comparison of radar and Navaid windfinding systems, *J. Atmos. Oceanic Technol.*, 3, 191-196
- [40] McBean, G. A., D. J. Phillips, and J. R. Mathieson, (1986) An intercomparison of two radiosonde systems, *Atmos. Ocean*, 24, 42-52

- [41] McBean, G. A. and R. E. Stewart, (1991) Structure of a frontal system over the northeast pacific ocean, *Mon. Wea. Rev.*, 119, 997-1013
- [42] Miller, J. E., (1948a) Studies of large scale vertical motions of the atmosphere, *Meteorol. Papers* New York Univ., No. 1, 1-48
- [43] Miller, J. E., (1948b) On the concept of frontogenesis, *J. Meteorol.*, 5, 169-171
- [44] Murty, T. S., G. A. McBean and B. McKee, (1983) Explosive cyclogenesis over the northeast pacific ocean, *Mon. Wea. Rev.*, 111, 1131-1135
- [45] Newton, C. W., (1954) Frontogenesis and frontolysis as a three-dimensional process, *J. Meteorol.*, 11, 449-461
- [46] Ogura, Y. and D. Portis, (1982) Structure of a cold front observed in SESAME-AVE III and its comparison with the Hoskins-Bretherton frontogenesis model, *J. Atmos. Sci.*, 39, 2773-2792
- [47] Palmen, E. and C. W. Newton (1969) *Atmospheric circulation systems: their structure and physical interpretation*, Int. reophys. Ser., 13, Academic press, 603 pp.
- [48] Panofsky, H. A., (1946) Methods of computing vertical motion in the atmosphere, *J. Meteorol.*, 3, 45-49
- [49] Rao, G. V., (1966) On the influences of fields of motion, baroclinicity and latent heat source on frontogenesis, *J. Atmos. Sci.*, 39, 296-327
- [50] Reed, R. J., and F. Sanders, (1953) An investigation of the development of a mid-tropospheric frontal zone and its associated vorticity field, *J. Meteorol.*, 10, 338-349
- [51] Reed, R. J., and S. L. Mullen, (1981) *STREX Meteorological Atlas*. STREX Data Centre, U. Wash., Seattle, 90 pp.

- [52] Sanders, F., (1955) An investigation of the structure and dynamics of an intense surface frontal zone, *J. Meteor.*, 12, 542-552
- [53] Sansom, H. W., (1951) A study of cold fronts over the British Isles, *Q. J. Roy. Met. Soc.*, 77, 96-120
- [54] Sawyer, J. S., (1956) The vertical circulation at meteorological fronts and its relation to frontogenesis, *Proc. Roy. Soc.*, A234, 246-262
- [55] Stewart, R. E., and S. R. Macpherson, (1989) Winter storm structure and melting-induced circulations, *Atmos. Ocean*, 27, 5-23